Monte Carlo Simulation Study of Dense Astrophysical Plasmas:
Freezing, Transport, and Nuclear Reaction

高密度宇宙プラズマのモンテカルロシミュレーション：
固化，輸送，および核反応

Shuji Ogata
尾形修司

高密度宇宙プラズマのモンテカルロシミュレーション

尾形修司

Kodak Color Control Patches
Blue Cyan Green Yellow Red Magenta White 3/Color Black
© Kodak 2007 TM: Kodak

Kodak Gray Scale
A 1 2 3 4 5 6 M 8 9 10 11 12 13 14 15 B 17 18 19
© Kodak 2007 TM: Kodak

Monte Carlo Simulation Study of Dense Astrophysical Plasmas: Freezing, Transport, and Nuclear Reaction

Shuji Ogata

Department of Physics, University of Tokyo

December 1990

Dissertation submitted to the University of Tokyo for partial fulfillment of the requirements for the degree of Doctor of Science

ACKNOWLEDGMENTS

I should like to express my sincere gratitude to Professor Setsuo Ichimaru for the continuing guidance and encouragements throughout this study and for critical reading and improvement of the original manuscript. I learned from him the importance of distinguishing essential elements from complicated physical phenomena in making researches into them. I appreciate useful discussions on this study and related topics with the past and present colleagues of our research group at the University of Tokyo, namely, Dr. H. Iyetomi, Dr. S. Tanaka, Dr. X.-Z. Yan, Dr. A. Nakano, Mr. K. Sato, Mr. S. Kaneko, Mr. K. Tsuruta, and Mr. N. Nakamura. Finally, I wish to thank my parents for their immeasurable affection and support.

ABSTRACT

The dense stellar matter inside a compact star offers an excellent example of dense plasmas in nature. Inside a white dwarf and in the outer crust of a neutron star, the ions obey the classical statistics since their thermal de Broglie wavelengths are smaller than the average interparticle spacings. The electrons may be regarded as a uniform charge-background for the ions; their compressibility is negligible because they are relativistically degenerate. A classical plasma is predicted to freeze when the Coulomb coupling parameter Γ, which is the ratio of Coulomb energy to the thermal energy, exceeds around 180. In dense-stellar plasmas, where Γ parameter may take on values 100–1000, a freezing transition may take place during the course of stellar evolution. Besides being one of the fundamental problems in statistical physics, we remark in particular that such a freezing transition should alter the physical properties and the elementary processes in the plasma. With astrophysical applications in mind, we thus study freezing transitions in classical ion plasmas microscopically using computer-simulation method.

We begin with investigation of the freezing transition in the classical one-component plasmas (OCPs). The OCP is a system of point charges embedded in a uniform neutralizing background. Equations of state for the OCP in fluid and crystalline phases have been accurately determined mainly by the Monte Carlo (MC) simulation method. Comparing the free energy between the two phases, it has been predicted that the OCP freezes into the *bcc* crystalline state at $\Gamma_{\rm m} \simeq 180$.

To investigate how and in what stages the ordering of particles develops in the freezing transition, we perform MC simulations for rapidly supercooled OCPs

with the number of particles $N = 1458$. Starting from a fluid state at $\Gamma = 160$, we apply stepwise quenches to $\Gamma = 300$ and 400; each run continues until the system reaches a metastable state. At each stage of the simulations, we analyze the structure of particle positions in detail using various methods of representation, such as radial-distribution functions, distributions of coordination numbers, values of rotationally invariant combinations of the spherical harmonics attached to each bond (i.e., a connecting line between a particle and its neighboring particle).

Earlier, we performed MC simulations for the freezing transition in OCPs with $N = 432$. The resultant final states corresponded to glasses characterized by random polycrystalline mixtures of *fcc*, *hcp*, and *bcc* structures. Examination of N-dependence in the freezing transition is another purpose for performing present simulations with $N = 1458$.

As a result of these analyses, we find that layered structures emerge at pre-nucleation stages in the system and expedite a subsequent evolution into metastable states. The metastable states are *bcc* monocrystalline states with an admixture of a few defects in the form of interstitials.

The difference between the former results and the present one should originate from the difference in periodic boundary conditions in the MC cell which are directly related to values of N. The boundary conditions may affect in two ways in the freezing transition depending on values of N: If N belongs to one of the specific values associated with formation of a lattice structure, the boundary conditions may act to transform the system into the lattice structure for smaller N. If it does not, particle motions may be hindered by the boundary conditions for smaller N. Numbers of particles in both simulations are chosen appropriate to

the *bcc* structure. However, the choice of N at a *bcc* number appears to bear no essential consequences to the freezing processes since the matastable states in the present simulations contain substantial numbers of imperfections from the perfect *bcc* crystalline states as well as in the former simulations.

We thus conclude that the OCPs undergo freezing in two steps: when the plasma is rapidly supercooled to $\Gamma > \Gamma_m$, particle layers emerge first in an arbitrary direction, which would favor a *fcc*/*hcp* local structure. If N is large enough, the system may transform into the *bcc* structure in which the free energy assume the lowest value.

Dense stellar plasmas are usually composed of multiple species of ions. As a typical example, we choose a binary-ionic mixture (BIM) and a possibility of phase separation in such a system at the freezing transition is studied.

The BIM of carbon (C) and oxygen (O) is thought to constitute the internal composition of a white dwarf in a close binary system, which may make a progenitor of a Type I supernova (SNI). Accurate determination of the phase diagram is needed in a prediction of the evolution scenario for a white dwarf and of the mechanisms for the SNI processes. Stevenson showed how sensitive the phase diagram of C-O BIMs was to the assumptions of thermodynamic models, and in particular pointed out a possibility of a eutectic phase diagram resulting in a chemical separation, when the random-alloy mixing model was assumed for the internal energy in the solid phase.

We perform MC simulations of C-O BIMs at various combinations of density-temperature and molar fraction of oxygen for both fluid and *bcc*-solid phases. We find that the internal energies in both phases are accurately described by the linear

mixing formula of the OCP internal energies. Such a finding leads to a prediction that the chemical separation is not likely to take place in both phases. With the use of results for the mixing entropy by separate variational calculations, we obtain an azeotropic phase diagram for C-O BIMs.

Finally we apply the results of such phase transitions in plasmas to the astrophysical problems. We calculate conductivities, elasticities, and nuclear reaction rates accurately in each phase and clarify the effects of phase transitions in dense plasmas.

The outer crustal matter exhibiting possibilities of freezing may be modeled fairly well by an iron OCP. The thermal conductivity in the crustal matter is an important quantity in the calculation of a temperature profile from inside to outside of a neutron star. The electric conductivity may be an essential quantity in a theoretical estimate for the decay rate of the magnetic fields in a neutron star. Applying results in the quenched simulations as well as in the separately MC-simulated crystalline solids to the outer crustal material of a neutron star, we calculate the conductivities by the Ziman formula for relativistic electrons. In the crystalline phase, we find that the calculated conductivities take on values smaller by a factor of 2–3 than those evaluated in the single-phonon approximation. The conductivities in the quenched solids are 20–40% smaller than those for the *bcc* crystalline solids.

A neutron star may be modeled as a three-component star consisting of fluid interior, solid crusts, and fluid "ocean." McDermott *et al.* first analyzed nonradial oscillation spectra of such a star and predicted the existence of new modes associated with the non-vanishing shear modulus of the crusts, which have a characteristic periodicity on the order of milliseconds. The value of shear modulus

used in their analysis was inappropriate in that it corresponds to a specific mode of deformation at $T = 0$. We calculate the shear modulus tensors of the quenched and crystalline solids from first principles including the temperature dependence. The calculated values of the tensorial elements are anisotropic and diminish near the melting conditions. Since the calculation of nonradial oscillation spectra assumes isotropy in the crust, we introduce an effective shear modulus through averages on the dispersion relation for the transverse shear modes with respect to the polarizations and directions. Newly analyzed nonradial oscillation spectra for a model neutron star using the effective shear modulus show that the oscillation periods increase by less than 30% than those in the earlier calculations due to McDermott *et al.*

Accurate determinations of nuclear reaction rates in C-O BIMs are essential in a theoretical investigation of the SNI processes. Nuclear reaction rates are in general proportional to the contact probability of two particles. Since the probability is enhanced strongly by many-body correlations in the system, it is necessary to take a correct account of the physical conditions involved. Those include whether the system is in fluid or in solid phase and whether it is a OCP or a BIM. We accurately derive the short-range screening potentials due to many-body correlations between ions in both fluid and solid phases. Nuclear reaction rates in the solid phase (pycnonuclear reaction) are obtained through the exact solution to the resultant Shrödinger equation. As a result, we find blocking effects of "O" nuclei against pycnonuclear reaction of "C" nuclei. Nuclear reaction rates in the fluid phases are determined through an average of the contact probabilities with respect to the relative energies.

In the aforementioned analyses on nuclear reaction rates, we neglected the screening effects of the electrons on the ground that the Fermi energy of the electrons is far larger than the Coulomb interaction energies. In the dense stellar material, however, relativistic effects soften the electrons against compression and may act to enhance nuclear reactions between the ions. The short-range screening effects of the electrons on Coulomb repulsion between the reacting nuclei have been calculated with the aid of the relativistic free-electron polarizability and the local-field correction for the degenerate electrons. Screening effects of the electrons on the long-range correlations between ions in the fluid phase are newly evaluated by the formula which is confirmed to have a good accuracy through comparison with the MC simulational results. We find that the electron screening brings about a considerable enhancement of nuclear reactions in high-Z materials such as C and O, even in the limit of high densities. As an application of those reaction rate calculations, we evaluate the carbon-ignition conditions appropriate to the white-dwarf interiors and show them on the density vs. temperature plane.

CONTENTS

GENERAL INTRODUCTION 1

Part A: CRYSTALLIZATION IN RAPIDLY QUENCHED ONE-COMPONENT PLASMAS 5

I. Introduction 5
II. Quenching processes 9
III. Bond-orientational order parameters 10
IV. Development of crystallization 18
V. Supercooled fluid state 46
VI. Discussion and concluding remarks 50

Part B: CONDUCTIVITIES AND SHEAR MODULI OF THE QUENCHED SOLIDS 56

I. Introduction 56
II. Quantum nature of ions and screening effects of electrons on the Madelung energy 59
III. Electric and thermal conductivities 64
IV. First principles calculation of shear moduli 67
V. Nonradial oscillation of neutron stars 78

Part C: EQUATION OF STATE AND PHASE DIAGRAM OF DENSE CARBON-OXYGEN MIXTURES 84

I. Introduction 84

II. Thermodynamic functions 85

III. Phase diagram 95

IV. Variations of mass density across the phase boundary 97

Part D: NUCLEAR REACTION RATES IN DENSE BINARY-IONIC MIXTURES 101

I. Introduction 101

II. MC screening potentials 103

III. Pycnonuclear reaction rates 111

IV. Thermonuclear reaction rates 117

V. Screening effects of relativistic degenerate electrons on the thermonuclear reaction rates 123

VI. Carbon ignition curves 135

VII. Concluding remarks 136

Appendix I: Fast computation of the Ewald potential 141

Appendix II: MC sampling of the coefficient h_2 in equation (D.3) 143

References 145

GENERAL INTRODUCTION

The dense stellar matter inside a compact star offers an excellent laboratory for a study on the physics of dense plasmas. The interior of a white dwarf (e.g., Shapiro and Teukolsky, 1983), one of the final stages of the stellar evolution, consists in dense material with the mass density 10^4–10^9 g/cm^3, corresponding to the electron density 10^{27}–10^{32} cm^{-3}, at the temperature 10^6–10^8 K. The neutron star (e.g., Shapiro and Teukolsky, 1983), another final stage of stellar evolution, is a highly condensed material corresponding approximately to a compression of a solar mass ($\sim 2 \times 10^{33}$ g) into a spherical body with a radius $\sim$ 10 km. According to a theoretical model study (e.g., Pandharipande, Pines, and Smith, 1976), it has a crust with a thickness of several hundred meters and a mass density in the range 10^4–10^9 g/cm^3, consisting mostly of iron.

The Fermi energy of the electrons in such a dense matter takes on a value much greater than the binding energy of an electron around an atomic nucleus; all the atoms are thus in pressure-ionized states. The Coulomb energy in the electron system is far smaller than the immensely large Fermi energy. The electron system makes an ideal neutralizing background of negative charges for the ionized nuclei, since its compressibility is negligible.

Those atomic nuclei stripped of the electrons form an ion plasma obeying the classical statistics; their de Broglie wavelengths are much smaller on the average than the interparticle spacings. In the interior of a highly evolved star, the Coulomb coupling parameter, defined as a ratio between the average Coulombic and kinetic energies, usually takes on a value greater than unity and may reach

as large a value as 10^3 under extreme conditions. Such a material may thus be looked upon as a strongly coupled plasma (Ichimaru, 1982).

When the Coulomb coupling parameter exceeds a critical value around 180, the plasma is known to solidify. This is the classical counterpart to the Wigner transition, predicted in the low-density degenerate electron systems (Wigner, 1934; Pines, 1964). The freezing transitions are therefore an essential feature in the physics of dense-stellar materials.

On the basis of the foregoing grasp of the astrophysical dense plasmas, Part A of this Thesis treats the problems associated with the physical mechanisms of freezing transitions. In so doing, we introduce a one-component plasma (OCP) model of dense material, appropriate for a description of the crustal matter in neutron stars. The freezing transitions are approached here by a Monte Carlo (MC) simulation method, through applications of a series of quenches (sudden decreases in temperature) to the OCP systems. Evolutions of the interparticle correlations and ordering are monitored microscopically in such a MC-simulated OCP. Internal developments in the freezing transitions are thereby elucidated for the Coulombic materials.

In Part B, we apply the results of the freezing-transition analyses in Part A to the calculations of the electric and thermal conductivities in the outer crustal matter of neutron stars. The thermal conductivity of the crust is a crucial element for a prediction on the thermal evolution in a neutron star (Gudmundsson, Pethick, and Epstein, 1982). The electric conductivity may have relevance in a theoretical account of decay mechanisms for the stellar magnetic field.

Treated also in Part B is the mechanical property of the crustal matter, represented by the shear modulus tensor of the Coulomb solids. First principles

calculations for the shear modulus tensor are presented for the *bcc* crystalline and rapidly quenched Coulomb solids produced by MC simulations for temperatures up to the melting conditions. The neutron star has a feature unique in astrophysical objects in that it may be modeled as a three-component star consisting of a fluid interior, a solid crust, and a fluid "ocean." The nonvanishing shear modulus of the crustal solid leads to a novel prediction for the associated bulk and interfacial modes in the spectra of the nonradial oscillations (McDermott *et al.*, 1985, 1988).

Part C analyzes another kind of freezing transition problems in dense matter, namely, the possibilities of phase separations associated with freezing in dense binary-ionic mixtures (BIMs). Specifically we consider a core material in a white-dwarf progenitor of Type-I supernova, modeled as a dense mixture of two ionic species: carbon and oxygen (Starrfield *et al.*, 1972). The phase diagrams of such a multi-component material at the freezing transitions are the factors that essentially affect the developments in the internal structures of white dwarfs and thereby control the resultant supernova mechanisms (Canal, Isern, and Labay, 1982; Mochkovitch, 1983).

The phase diagrams depend quite sensitively on the equations of state for the strongly coupled BIMs. We perform MC simulations at various combinations of the BIM parameters and thereby set accurate constraints on the BIM equations of state. A phase diagram will be predicted, and its astrophysical implications will be discussed.

Finally in Part D, we present most accurate calculations to date for the nuclear reaction rates in astrophysical dense materials, again with the aid of elaborate MC simulation study of the screening potentials.

The reaction rates generally depend on the strength of overlapping between wave functions of the two reacting nuclei (e.g., Salpeter and Van Horn, 1969), and as such are closely related to joint probability functions between the two particles (albeit at a short distance, i.e., in the nuclear-force range). Such a joint probability function is in turn strongly influenced by the states of a dense material under consideration. Elements of distinction involved in the present context are, for instance, whether the matter is a OCP or a BIM, whether it is in a frozen state leading to pycnonuclear reactions or in an itinerant fluid state leading to thermonuclear reactions, and to what extent the electron screening may influence the rates of nuclear reactions. In each of those distinct cases, the microscopic interparticle correlations exhibit different features, resulting in varied predictions on the reaction rates. The results of these calculations are applied to dense carbon-oxygen BIMs with and without electronic screening; ignition curves are thereby obtained through balancing the resulting energy-production rates with energy-loss mechanisms such as neutrino-processes.

Part A: CRYSTALLIZATION IN RAPIDLY QUENCHED ONE-COMPONENT PASMAS

I. Introduction

Solidification such as crystallization and glass transition is one of the most interesting events in the thermal evolution of a many-body system. Accumulation of the effort by many investigators notwithstanding, microscopic understanding of such a transition has remained an outstanding problem. Theoretical treatment is difficult since the transition occurs catastrophically as a result of many-body correlations; it is neither easy to trace the dynamic evolutions of the microscopic structures in a laboratory experiment.

Computer simulation study of a simple system (e.g., Hansen and McDonald, 1986) where particles interact via binary and spherically symmetric potentials has a long history. More than three decades ago, Monte Carlo (e.g., Binder, 1979) (MC) and molecular dynamics (e.g., Ciccotti *et al.*, 1987) (MD) simulation methods were first applied to the hard core systems (Alder and Wainwright, 1957, 1959). Later these methods were extended to other cases of the potentials, such as soft core (e.g., Hansen and McDonald, 1986) and Lennard-Jones (e.g., Hansen and McDonald, 1986). Available size of the simulations has rapidly increased as the computer capabilities develop. Simulation studies of crystallization and glass transition for these systems have contributed much to the explanation for physical properties of the solids.

Classical one-component plasma (Baus and Hansen, 1980; Ichimaru, Iyetomi, and Tanaka, 1987) (OCP), one of the most fundamental in simple systems, is

a statistical system where N particles of single species with charge Ze interact via Coulomb potentials in a volume V with uniform neutralizing charges. Since the Coulomb potential has no characteristic length, thermodynamic properties of the OCP with number density $n = N/V$ depend only on the Coulomb coupling parameter

$$\Gamma = \frac{(Ze)^2}{ak_{\rm B}T} \tag{A.1}$$

where

$$a = \left(\frac{3}{4\pi n}\right)^{1/3} \tag{A.2}$$

is the ion-sphere radius. The OCP is distinct from other simple systems in at least two respects: First, Coulomb potential is long-ranged; hence it is necessary to assess the effects of the boundary conditions carefully. Second, no volume fluctuations exist in the OCP at a fixed value of N since the background charges are incompressible; the OCP keeps its volume constant through the process of solidification.

The OCP has been treated not only as a basic model in the statistical mechanics but as a realistic model for the dense matter in the outer crust of a neutron star (e.g., Van Horn, 1990; Shapiro and Teukolsky, 1983). The main constituent of the outer crust is iron in the density-temperature regime, $\rho_{\rm m} = 10^4$–10^9 g cm^{-3} and $T = 10^6$–10^8 K; hence $\Gamma = 100$–1000. Electrons in the crusts are relativistically degenerate and may be regarded as forming a uniform charge-background for the iron ions. Physical properties of the outer crust such as conductivities (Ogata and Ichimaru, 1990a) and viscoelasticity (Ichimaru and Tanaka, 1986; Ogata and Ichimaru, 1990b), are essential ingredients in the analyses of the internal structure and the evolution of the star.

Equation of state for the OCP has been investigated accurately in the fluid (Brush, Sahlin, and Teller, 1966; Hansen, 1973; Slattery, Doolen, and DeWitt, 1980, 1982; Ogata and Ichimaru, 1987) and in the *bcc* (Brush *et al.*, 1966; Hansen, 1973; Slattery *et al.*, 1980, 1982) and *fcc* (Helfer, McCrory, and Van Horn, 1981) crystalline phases mainly by the MC simulation method, including dependence on the particle number, N. Comparing the Helmholtz free energies between the fluid and crystalline phases, it has been found (Slattery *et al.*, 1982; Ogata and Ichimaru, 1987) that the fluid OCP freezes (Wigner transition) into the *bcc* crystals at $\Gamma_{\rm m} = 178$–180.

It is not clear, however, what the final state of a OCP is when a rapid quench is applied to $\Gamma > \Gamma_{\rm m}$. It is instructive in these connections to compare the Madelung energies (e.g., Brush *et al.*, 1966) of the OCP between the crystalline structures:

$$\frac{E_{\rm M}}{Nk_{\rm B}T} = \begin{cases} -0.895929\Gamma, & \text{(bcc)} \\ -0.895874\Gamma, & \text{(fcc)} \\ -0.895838\Gamma, & \text{(hcp)}\ . \end{cases} \tag{A.3}$$

We thus find $(E_{\rm fcc} - E_{\rm bcc})/N = 0.010k_{\rm B}T$ and $(E_{\rm hcp} - E_{\rm bcc})/N = 0.016k_{\rm B}T$ at $\Gamma = 180$; the differences are only 1–2% of the thermal energy.

The MC simulations for rapidly quenched OCPs with $N = 432$ were performed and reported earlier in Ogata and Ichimaru (1989a) (referred to as Paper I). The resultant final states corresponded to glasses characterized by random polycrystalline mixtures of *fcc*, *hcp*, and *bcc* crystalline structures. In those glasses, we found development of layered structures (Ogata and Ichimaru, 1989b) over the MC cell. Emerged out of those simulations are the problems: Do the layered structures have any relation with the periodic boundary conditions ? How and in what

stage are the layered structures formed ? Is it possible to obtain a monocrystalline state, rather than a polycrystalline state, by the MC simulation method ?

To answer these problems and to apply the quenched states to the investigation on the physical properties of the neutron star crusts, we have performed new MC simulations for rapidly supercooled OCPs with a significantly increased value of N. The periodic boundary conditions depending on N may have two kinds of effects on the solidification. Under the periodic boundary conditions, any particle must move collectively with all of its images which form a simple cubic lattice with the lattice constant $L \propto N^{1/3}$. For a smaller N, the boundary conditions may hinder the motion of particles and the resultant ordering of particles. However, if N takes on a value specific to the lattice structures, such as a *bcc* number $2I^3$ or a *fcc* number $4I^3$ (I is an integer), the boundary conditions may assist in transforming the system into the respective lattice structure; such an effect may be more efficient for a smaller N. We remark that $N = 432$ in Paper I is one of the *bcc* numbers. To examine those two effects separately, we have chosen $N = 1458$, another *bcc* number; this number is more than three times as large as that in Paper I. The resulting side length of the MC cell is $L = (4\pi N/3)^{1/3}a = 18.3a$.

In Part A of this Thesis, we thus report detailed analyses on the results of these newly performed simulations (Ogata, 1991). We find a formation of particle layers in the pre-nucleation stages. Internal energies at the metastable states are very close to the *bcc* crystalline value. Unlike the glass structures obtained in the former simulations, we find *bcc* monocrystalline structures in the resultant metastable states. Preliminary results have been reported in Ogata and Ichimaru (1989c, 1989d).

The organization of Part A is the following: In Sec. A.II quenching processes are described. In Sec. A.III we introduce bond-orientational order parameters to monitor the development of nucleation. In Sec. A.IV the main results are presented. Section A.V is devoted to a description of a separate simulation, where a supercooled fluid state is obtained. Discussion and concluding remarks are given in Sec. A.VI.

II. Quenching processes

We perform MC simulations with the usual Metropolis algorithm (Metropolis *et al.*, 1953): First a randomly selected particle is displaced tentatively by $\Delta\vec{r}$ with probability $P(|\Delta\vec{r}|)$; the new configuration is accepted with the probability $\exp(-\Delta U/k_{\rm B}T)$, where ΔU is an increment of the internal energy between the new and the original configurations (all the cases with $\Delta U < 0$ are accepted). The procedure just described constitutes a single step in the MC simulations; the number of configurations so generated is denoted by c. In Appendix I, we explain a technique to accelerate computation of internal energies.

For the probability density of particle displacements, we have adopted the form same as that in Paper I, that is,

$$P(r) = \sqrt{\frac{2\Gamma}{\pi}}\Gamma\left(\frac{r}{a}\right)^2 \exp\left[-\frac{\Gamma}{2}\left(\frac{r}{a}\right)^2\right] \tag{A.4}$$

with the normalization $\int_0^\infty P(r)dr = 1$. If the concept of "MC elapsed time" applies, we may estimate the elapsed time via the relation (Ogata and Ichimaru, 1988),

$$\omega_p t = 0.12\ c/N\ . \tag{A.5}$$

The quenching processes are schematically depicted in Fig. A.1. Starting with a fluid equilibrium state at $\Gamma = 160$, we apply stepwise quenches by $\Delta\Gamma = 50$ at every $c/N \times 10^{-4} = 1.25$, excepting for $\Delta\Gamma = 40$ at $c = 0$, until Γ reaches 300 (Fig. A.1 (top)) and 400 (Fig. A.1 (bottom)). Phase evolution is monitored until $c/N \times 10^{-4} = 25.0$ in both cases. Stepwise quench to $\Gamma = 800$ is applied subsequently to the final state obtained at the quench to $\Gamma = 400$; simulation has been continued until $c/N \times 10^{-4} = 35.0$. If we assume the relation Eq. (A.5) for the estimation of the elapsed time, the rates of quenches to $\Gamma = 300$ and 400 should be the same as those in the cases of "gradual quench" in Paper I.

III. Bond-orientational order parameters

Orders in the particle configurations are described in terms of the orientational correlations between "bonds," which are connecting lines between a particle and its "neighboring particles." We define the "neighboring particles" as particles inside a sphere of radius $r/a = 2.3$ around a given particle; particle positions are averaged over a sequence of $\Delta c/N \times 10^{-4} = 0.069$ to reduce the thermal fluctuations. The radius $r/a = 2.3$ corresponds approximately to the first bottom of the radial distribution functions $g(r)$ both in the fluid phase near the freezing condition shown in Fig. A.2 (left) and in the *bcc* crystalline phase shown in Fig. A.2 (right). The number N_c of neighboring particles, which we shall call "coordination number," is 14 for the *bcc* cluster; and 12 for the *fcc*, *hcp*, and *icosahedral* clusters. In the fluid simulation at $\Gamma = 160$, $N_c = 12$–14 for almost all the particles. In the *bcc* crystalline simulation at $\Gamma = 400$, $N_c = 14$ for all the particles. We associate a set of quantities $\{Q_{lm}(\vec{r})\}$ to each bond in terms of

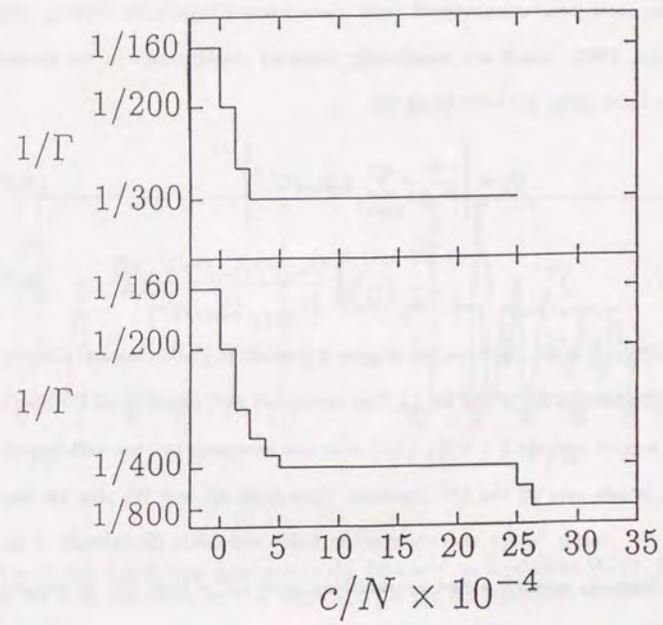

Fig. A.1 Variation of $1/\Gamma$ in the MC simulation runs: (upper) is the quench to $\Gamma = 300$; (lower) is the quench to $\Gamma = 400$ and subsequently to $\Gamma = 800$.

the spherical harmonics: $Q_{lm}(\vec{r}) = Y_{lm}(\theta(\vec{r}), \phi(\vec{r}))$, $\vec{r}$ is the central position of a bond, $\theta(\vec{r})$ and $\phi(\vec{r})$ are its polar angles.

The local bond-orientational order parameters (Steinhardt, Nelson, and Ronchetti, 1983), which are rotationally invariant combinations in the second and the third order, are introduced via

$$Q_l = \left[\frac{4\pi}{2l+1} \sum_{|m| \le l} |\langle Q_{lm}(\vec{r}) \rangle|^2 \right]^{1/2} , \tag{A.6}$$

$$W_l = \sum_{m_1+m_2+m_3=0} \begin{pmatrix} l & l & l \\ m_1 & m_2 & m_3 \end{pmatrix} \frac{\bar{Q}_{lm_1}(\vec{r}) \bar{Q}_{lm_2}(\vec{r}) \bar{Q}_{lm_3}(\vec{r})}{\left[\sum_{|m| \le l} |\bar{Q}_{lm}(\vec{r})|^2 \right]^{3/2}} . \tag{A.7}$$

The coefficients in Eq. (A.7) are the Wigner 3j symbols (e.g., Landau and Lifshitz, 1976). The average $\bar{Q}_{lm}(\vec{r})$ in Eq. (A.7) is carried out with regard to all the bonds around a given particle; $\langle\ \rangle$ in Eq. (A.6) means an analogous average with respect to such bonds over all the MC particles. Quantities Q_l and W_l play the key part in the cluster "shape spectroscopy" in fluids and solids (Steinhardt *et al.*, 1983). Since Q_4 assumes a first nonvanishing value (other than Q_0) in samples with cubic symmetry, and Q_6 in icosahedral systems, we take $l = 4$ and 6 in the present analyses.

The quantities (Q_4, Q_6) take on values (0.1909, 0.5745) for the *fcc*, (0.0972, 0.4848) for the *hcp*, (0, 0.6633) for the *icosahedral*, and (0.0364, 0.5107) for the *bcc* clusters. We observe that Q_4 differ significantly from each other for the four types of clusters, while Q_6 remain almost the same. It is ascertained that (Q_4, Q_6) take on much smaller values, (0.01, 0.03), in the fluid simulation at $\Gamma = 160$ than the *bcc* crystalline simulation values (0.04, 0.5).

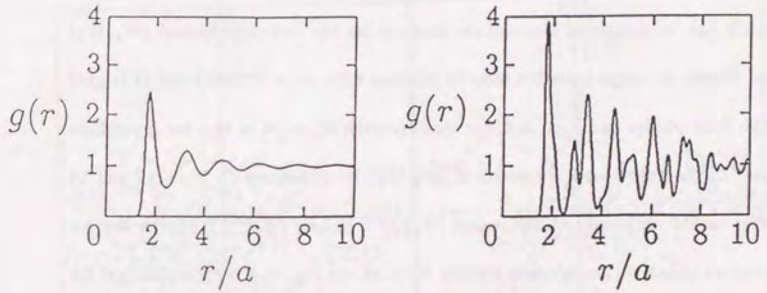

Fig. A.2 The radial distribution functions in the fluid and *bcc* crystalline OCPs: (left) is the fluid simulation at $\Gamma = 160$; (right) is the *bcc* crystalline simulation at $\Gamma = 400$.

The quantities W_4 and W_6 assume significantly different values between the clusters: $(W_4, W_6) = (-0.1593, -0.0132)$ for the *fcc*, $(0.1341, -0.0124)$ for the *hcp*, $(0, -0.1698)$ for the *icosahedral*, $(0.1593, 0.0132)$ for the *bcc* clusters. We remark that W_4 is not a well defined quantity for the *icosahedron* since $Q_4 = 0$. The magnitude of W_6 is substantially larger for the *icosahedron* than for the other three types of clusters. We find that the local bond-orientational symmetries around a particle can be discerned through its location on the two-dimensional (W_4, W_6) map. Figure A.3 depicts such a map for clusters with $N_c = 12$ (left) and 14 (right) at the fluid phase, and Fig. A.4, for clusters with $N_c = 14$ at the *bcc* crystalline phase. In the fluid phase, locations of (W_4, W_6) for clusters with $N_c = 12$ and 14 scatter rather uniformly in the region $|W_4| \leq 0.15$ and $|W_6| \leq 0.16$. In the *bcc* crystalline phase, all the clusters assume $N_c = 14$. In Fig. A.4, we observe that for a substantial fraction of clusters the bond-orientational parameters deviate from the *bcc* values especially for W_4 parameter owing to thermal fluctuations.

Extended bond-orientational symmetries (Steinhardt *et al.*, 1983) are studied in terms of the correlation functions

$$G_l(r) = \frac{4\pi}{(2l+1)G_0(r)} \sum_{|m|\leq l} \langle Q_{lm}(\vec{r}) Q_{l-m}(\vec{0}) \rangle \qquad \text{(A.8)}$$

where $G_0(r) = 4\pi \langle Q_{00}(\vec{r}) Q_{00}(\vec{0}) \rangle$. $G_l(r)$ take on first nonvanishing values at $l = 6$ for the *bcc* structure. We find in Fig. A.5 (left) that $G_6(r) \simeq 0$ in the fluid simulation at $\Gamma = 160$, indicating absence of an extended order. In the *bcc* crystalline phase at $\Gamma = 400$, $G_6(r) \simeq 0.3$ as shown in Fig. A.5 (right), confirming

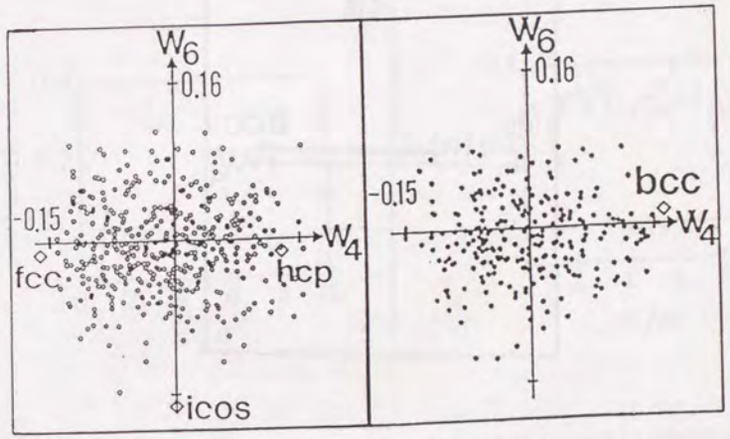

Fig. A.3 Two-dimensional (W_4, W_6) maps in the fluid OCP at $\Gamma = 160$: (left) is the particles with $N_c = 12$ shown by open circles; (right) is the particles with $N_c = 14$ shown by closed circles. Diamond markers correspond to (W_4, W_6) values for the *fcc*, *hcp*, *icosahedral*, and *bcc* clusters; for the *icosahedron*, we set $W_4 = 0$ here.

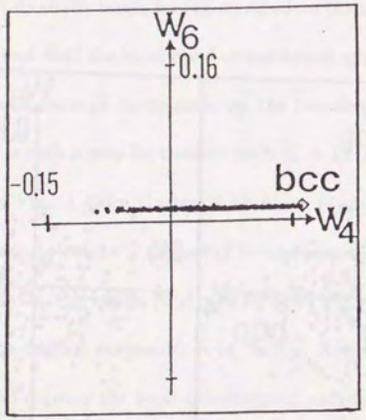

Fig. A.4 Two-dimensional (W_4, W_6) map in the *bcc* crystalline OCP at $\Gamma = 400$ for the particles with $N_c = 14$. Diamond marker corresponds to (W_4, W_6) value for the *bcc* cluster.

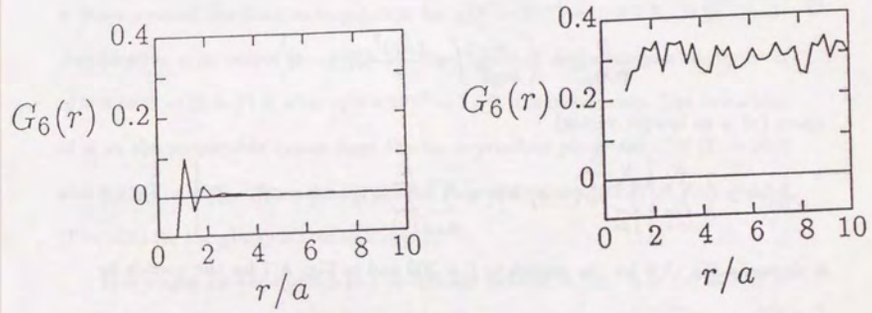

Fig. A.5 Bond-orientational correlation function $G_6(r)$: (left) is the fluid simulation at $\Gamma = 160$; (right) is the *bcc* crystalline simulation at $\Gamma = 400$.

the existence of a long-range extended order.

IV. Development of crystallization

(a) Excess internal energies

Excess internal-energy (Ichimaru, Iyetomi, and Tanaka, 1987) is a primary quantity in characterizing the states of OCP since its volume is fixed. Evolution of the excess internal-energy per particles, averaged over a sequence of $\Delta c/N \times 10^{-4} = 0.007$,

$$u \equiv \frac{U}{N k_{\rm B} T} = \left\langle \frac{n}{2 k_{\rm B} T} \int d\vec{r} \frac{(Ze)^2}{r} [\hat{g}(r) - 1] \right\rangle , \tag{A.9}$$

where ($\vec{m}$ is an integer vector)

$$n\hat{g}(\vec{r}) = \frac{1}{N} \sum_{i=1}^{N} \left\{ \sum_{j \neq i}^{N} \delta(\vec{r}_i - \vec{r}_j - \vec{r}) + \sum_{\vec{m} \neq \vec{0}} \sum_{j=1}^{N} \delta(\vec{r}_i - \vec{r}_j + \vec{m}L - \vec{r}) \right\} \tag{A.10}$$

is shown in Fig. A.6 for the quench to $\Gamma = 300$ and in Fig. A.7 for the quench to $\Gamma = 400$.

In each figure, dashed lines imply the extrapolation values of the fluid internal energy formula,

$$u = -0.897744\Gamma + 0.95043\Gamma^{1/4} + 0.18956\Gamma^{-1/4} - 0.81487 \tag{A.11}$$

due to Slattery *et al.* (1982) for the upper line, and

$$u = -0.898004\Gamma + 0.96786\Gamma^{1/4} + 0.220703\Gamma^{-1/4} - 0.86097 \tag{A.12}$$

due to Ogata and Ichimaru (1987) for the lower. The dot-dashed line means the *bcc* crystalline value according to the formula (Slattery *et al.*, 1982)

$$u = -0.895929\Gamma + 1.5 + 3225\Gamma^{-2} . \tag{A.13}$$

We note that the *fcc* crystalline value (Helfer *et al.*, 1981) of u are higher than the *bcc* one only by 0.01–0.02 for $\Gamma = 300$–400.

In the case of the quench to $\Gamma = 300$, u stays around the fluid extrapolation value for $c/N \times 10^{-4} = 2.5$–6.0. It gradually decreases as c increases for $c/N \times 10^{-4} = 6.0$–8.0, and decreases abruptly at $c/N \times 10^{-4} = 8.0$–9.0 and at 11.0–12.0; after $c/N \times 10^{-4} \simeq 12.0$, it is metastable though jitters are observed. The evolution of u for the quench to $\Gamma = 400$ is similar to that for the case with $\Gamma = 300$; u stays around the fluid extrapolation for $c/N \times 10^{-4} = 5.0$–7.5. It gradually decreases as c increases for $c/N \times 10^{-4} = 7.5$–15.0, and decreases abruptly at $c/N \times 10^{-4} = 15.0$–17.0; after $c/N \times 10^{-4} \simeq 17.0$, it is metastable. The deviations of u at the metastable states from the *bcc* crystalline phase are 0.08 ($\Gamma = 300$) and 0.21 ($\Gamma = 400$). Those are far smaller than the values 0.25 ($\Gamma = 300$) and 0.4 ($\Gamma = 400$) for the glassy states in Paper I.

Five stages for the quench to $\Gamma = 300$ are defined in Fig. A.6: (a) at $c/N \times 10^{-4} = 4.6$, (b) 7.0, (c) 8.6, (d) 9.5, (e) 24.9. For the quench to $\Gamma = 400$, four stages are also defined in Fig. A.7: (α) 7.3, (β) 12.1, (γ) 15.8, (δ) 19.5. Stages (c) and (γ) correspond to a midst of the abrupt decreases in u for the quenches to $\Gamma = 300$ and 400, respectively.

(b) Radial distribution functions

Evolution of $g(r) = \langle \hat{g}(\vec{r}) \rangle$ averaged over $\Delta c/N \times 10^{-4} = 0.21$ is displayed in Fig. A.8 for the quench to $\Gamma = 300$, and in Fig. A.9 for the quench to $\Gamma = 400$.

For the quenches to $\Gamma = 300$ and 400, $g(r)$ exhibits a smooth feature analogous to that in a fluid simulation (see Fig. A.2 (left)) at the stages before the abrupt decreases in u ((a), (b), (α), and (β)). For the quench to $\Gamma = 300$, the second

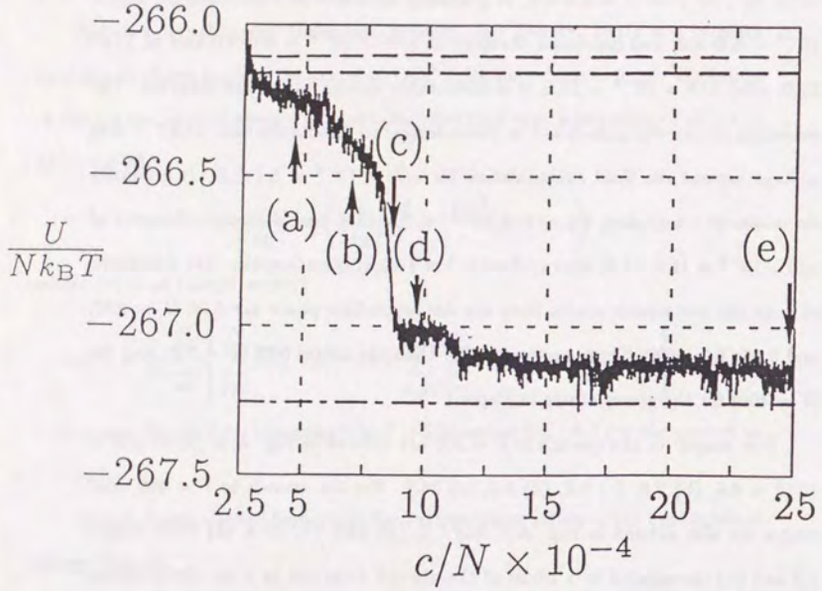

Fig. A.6 Evolution of the normalized excess internal-energy for the quench to $\Gamma = 300$. Stages are specified at (a) 4.6, (b) 7.0, (c) 8.6, (d) 9.5, and (e) 24.9. The dashed lines indicate the levels predicted from the extensions of the fluid internal-energy formulas [upper: Eq. (A.11), lower: Eq. (A.12)]; the dot-dashed line, the *bcc* crystalline level via Eq. (A.13).

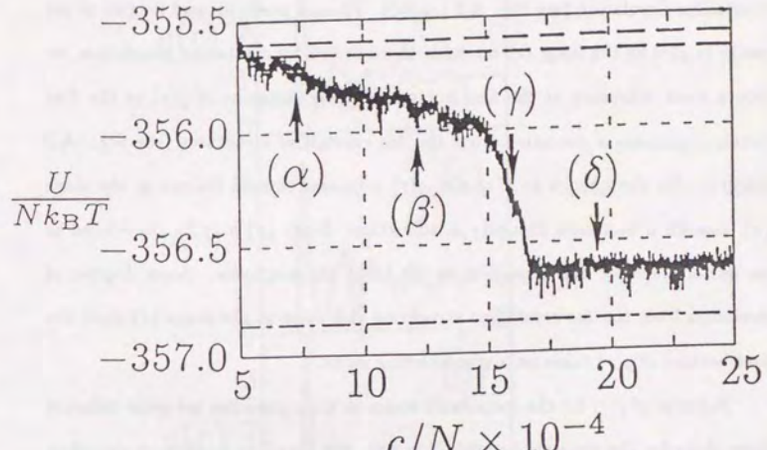

Fig. A.7 Evolution of the normalized excess internal-energy for the quench to $\Gamma = 400$. Stages are specified at (α) 7.3, (β) 12.1, (γ) 15.8, and (δ) 19.5. The dashed lines indicate the levels predicted from the extensions of the fluid internal-energy formulas [upper: Eq. (A.11), lower: Eq. (A.12)]; the dot-dashed line, the *bcc* crystalline level via Eq. (A.13).

and the third peaks of $g(r)$ have shoulders at radii corresponding to the *bcc* peaks at the stage (c). The system seems to have acquired a substantial degree of the *bcc* local structures at the stage (c). We find no substantial change in $g(r)$ from the stage (c) to (d). At the stage (e), $g(r)$ is quite similar to the one in the *bcc* crystalline simulation (see Fig. A.2 (right)). Though positions and heights of the peaks in $g(r)$ at the stage (e) resemble those in the *bcc* crystalline simulation, we find a clear difference at the first bottom of $g(r)$; finiteness of $g(r)$ at the first bottom indicates a deviation from the *bcc* crystalline structures (see Fig. A.2 (right)). For the quench to $\Gamma = 400$, $g(r)$ retains a smooth feature at the stage (γ), though u decreases abruptly at this stage. Stage (γ) may be considered as an initial stage for the transition to the local *bcc* structures. Some degrees of deviation from the *bcc* crystalline structures still exist at the stage (δ) since the first bottom of $g(r)$ takes on a nonvanishing value.

Features of $g(r)$ for the metastable states in both quenches are quite different from those for the simulations with $N = 432$. We found no peaks corresponding to the *bcc* structures in all the cases of the quench with $N = 432$. In one case, a few peaks appeared at the radii corresponding to the *fcc–hcp* structures. In other cases, however, we found several little peaks at those radii which have no correspondence to the *fcc-hcp* and *bcc* structures.

(c) Local bond-orientational orders

Evolutions of the local bond-orientational order parameters (Q_4, Q_6) are depicted in Fig. A.10 for the quench to $\Gamma = 300$ and in Fig. A.11 for the quench to $\Gamma = 400$. For the quench to $\Gamma = 300$, the rate of increase in Q_6 steepens at $c/N \times 10^{-4} = 6.0$–7.0, followed by the first abrupt decrease

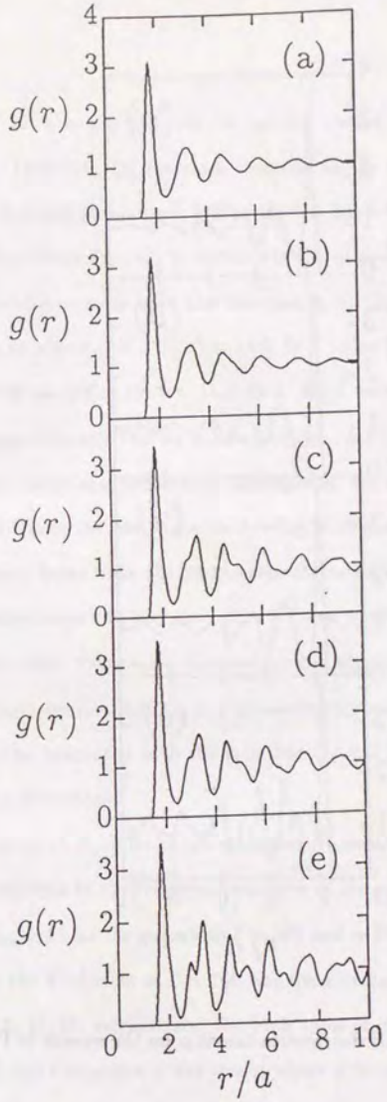

Fig. A.8 Evolution of the radial distribution function for the quench to $\Gamma = 300$.

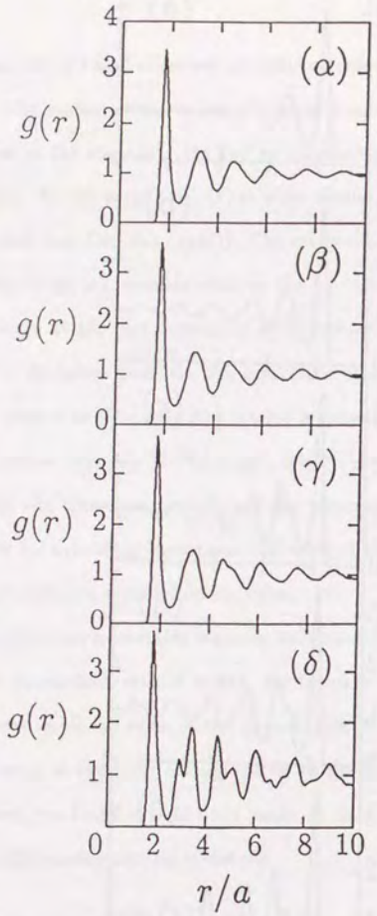

Fig. A.9 Evolution of the radial distribution function for the quench to $\Gamma = 400$.

in u at $c/N \times 10^{-4} = 8.0$–9.0. At the second abrupt decrease in u around $c/N \times 10^{-4} = 11.0$–$12.0$, Q_6 increases stepwise to $Q_6 \simeq 0.41$. In regard to Q_4, we find its increase at one time, $c/N \times 10^{-4} = 8.0$–9.0, corresponding to the first decrease in u; thereafter, $Q_4 \simeq 0.035$. For the quench to $\Gamma = 400$, both Q_4 and Q_6 increase concurrently with the decrease in u. Q_6 reaches 0.45 after its abrupt increase at about $c/N \times 10^{-4} = 15.0$–$17.0$. Also for the quantity Q_4, it jumps up to 0.039 at $c/N \times 10^{-4} = 15.0$–$16.0$. Final values of (Q_4, Q_6) in both quenches are approximately the *bcc* values (see Sec. A.III). The aforementioned difference in the evolutional processes of Q_6 between the two quenches indicates that the local orders in the two quenches develop in different ways.

We have thus found that the metastable states have a long-ranged bond-orientational order extending over the entire MC cell at the same level as that in a *bcc* crystalline state. Comparing the evolution of Q_4 with that of Q_6 in both quenches, we might remark that Q_4 is a parameter insensitive to the freezing in OCPs; this may be connected with the fact that $Q_4 = 0$ for *icosahedron*, one of the close-packing structures.

Since the values of N_c differ between clusters, it would be instructive to look into the the evolutions in the fractional numbers of the particles with $N_c = 12$, 13, and 14 in Fig. A.12 for the quench to $\Gamma = 300$ and in Fig. A.13 for the quench to $\Gamma = 400$. For the fluid state at $\Gamma = 160$, the fractional numbers are 0.30, 0.45, 0.20 for $N_c = 12$, 13, 14, respectively. For both cases of quenches, the fractional number with $N_c = 14$ increases at the stages where u decrease abruptly. Finally, about 95% of clusters in the metastable state have $N_c = 14$ for the quench to $\Gamma = 300$; about 83% for the quench to $\Gamma = 400$. These fractional numbers for

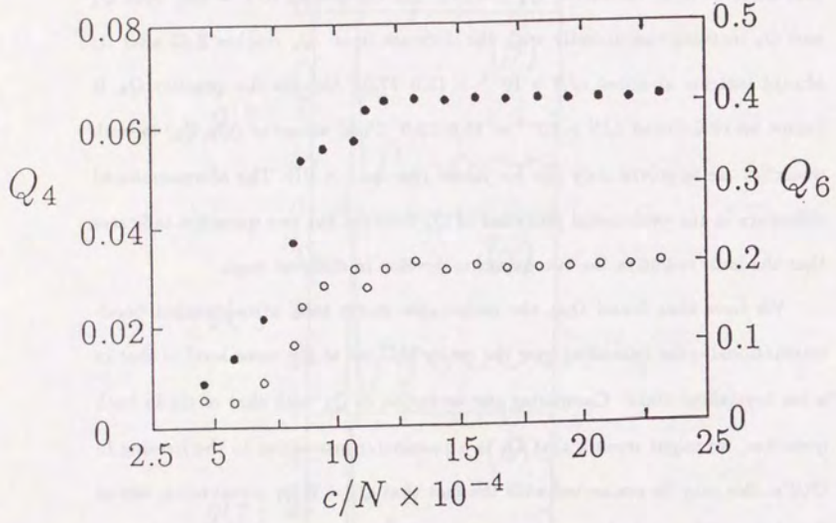

Fig. A.10 Evolution of the bond-orientational parameters, Q_4 and Q_6, for the quench to $\Gamma = 300$. Open circles correspond to Q_4 values; closed circles, Q_6 values.

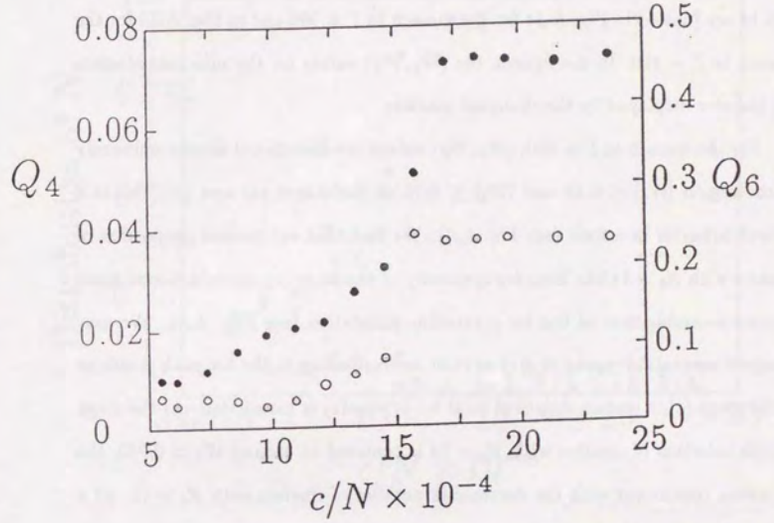

Fig. A.11 Evolution of the bond-orientational parameters, Q_4 and Q_6, for the quench to $\Gamma = 400$. Open circles correspond to Q_4 values; closed circles, Q_6 values.

$N_c = 14$ in both quenches are much larger than the values 10–50% in the cases with $N = 432$.

Evolutions of the two-dimensional (W_4, W_6) maps for clusters with $N_c = 12$ and 14 are plotted in Fig. A.14 for the quench to $\Gamma = 300$ and in Fig. A.15 for the quench to $\Gamma = 400$. In the figures, the (W_4, W_6) values for the reference clusters are likewise displayed by the diamond markers.

For the quench to $\Gamma = 300$, (W_4, W_6) values are distributed almost uniformly in the region $|W_4| \leq 0.15$ and $|W_6| \leq 0.16$ at the stages (a) and (b); this is a typical behavior in a fluid (see Fig. A.3). We find that substantial proportion of clusters with $N_c = 14$ has local *bcc* symmetry at the stage (c); distribution of these clusters resemble that of the *bcc* crystalline simulation (see Fig. A.4). We may interpret several sub-peaks of $g(r)$ at radii corresponding to the *bcc* peak positions at the stage (c); a certain degree of local *bcc* symmetry is manifested. At the stage (d), distribution of clusters with $N_c = 14$ is centered at around $W_6 \simeq 0.013$, the *bcc* value, concurrent with the decrease in number of clusters with $N_c = 12$. At a subsequent stage (e), we observe an increased degree of local *bcc* symmetry in the distribution of clusters with $N_c = 14$.

For the quench to $\Gamma = 400$, distributions of clusters with $N_c = 12$ and 14 at stages (α) and (β) resemble those for the fluid phase. At the stage (γ), some fractions of clusters with $N_c = 12$ coalesce at the *fcc* marker; at this stage, a concentration to $W_6 \simeq 0.013$ takes place for clusters with $N_c = 14$. The smooth feature of $g(r)$ observed at the stage (γ) may be attributed to such a coexistence of the local *fcc* and *bcc* symmetries. At the stage (δ), only a small number of clusters with $N_c = 12$ which have no *fcc* or *hcp* structures remaining, and clusters with $N_c = 14$ have the *bcc* symmetry to a large extent.

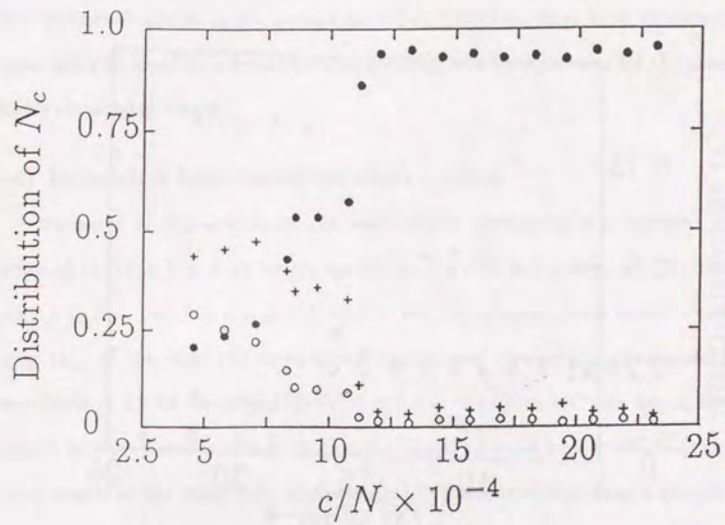

Fig. A.12 Evolution of the fractional numbers of particles with various N_c for the quench to $\Gamma = 300$: open circles, those with $N_c = 12$; crosses those with $N_c = 13$; and closed circles; those with $N_c = 14$.

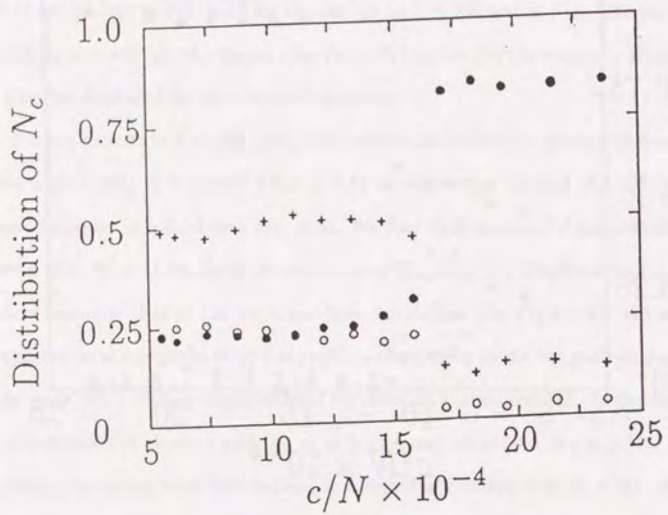

Fig. A.13 Evolution of the fractional numbers of particles with various N_c for the quench to $\Gamma = 400$: open circles, those with $N_c = 12$; crosses those with $N_c = 13$; and closed circles; those with $N_c = 14$.

All the analyses on the local orders mentioned above consistently show that the metastable states in both quenches have almost perfect local *bcc* structures. The metastable states in the present quenches, therefore, have local structures quite different from the mixture of local *fcc*, *hcp*, and *bcc* structures for the glass states obtained in Paper I.

(d) Extended bond-orientational orders

Evolution of the extended bond-orientational symmetries are displayed in terms of $G_6(r)$ in Fig. A.16 for the quench to $\Gamma = 300$ and in Fig. A.17 for the quench to $\Gamma = 400$. For the quench to $\Gamma = 300$, no extended order exists at the stage (a). At the stage (b), bond correlations extend themselves approximately two thirds of L. At the stage (c), $G_6(r) \simeq 0.1$ in the entire MC cell; hence, the system exhibits a degree of long-range order. For the quench to $\Gamma = 400$, $G_6(r)$ is short-ranged at the stage (α). At the stage (β) bond-correlation length extends to a half of L. Bond-orientational correlation becomes long-ranged at the stage (γ) to the same degree as with the stage (c) for the quench to $\Gamma = 300$. Final values of $G_6(r)$ in both quenches are about two thirds of the *bcc* value.

(e) Layered structures

One of the main concerns in the present simulations has been a possible formation of the layered structures and their relation to the periodic boundary conditions. For elucidation of such an issue, two-dimensional projection maps of particles have been constructed from various directions, to illustrate possible layered structures. We begin with isolating those particles inside a sphere of radius $L/2$, then rotate these as a whole by an angle ζ around the y axis and by η around

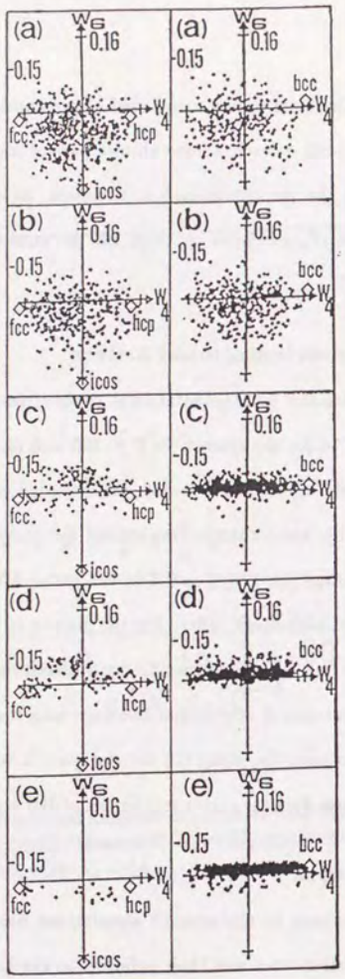

Fig. A.14 Evolution of two-dimensional (W_4, W_6) maps for the quench to $\Gamma = 300$: (left) is the particles with $N_c = 12$ shown by open circles; (right) is the particles with $N_c = 14$ shown by closed circles. Diamond markers correspond to (W_4, W_6) values for the *fcc*, *hcp*, *icosahedral*, and *bcc* clusters; for the *icosahedron*, we set $W_4 = 0$ here.

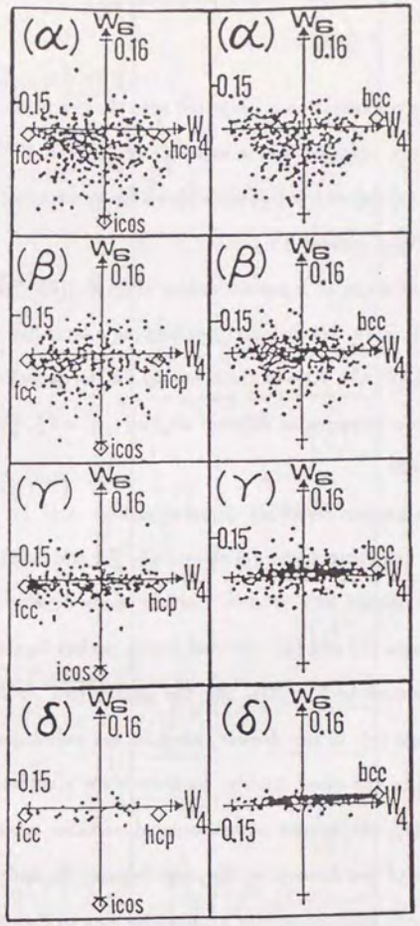

Fig. A.15 Evolution of two-dimensional (W_4, W_6) maps for the quench to $\Gamma = 400$: (left) is the particles with $N_c = 12$ shown by open circles; (right) is the particles with $N_c = 14$ shown by closed circles. Diamond markers correspond to (W_4, W_6) values for the *fcc*, *hcp*, *icosahedral*, and *bcc* clusters; for the *icosahedron*, we set $W_4 = 0$ here.

the z axis; the resulting configuration is projected onto the y–z plane. (Note that the particle positions are averaged over a sequence of $\Delta c/N \times 10^{-4} = 0.069$.) For each of the stages (a)–(e) and (α)–(δ), we have thus constructed maps from various angles $(\zeta, \eta) = (\frac{\pi}{40}i, \frac{\pi}{40}j)$ with $i, j = 1, 2, \cdots, 20$.

Such a collection of maps at a pre-nucleation stage (α) for the quench to $\Gamma = 400$ is shown in Fig. A.18. We find particles forming a layer-like structure in the map with $(\zeta, \eta) = (\frac{11\pi}{40}, \frac{2\pi}{5})$. Also at the stage (a) for the quench to $\Gamma = 300$, we find layered structures emerging at different angles $(\zeta, \eta) = (\frac{\pi}{4}, \frac{\pi}{5})$ from those for the quench to $\Gamma = 400$.

Evolutions of such particle layers are depicted in Fig. A.19 for the quench to $\Gamma = 300$ viewed at the same angles $(\zeta, \eta) = (\frac{11\pi}{40}, \frac{2\pi}{5})$ and in Fig. A.20 at $(\zeta, \eta) = (\frac{\pi}{4}, \frac{\pi}{5})$ for the quench to $\Gamma = 400$. Particle layers develop over a half of the sphere at the stages (b) and (β). We find nearly perfect layers already at the stage (c) for the quench to $\Gamma = 300$. For the quench to $\Gamma = 400$, we find two domains at the stage (γ): in one domain, particles are well-ordered forming a nearly perfect layers; in the other domain, particles show a rather disordered feature. At the stage (δ), the domain of well-ordered particles spread over the cell. Such an emergence of two domains at the stage (γ) may be understood as a result of the coexistence of local *fcc* and *bcc* symmetries seen in Fig. A.15.

If the formation of layered structures has anything to do with the periodic boundary conditions in the cell, orientations of emerged layers would have a cubic symmetry. We single out the two cases, where the layered structures are found at the pre-nucleation stages. The two values of the angle ζ are very close to each other and approximately take on $\frac{\pi}{4}$, a half the characteristic angle for the cubic

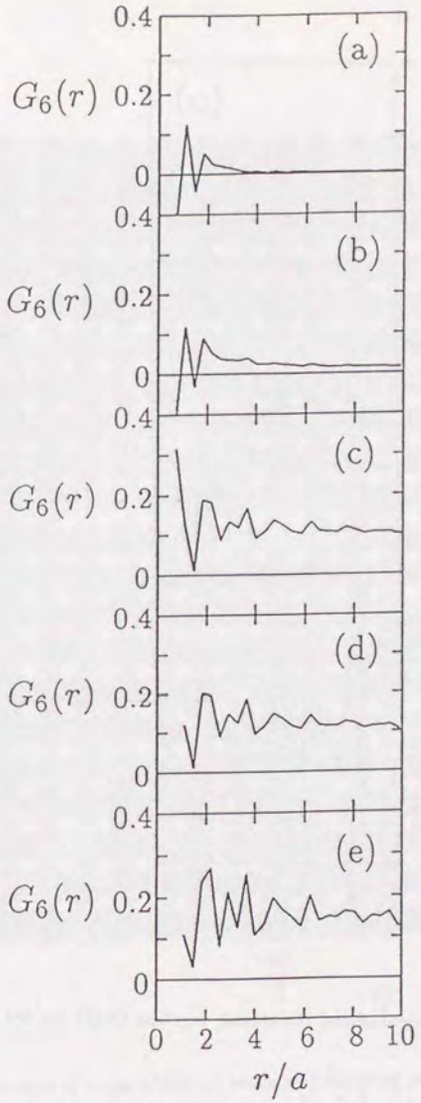

Fig. A.16 Evolution of bond-orientational correlation function $G_6(r)$ for the quench to $\Gamma = 300$.

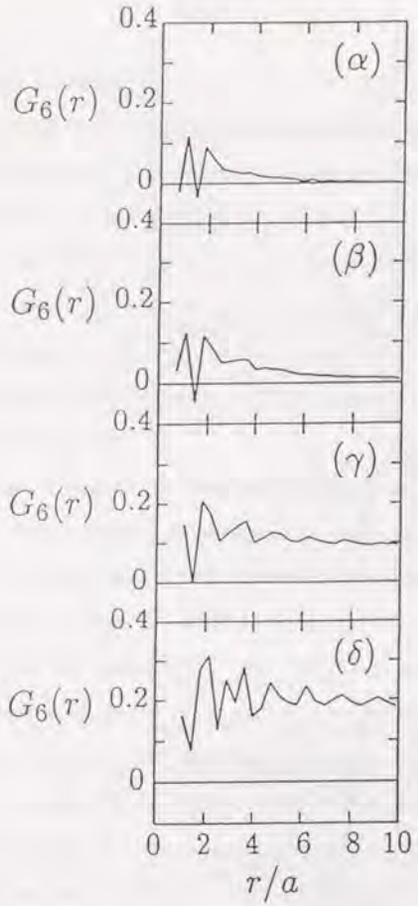

Fig. A.17 Evolution of bond-orientational correlation function $G_6(r)$ for the quench to $\Gamma = 400$.

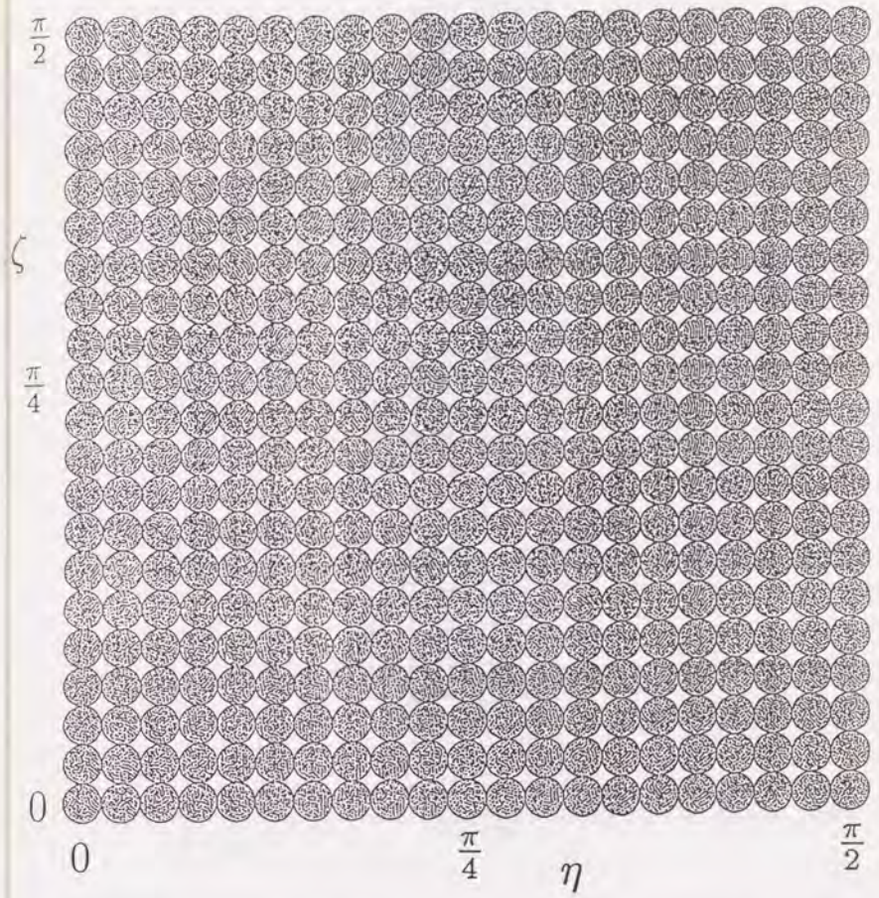

Fig. A.18 A collection of maps which are made by projecting particles onto the y–z plane with various rotation angles $(\zeta, \eta) = (\frac{\pi}{40}i, \frac{\pi}{40}j)$, $i, j = 1, 2, \cdots, 20$.

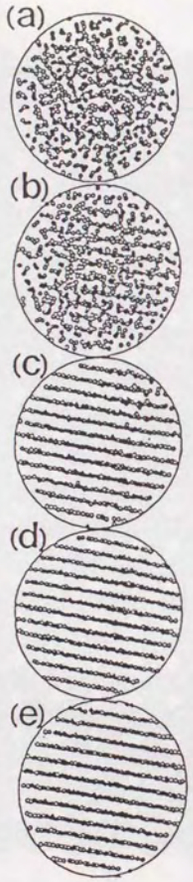

Fig. A.19 Evolution of layered structures for the quench to $\Gamma = 300$ viewed at angles $(\zeta, \eta) = (\frac{11\pi}{40}, \frac{2\pi}{5})$.

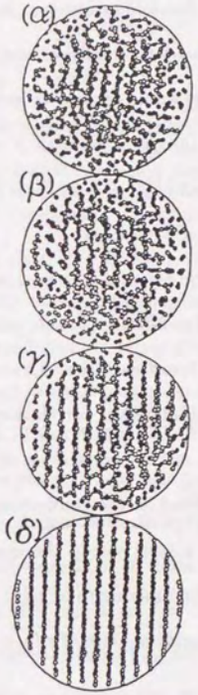

Fig. A.20 Evolution of layered structures for the quench to $\Gamma = 400$ viewed at angles $(\zeta, \eta) = (\frac{\pi}{4}, \frac{\pi}{5})$.

symmetry. On the other hand, the values of the angle η in both cases are multiples of $\frac{\pi}{5}$, characteristic angles for the five-fold symmetry. Further investigation on the relation between the periodic boundary condition and the emergence of layered structures in a pre-nucleation stage would require an increased number of samples.

In the metastable states for the quenches with $N = 432$, we found layers at angles $(\zeta, \eta) = (\frac{\pi}{20}, \frac{\pi}{2})$, $(\frac{3\pi}{20}, 0)$, and $(\frac{17\pi}{40}, \frac{\pi}{40})$. In these cases, we could not detect such an indication of possible cubic symmetry.

Since all the particles reside on layers at the final stages (e) and (δ) as in the case of a lattice structure, two-dimensional particle positions on the layers may contain some imperfections. We investigate the character of the final states, (e) and (δ), from the point of view of intralayer correlations by the two-dimensional radial distribution function $g_2(r)$, and the correlation of bond angles $P(\theta)$ around a particle. Here, bonds are redefined as the connecting lines between a particle and its neighboring particles on a layer inside the circle of radius $2.5a$, which correspond approximately to the first minimum of $g_2(r)$. We note that about 97% of the particles have 6 particles inside a circle of $r/a = 2.5$ at the stages (e) and (δ).

Figure A.21 shows $g_2(r)$ and $P(\theta)$ at the stages (e) (upper) and (δ) (lower). At the bottom of the figure, intralayer correlations on the most closely packed planes for each structure are shown: vertical solid-lines depict the correlations for the *fcc-hcp* hexagonal planes; vertical dashed-lines, for the *bcc* {110} planes. Peak positions and heights of $g_2(r)$ and $P(\theta)$ are nearly identical to the *bcc* structures. Nevertheless, we find substantial degrees of deviation from the *bcc* structures: for instance, $P(\theta)$ around $\theta \sim \pi/2$ and $g_2(r)$ around $r \sim 2.5a$ do not vanish. Both

for the stages (e) and (δ), imperfections are found in the particle correlations on the layers.

(f) Motion of defects

Since u shows transient behaviors in the metastable region, it appears probable that the final state may transform into a purely *bcc* crystalline state by a further extension of the MC samplings. To estimate the probability of such a transition, we investigate the character of the intralayer imperfections and their dynamics during the metastable state by tracing the motion of particles.

Following three periods are defined in terms of $c/N \times 10^{-4}$: (1) 12.6–16.7, (2) 16.7–20.8, (3) 20.8–24.9. In each of the three periods, we first single out particles in a layer (exemplified in Figs. A.19 and A.20) at the final configuration, and project these (solid circles) on the x–z plane. Then their positions are traced back to the beginning of the period (open circles) with an equal interval of $\Delta c/N \times 10^{-4} = 0.21$. Such maps, extended to the size $2L \times 2L$ to see the linked motion of particles, are depicted in Fig. A.22 for the quench to $\Gamma = 300$: (top) corresponds to the period (1); (middle), for the same layer as top, but to the period (2); (bottom), for the same layer as top, but to the period (3). The pairs of vertical noisy lines depict the projections of the particle positions during the corresponding period on a y–z plane: the left line is for $x < 0$ particles; the right, for $x > 0$ particles. For the quench to $\Gamma = 400$, we depict in Fig. A.23 such a map for the period (3).

The imperfections found in these analyses can be classified into three types: (A) a particle outside the layer (belonging mostly to one of the adjacent layers) in the open-circle configurations, (B) an interstitial (or an extra particle outside the adjacent layers) in the layer, and (C) a vacancy in the open-circle configurations.

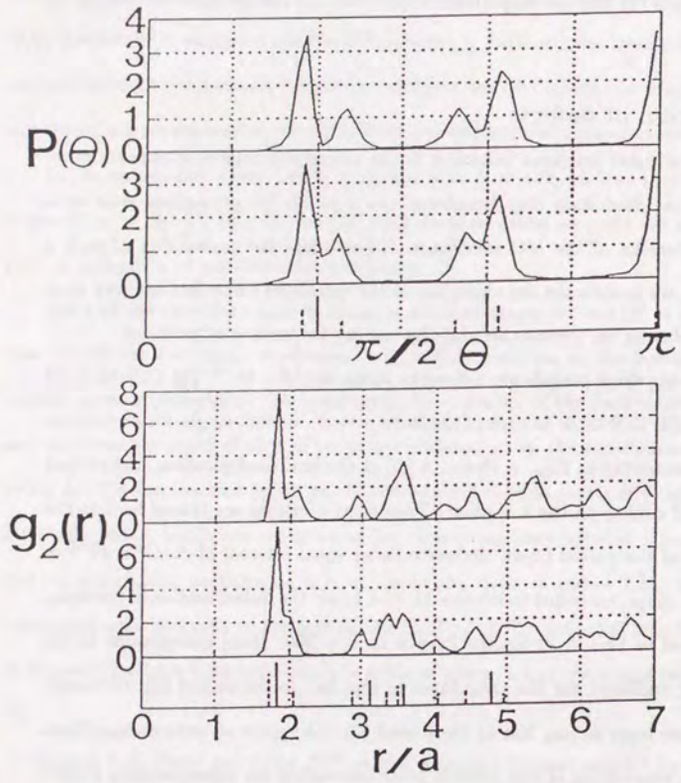

Fig. A.21 Bond-angle distribution $P(\theta)$ and two-dimensional radial distribution function $g_2(r)$ between intralayer particles in the stages (e) [upper] and (δ) [lower]. The bottom figures show the corresponding quantity for the *bcc* (dashed lines) and for the *fcc*, i.e., hexagnal, (solid lines) lattices.

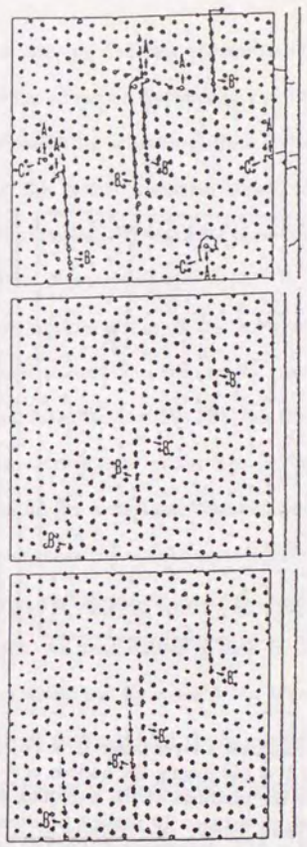

Fig. A.22 Motions of particles in and near a layer (size: $2L \times 2L$) projected onto a x–z plane for the quench to $\Gamma = 300$ during the periods $c/N \times 10^{-4} = 12.6$–$16.7$ (top), 16.7–20.8 (middle), and 20.8–24.9 (bottom). The open circles denote the positions at the beginning of a period, the solid circles, those at the end; in between 19 particle positions follow at an equal interval of $\Delta c/N \times 10^{-4} = 0.21$. Examples of type (A), (B), and (C) imperfections are shown. The pairs of vertical noisy lines (left for $x < 0$, right for $x > 0$) depict the projections of the particle motions onto a y–z plane.

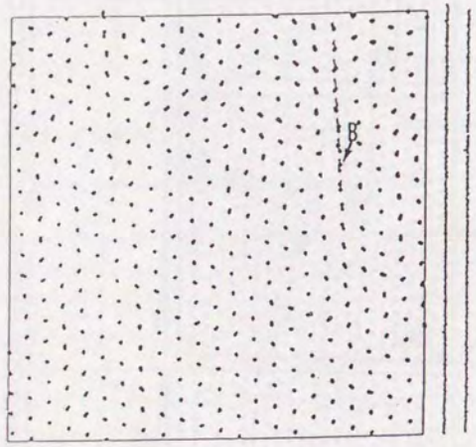

Fig. A.23 Motions of particles in and near a layer (size: $2L \times 2L$) projected onto a x–z plane for the quench to $\Gamma = 400$ during the periods $c/N \times 10^{-4} = 20.8$–$24.9$. The open circles denote the positions at the beginning of a period, the solid circles, those at the end; in between 19 particle positions follow at an equal interval of $\Delta c/N \times 10^{-4} = 0.21$. A example of type (B) imperfection is shown. The pair of vertical noisy lines (left for $x < 0$, right for $x > 0$) depicts the projections of the particle motions onto a y–z plane.

For the quench to $\Gamma = 300$, we find real transitions during the period (1) (top of Fig. A.22) in the forms of merges between (A) and (C) and between (B) and (C), and of a transformation (or a settling) from (A) to (B), as well as virtual transitions within (B); the virtual transition usually ceases at a return to the original interstitial configurations. We attribute these real transitions as the causes of the transient behaviors of u around $c/N \times 10^{-4} = 14.0$. During the periods (2) and (3) (middle and bottom of Fig. A.22), however, no imperfections of the types (A) and (C) appear to remain in the system; transient behaviors in u arise only through the virtual transitions within (B). For the quench to $\Gamma = 400$ (Fig. A.23), we find only virtual transitions within type (B) imperfections in the period (3). The jitters observed in the metastable states shown in Figs. A.6 and A.7 are attributed to those incidents of the virtual transitions.

We thus characterize the imperfections at the final states in both quenches as intralayer interstitials. An annihilation of such an isolated interstitial by the MC sampling processes would call for a slight but homogeneous compression of a configuration of particles that surround the interstitial in the layer, concurrent with appropriate compressions of the particle configurations in the neighboring layers, in such a way as to preserve the overall *bcc*-crystalline structures. We speculate the probability of such a sampling, if not zero, would be extremely small.

(g) Quench to Γ =800

One expects a possibility that a further increase in Γ might introduce some additional changes to the final state since the deviation of Madelung energy in

units of $k_{\rm B}T$ from the purely *bcc*-crystalline state grows proportional to Γ. Besides, a state where Γ parameter is as large as 1000 may become necessary when application of the MC results is considered in the the outer crustal matter of the neutron stars. We therefore perform an additional MC simulation for a further quench. Starting from the final state for the quench to $\Gamma = 400$ (i.e., at $c/N \times 10^{-4} = 25.0$), we increase Γ stepwise through 600 to 800, and maintain it until $c/N \times 10^{-4} = 35.0$ as shown in Fig. A.1 (bottom).

Excess internal-energies u, depicted in Fig. A.24, stay about 0.2 above the *bcc* value (dashed line), though transient behaviors are seen at around $c/N \times 10^{-4} = 28.5$ and 33.0. No change in $g(r)$ is observed during the run after the quench to $\Gamma = 800$. Figure A.25 shows such a $g(r)$ at $c/N \times 10^{-4} = 32.4$. In Fig. A.26, motion of particles in the same layer as in Fig. A.23 is described on a x–z plane from open circles to solid circles during the period $c/N \times 10^{-4} = 30.7$–$34.8$ with an equal interval of $\Delta c/N \times 10^{-4} = 0.21$. A pair of vertical noisy lines depict the projections of the particle positions onto a y–z plane: the left line is for $x < 0$ particles; the right, for $x > 0$ particles. We find that motions of particles are locked around their original positions.

It has not been possible to remove the defects produced during the rapid quenches through application of a further quench to the system.

V. Supercooled fluid state

The OCP has the lowest free energies for the *bcc* phase at $\Gamma > \Gamma_{\rm m} = 180$. MC simulations with $N \leq 1024$, however, indicates that the supercooled fluid OCP at $\Gamma = 200$ appears stable. The stability of the OCP in the supercooled fluid state would be attributed to a limited span of simulations and to the periodic boundary

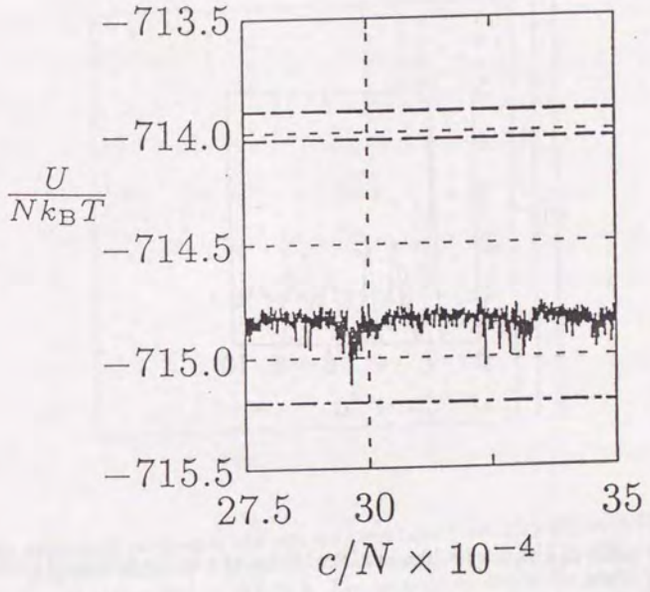

Fig. A.24 Evolution of the normalized excess internal-energy for the further quench to $\Gamma = 800$. The dashed lines indicate the levels predicted from the extensions of the fluid internal-energy formulas [upper: Eq. (A.11), lower: Eq. (A.12)]; the dot-dashed line, the *bcc* crystalline level via Eq. (A.13).

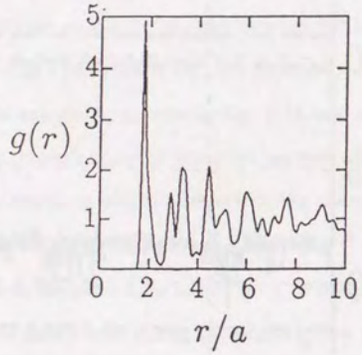

Fig. A.25 The radial distribution function at $c/N \times 10^{-4} = 32.4$ for the additional quench to $\Gamma = 800$.

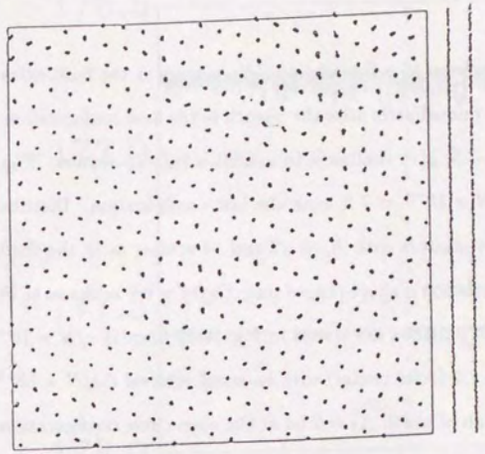

Fig. A.26 Motions of particles in and near the same layer (size: $2L \times 2L$) as in Fig. A.23, projected onto a x–z plane for the additional quench to $\Gamma = 800$ during the period $c/N \times 10^{-4} = 30.7$–$34.8$. The open circles denote the positions at the beginning of a period, the solid circles, those at the end; in between 19 particle positions follow at an equal interval of $\Delta c/N \times 10^{-4} = 0.21$. The pair of vertical noisy lines (left for $x < 0$, right for $x > 0$) depicts the projections of the particle motions onto a y–z plane.

conditions. We study the stability of the supercooled fluid OCP with $N = 1458$ by performing an additional long run. Starting with the fluid state at $\Gamma = 160$, we apply a sudden quench to $\Gamma = 200$ at $c = 0$. The evolution is monitored until $c/N \times 10^{-4} = 7.5$.

Figure A.27 shows u as a function of c/N. u stays at the fluid extrapolation level (dashed lines) immediately after the quench to the final configuration. During $c/N \times 10^{-4} = 0.6$–7.5, $g(r)$ continues to exhibit a smooth feature. Figure A.28 depicts $g(r)$ at $c/N \times 10^{-4} = 7.2$, near the last configuration. Distributions of (W_4, W_6) values for clusters with $N_c = 12$ and 14 scatter as in the fluid case at $\Gamma = 160$. Bond correlation is short-ranged since $G_6(r) \simeq 0.0$ as shown in Fig. A.29. Diffusive motions of particles are traced in Fig. A.30 from at $c/N \times 10^{-4} = 5.7$ (open circles) to at 7.3 (solid circles) with an equal interval $\Delta c/N \times 10^{-4} = 0.21$ for those inside a slab of width $\Delta z = 2.0a$ at the open circle configurations. In all the analyses, we found no indications of phase transitions.

VI. Discussion and concluding remarks

In the present simulations, rapidly quenched OCPs have solidified into *bcc* monocrystalline states with defects. Microscopic structures in these final states are significantly different from those in the polycrystalline glasses obtained in the former simulations with $N = 432$. Since the quenching procedures are almost the same in both simulations, the difference in the final states should be attributed to the difference in N. The choice of N at a *bcc* number appears to bear no essential consequences to the solidification processes since substantial numbers of imperfections from the perfect *bcc* crystalline states have been observed in both metastable states. By considering the effects of the periodic boundary conditions

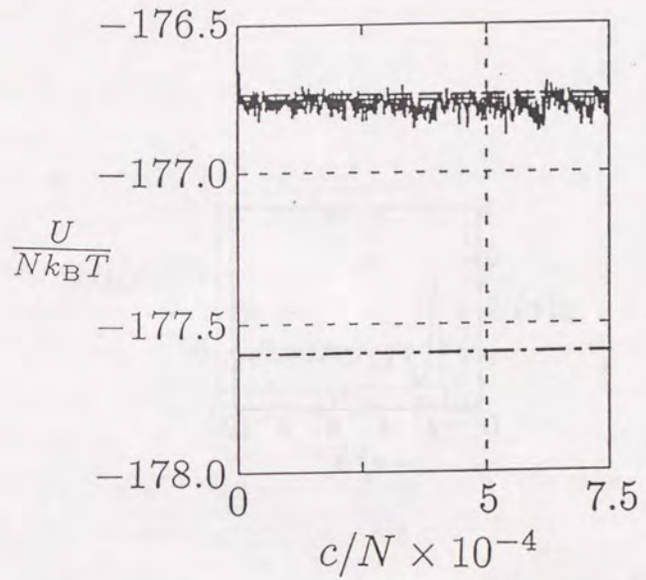

Fig. A.27 Evolution of the normalized excess internal-energy for the quench to $\Gamma = 200$. The dashed lines indicate the levels predicted from the extensions of the fluid internal-energy formulas [upper: Eq. (A.11), lower: Eq. (A.12)]; the dot-dashed line, the *bcc* crystalline level via Eq. (A.13).

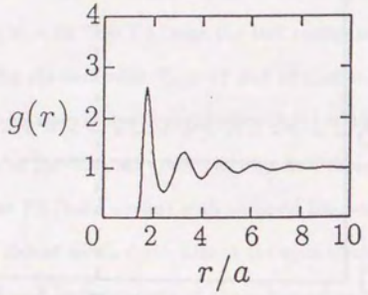

Fig. A.28 The radial distribution function at $c/N \times 10^{-4} = 7.2$ for the quenche to $\Gamma = 200$.

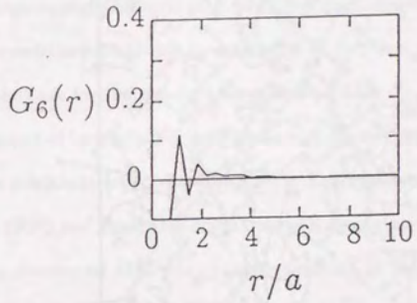

Fig. A.29 Bond-orientational correlation function $G_6(r)$ at $c/N \times 10^{-4} = 7.2$ for the quench to $\Gamma = 200$.

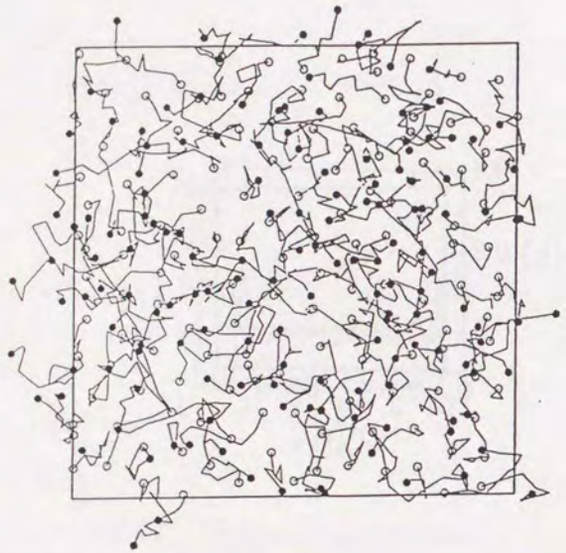

Fig. A.30 Motion of particles inside a slab of width $\Delta z = 2.0a$ for the quench to $\Gamma = 200$ during the period $c/N \times 10^{-4} = 5.7$–7.3. The open circles denote the positions at the beginning of a period, the solid circles, those at the end; in between 8 particle positions follow at an equal interval of $\Delta c/N \times 10^{-4} = 0.21$.

as to hinder the motion of particles for smaller N, we may explain the mechanism of the formation of the metastable states in both simulations: When the OCP is rapidly quenched to $\Gamma > \Gamma_m$, particle layers emerge first in an arbitrary direction, which would favor a *fcc-hcp* local structures. Subsequently the system may transform itself into a *bcc* crystalline state if N is large enough, since the Helmholtz free energies assume the lowest values in the *bcc* phase. In case that N is not large enough, however, the motion of particles would be hindered by the boundary conditions resulting in a mixture of *fcc*, *hcp*, and *bcc* structures; this would be the case for the simulations with $N = 432$.

Emergence of layered structures preceding the nucleation may be a characteristics of the solidification processes in OCPs. Experiments (Gilbert, Bollinger, and Wineland, 1988) and computer simulations (Rahman and Schiffer, 1986; Schiffer, 1988) have discovered that the charged particles in an external confining field freeze into a state in which shell (layer) structures are formed in the field direction. The long-rangedness of the Coulomb force, which is a feature common to both systems, might be a cause for the emergence of a layered structure in these rapidly quenched systems.

In the present simulations, the temperature is lowered by about $\frac{1}{2}$ during the very short span of time $\omega_p t \sim 3 \times 10^3$ (evaluated through Eq. (A.5)). To obtain metastable glassy states in the MC simulations with a large number of N ($\geq$ 1458), a OCP would have to be quenched to a value of Γ much higher than 300–400.

Part B: CONDUCTIVITIES AND SHEAR MODULI OF THE QUENCHED SOLIDS

I. Introduction

The crustal matter, forming an outer envelop of a neutron star with a thickness of several hundred meters (e.g., Shapiro and Teukolsky, 1983), may be modeled fairly well by a OCP consisting mostly of Fe ($Z = 26, A = 56$) with a mass density $\rho_{\rm m}$ and a temperature T in the ranges of 10^4–10^9 g/cm^3 and 10^6–10^8 K, where Z and A refer to the charge and mass numbers. The $r_{\rm s}$ parameter of electrons, ratio of the Wigner-Seitz radius to the Bohr radius, takes on a value,

$$r_{\rm s} = 1.8 \times 10^{-2} \left(\frac{Z}{26}\right)^{-1/3} \left(\frac{A}{56}\right)^{1/3} \left(\frac{\rho_{\rm m}}{10^6 {\rm g/cm}^3}\right)^{-1/3}, \qquad \text{(B.1)}$$

ranging 10^{-2}–10^{-1}. The Fermi energy of electrons, $E_{\rm F} = mc^2[\sqrt{1 + 0.0002 r_{\rm s}^{-2}} - 1]$, is $\sim$ 1Mev at $r_{\rm s} = 0.01$ and is far larger than $mZ^2e^4/2\hbar^2 \sim 10$ kev, the characteristic interaction energy between an electron and an ion. The system of electrons may thus be regarded as a uniform background of negative charges neutralizing the average space charge of the positive ions. The screening effects of relativistically degenerate electrons on the Madelung energy will be investigated quantitatively in Sec. B.II.

The Coulomb coupling parameter of ions, defined in Eq. (A.1), is written as

$$\Gamma = \frac{(Ze)^2}{ak_{\rm B}T} = 4 \times 10^2 \left(\frac{Z}{26}\right)^2 \left(\frac{A}{56}\right)^{-1/3} \left(\frac{T}{10^7 {\rm K}}\right)^{-1} \left(\frac{\rho_{\rm m}}{10^6 {\rm g/cm}^3}\right)^{1/3}. \qquad \text{(B.2)}$$

Freezing transition of ions is well expected in the cooling process of a neutron star, since the transition to a *bcc*-crystalline phase is predicted to occur at $\Gamma = 178$–180.

It has been shown by Gudmundsson, Pethick, and Epstein (1982) that the $\rho_{\rm m}$–T regime specified above overlaps bulk of the *sensitivity strip*, where the opacity is needed most precisely in the calculation of a temperature profile from inside to outside of a neutron star. The electric conductivity of the crustal matter is essential in a theoretical estimate for the decay rate of the magnetic field in a neutron star.

Scattering rates of the electrons governing the opacities and conductivities in such a dense material are delicately affected by the microscopic detail of interparticle correlations. The conductivities in a *bcc*-crystalline OCP were approached by Flowers and Itoh (1976) in the single phonon scattering approximation; those in a glassy OCP were considered by Ichimaru *et al.* (1983) and by Iyetomi and Ichimaru (1983a).

The elasticity of crustal matter is essential for prediction of nonradial oscillation spectra (McDermott *et al.*, 1985, 1988) in neutron stars and for investigation of the glitch phenomena (Pandharipande, Pines, and Smith, 1976) in pulsars. McDermott *et al.*, (1985) first analyzed nonradial oscillations of neutron stars, modeled as three-component stars consisting of fluid interiors, solid crusts, and fluid "oceans." Novel features in the analyses were the predictions of the bulk and interfacial modes, associated with the non-vanishing shear modulus of the crustal solid, with characteristic periodicity on the order of milliseconds.

The value of the shear modulus used by McDermott *et al.* (1985, 1988) for the crust was one of the "Fuchs values" (Mott and Jones, 1936) appropriate to the *bcc* Coulomb crystal at zero temperature and a specific mode of deformation. Generally, however, the stress-strain relations in solids should be expressed through

tensors of higher order (Mott and Jones, 1936; Landau and Lifshitz, 1970). The shear modulus tensor should depend sensitively on the temperature, as the melting transition is approached. The value used in the calculations in fact, corresponded to the largest possible value in the tensorial shear moduli of the *bcc* Coulomb solids. Elucidation of the temperature dependence of the shear modulus tensor has been an outstanding problem in condensed-plasma physics and astrophysics.

In Part B of this Thesis, the conductivities and the shear modulus tensors are evaluated at various temperatures for the MC-simulated solids and supercooled fluids. Two types of states are considered for the solids: quenched and crystalline states. The quenched (Q) states have been obtained by the MC simulation method with $N = 1458$ at $\Gamma = 300$, 400, and 800 as elucidated in Part A. We newly created *bcc* crystalline (C) states by the MC method with $N = 1458$. In the simulations, particles were placed initially at the *bcc* lattice points in the cell, and $(1 \sim 2) \times 10^6$ MC configurations were generated subsequently at $\Gamma = 200$, 300, 400, and 800. In each case thermalization has been ensured. The final states of the simulations maintain the cubic symmetry of the *bcc* lattice. We have a case of supercooled fluid (F) state at $\Gamma = 200$ as explained in Sec. A.V.

The conductivities are calculated through a precise evaluation of the scattering integrals as in Ichimaru *et al.* (1983a) and in Iyetomi and Ichimaru (1983) using the static structure factors $S(\vec{k})$ evaluated in each state. The results predict the conductivities lower by a factor greater than ~ 3 than those with the single-phonon approximation.

We present first principles study of the shear modulus tensor for Coulomb solids with inclusion of temperature-dependent effects. The free-energy increments (Mott and Jones, 1936; Nielsen and Martin, 1983) stemming from virtual

deformations of the resultant solids are then evaluated by MC samplings of the relevant Ewald sums; these evaluations lead to determination of the temperature-dependent shear-modulus tensors. Then we show a way to approximate the solid as an "isotropic" body by introducing an effective shear modulus through averages over directions.

To illustrate an effect of the shear modulus calculations, we recompute the nonradial oscillation modes of a particular model neutron star. The results are compared with those in the former calculations by McDermott *et al.* (1988).

The Part B is organized as follows: In Sec. B.II, applicability of the classical OCP model to the outer crustal matter is examined by evaluating the quantum effects of ions and screening effects of electrons. In Sec. B.III, the electric and thermal conductivities are calculated (Ogata and Ichimaru, 1990a). The temperature-dependant shear-modulus tensors are evaluated by the MC method in Sec. B.IV (Ogata and Ichimaru, 1990b). We apply the obtained shear modulus to the computation of the nonradial oscillation modes of a neutron star in Sec. B.V (Strohmayer *et al.*, 1991)

II. Quantum nature of ions and screening effects of electrons on the Madelung energy

We show that the Fe ions in the outer crustal material may be treated as classical particles and that their lowest-energy configuration assume the *bcc* structure at $T = 0$ even with the inclusion of electron screening.

When the OCP is in a fluid state, the ratio between the thermal de Broglie wavelength and a,

$$\Lambda = \frac{\hbar}{(Mk_{\rm B}T)^{1/2}a} = 2 \times 10^{-2} \left(\frac{A}{56}\right)^{-5/6} \left(\frac{\rho_{\rm m}}{10^6 {\rm g/cm}^3}\right)^{1/3} \left(\frac{T}{10^7 {\rm K}}\right)^{-1/2}, \quad \text{(B.3)}$$

measures the degree to which a quantum-mechanical description is necessitated in the behavior of the ions with mass M. For a crystalline OCP, the Einstein frequency in the Wigner-Seitz sphere model,

$$\omega_0 = \sqrt{\frac{4\pi(Zen)^2}{3\rho_{\rm m}}}\,, \tag{B.4}$$

goes into a description of the quantum states, so that the ratio

$$Y = \frac{\hbar\omega_0}{k_{\rm B}T} \tag{B.5}$$

measures involvement of the quantum effects.

Figure B.1 compares relative magnitude of those parameters on the $\rho_{\rm m}$–T plane for Fe materials in the outer crusts of neutron stars. Over the entire plane of Fig. B.1, $\Lambda \ll 0.1$, so that quantum effects are negligible for Fe ions in a fluid state. We observe in Fig. B.1 that Fe solids likewise behave classically over a significant domain on the $\rho_{\rm m}$–T plane.

Next, let us consider screening effects of relativistic degenerate electrons on ions. As is listed in Eq. (A3), the Madelung energy of the OCP assumes the lowest value for the *bcc* structure. At the same time, differences of the energies between the *fcc*, *hcp*, and *bcc* structures are only ~0.005%. Screening effects of electrons are expected to be small in magnitude in the outer crustal matter since $r_{\rm s} < 0.1$. However, there exists a possibility that the *bcc* structure may not be the lowest-energy structure.

We evaluate the correction term to the Madelung energy arising from the electron screening. In a linear response approximation, electron number density induced by the ion number density $n(\vec{k}) = \sum_{j=1}^{N} \exp(i\vec{k}\cdot\vec{r}_j)$ is expressed as

$$\delta n_e(\vec{k}) = \left[\frac{1}{\epsilon(\vec{k},0)} - 1\right] n(\vec{k}) \tag{B.6}$$

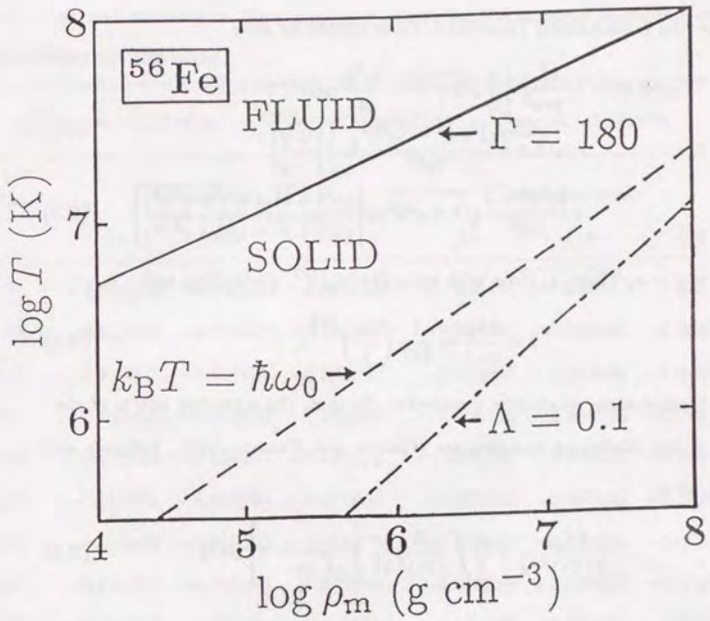

Fig. B.1 Comparison of parameters on $\rho_{\rm m}$–T plane for the iron material.

where $\epsilon(\vec{k},0) = 1-(4\pi e^2/k^2)\chi_0(\vec{k},0)$, $\chi_0(\vec{k},0)$ is the static free-electron polarizability. Since electrons are partially relativistic and perfectly degenerate, relativistic free-electron polarizability (Jancovici, 1962) should be used:

$$\chi_0(k,0) = -\frac{k_{\rm TF}^2}{4\pi e^2}\left\{\frac{2}{3}\sqrt{1+b^2} - \frac{2q^2 b}{3}\sinh^{-1} b + \sqrt{1+b^2}\frac{1+b^2-3q^2b^2}{6qb^2}\ln\left|\frac{1+q}{1-q}\right| + \frac{2q^2b^2-1}{6qb^2}\sqrt{1+q^2b^2}\ln\left|\frac{q\sqrt{1+b^2}+\sqrt{1+q^2b^2}}{q\sqrt{1+b^2}-\sqrt{1+q^2b^2}}\right|\right\} \quad \text{(B.7)}$$

where $k_{\rm TF} = e\sqrt{12\pi m_e n_e}/\hbar k_{\rm F}$ with $k_{\rm F} = (3\pi^2 n_e)^{1/3}$, $q = k/2k_{\rm F}$, and

$$b = \frac{\hbar k_{\rm F}}{m_e c} = \frac{1}{137}\left(\frac{9\pi}{4}\right)^{1/3} r_{\rm s}^{-1} \quad \text{(B.8)}$$

is the dimensionless relativistic parameter. So that, the screening effects of electrons on the Madelung energies are (Galam and Hansen, 1976; Ashcroft and Stroud, 1978),

$$\frac{\delta E_M}{N(Ze)^2/a} = \frac{a}{2}\int \frac{d\vec{k}}{(2\pi)^3}\frac{4\pi}{k^2}\left[\frac{1}{\epsilon(\vec{k},0)} - 1\right] S(\vec{k}) \quad \text{(B.9)}$$

where

$$S(\vec{k}) = \frac{\langle n(\vec{k}) n(-\vec{k})\rangle}{N}\,. \quad \text{(B.10)}$$

In the outer crustal matter, electron density parameter takes on values $r_{\rm s}\lesssim 0.015$ in solid phase (see Fig. B.1). Table B.1 shows Eq. (B.9) as a function of $r_{\rm s}$ for *fcc*, *hcp*, and *bcc* crystals; for comparison, values for non-relativistic free-electron polarizability ($b \to 0$) or the Lindhard polarizability (Lindhard, 1954) are also shown.

We find in Table B.1 that $\delta E_M/[N(Ze)^2/a]$ for relativistic degenerate electrons are insensitive to the difference in lattice structures compared with

TABLE B.1. Electron screening effects on the Madelung energies, $\delta E_M/[N(Ze)^2/a]$, for the *fcc*, *hcp*, and *bcc* lattices. For comparison, those for the non-relativistic free-electron polarizability are also listed.

$\frac{E_{\rm fcc}}{N(Ze)^2/a} = -0.895874$; $\frac{E_{\rm hcp}}{N(Ze)^2/a} = -0.895838$ $\frac{E_{\rm bcc}}{N(Ze)^2/a} = -0.895929$

$r_{\rm s}$	relativistic			non-relativistic		
	fcc	*hcp*	*bcc*	*fcc*	*hcp*	*bcc*
0.0	−0.015529	−0.015531	−0.015512	0.0	0.0	0.0
0.001	−0.015635	−0.015637	−0.015617	−0.001534	−0.001534	−0.001531
0.002	−0.015935	−0.015937	−0.015917	−0.003066	−0.003066	−0.003059
0.003	−0.016398	−0.016400	−0.016380	−0.004595	−0.004595	−0.004586
0.004	−0.016995	−0.016997	−0.016975	−0.006122	−0.006122	−0.006109
0.005	−0.017702	−0.017703	−0.017680	−0.007647	−0.007646	−0.007631
0.006	−0.018499	−0.018500	−0.018476	−0.009169	−0.009168	−0.009150
0.007	−0.019373	−0.019374	−0.019348	−0.010689	−0.010688	−0.010666
0.008	−0.020313	−0.020313	−0.020285	−0.012206	−0.012205	−0.012180
0.009	−0.021309	−0.021309	−0.021279	−0.013721	−0.013719	−0.013692
0.010	−0.022354	−0.022354	−0.022321	−0.015234	−0.015232	−0.015202
0.011	−0.023442	−0.022442	−0.023407	−0.016744	−0.016742	−0.016709
0.012	−0.024567	−0.024567	−0.024529	−0.018252	−0.018250	−0.018214
0.013	−0.025725	−0.025724	−0.025685	−0.019758	−0.019755	−0.019716
0.014	−0.026912	−0.026911	−0.026868	−0.021261	−0.021258	−0.021216
0.015	−0.028123	−0.028122	−0.028077	−0.022762	−0.022759	−0.022714

$E_M/[N(Ze)^2/a]$ in Eq. (A.3) and that lower the Madelung energies less than 3% for $r_s \leq 0.015$. As a result, the corrected Madelung energy assumes the lowest value again in the *bcc* structure. We add a remark that the relativistic degenerate electrons considerably screen the Coulomb potentials of ions even at $r_s = 0$ (Ichimaru and Utsumi, 1983). Such an effect becomes important in the theoretical evaluation of nuclear reaction rates in dense astrophysical materials especially for high-Z ions, which will be elucidated in Sec. D.V.

III. Electric and thermal conductivities

(a) Static structure factors

In the final states for the quenched OCPs (see Part A) at $\Gamma = 160$, 200, 300, and 800 as well as in the MC-simulated *bcc*-crystalline states at $\Gamma = 300$ and 800, we evaluate the static structure factors via,

$$S(\vec{k}) = \frac{1}{N}\left(1 - \sum_{\vec{G}\in\{\mathbf{RLV}\}} \delta_{\vec{k},\vec{G}}\right)\left\langle \sum_{j,l=1}^{N} \exp[-i\vec{k}\cdot(\vec{r}_j - \vec{r}_l)]\right\rangle . \qquad \text{(B.11)}$$

Here the average (in angle brackets) is carried out over an interval, $\Delta c = 2\times 10^5$, of MC configurations, and the contributions from the Bragg peaks at the *bcc* reciprocal-lattice vectors, $\{\mathbf{RLV}\}$, are subtracted. Raw data for $S(\vec{k})$ from the MC sequences generated are illustrated in Fig. B.2. Those data will be used for the calculation of the conductivities in the following section.

(b) Numerical results and discussion

The electric and thermal conductivities, σ and κ, of the crustal matter are formulated (Itoh *et al*, 1983) through the scattering rates of the relativistically

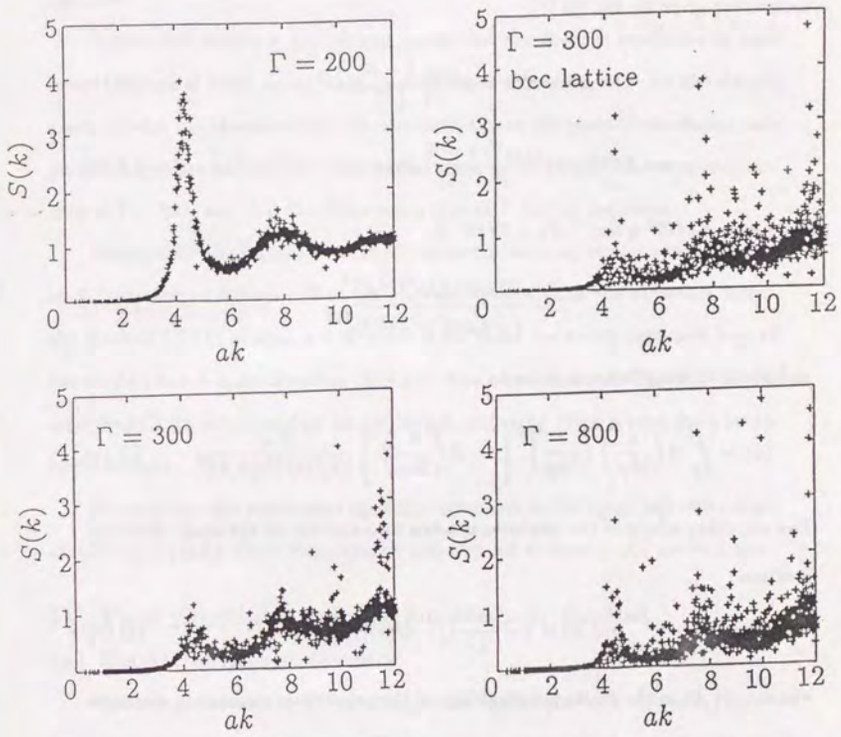

Fig. B.2 Structure factors for a fluid (top left), a *bcc* solid (top right), and quenched solids (bottom).

degenerate electrons against the dielectrically screened ion fields, whose structure factors are given by Eq. (B.11):

$$\sigma = 8.693 \times 10^{21} \frac{\rho_6}{A} \frac{1-R}{\langle S \rangle} \ (\mathrm{s}^{-1}) \ , \tag{B.12}$$

$$\kappa = 2.363 \times 10^{16} \frac{\rho_6 T_7}{A} \frac{1-R}{\langle S \rangle} \ (\mathrm{ergs\ cm^{-1}\ s^{-1}\ K^{-1}}) \ . \tag{B.13}$$

Here $\rho_6 = \rho_\mathrm{m}/10^6$ g cm^{-3}, $T_7 = T/10^7$ K,

$$R = \frac{1.018(Z/A)^{2/3}\rho_6^{2/3}}{1+1.018(Z/A)^{2/3}\rho_6^{2/3}} \tag{B.14}$$

and the scattering factor is given by

$$\langle S \rangle = \int_0^1 d\left(\frac{k}{2k_\mathrm{F}}\right) \left(\frac{k}{2k_\mathrm{F}}\right)^3 \left[1 - R\left(\frac{k}{2k_\mathrm{F}}\right)^2\right] \frac{S(k)}{[(k/2k_\mathrm{F})^2 \epsilon(k,0)]^2} \ . \tag{B.15}$$

The screening effects of the electrons is taken into account by the static dielectric function,

$$\epsilon(k,0) = 1 - \frac{4\pi e^2}{k^2}[1 - G(k)]\chi_0(k,0) \ , \tag{B.16}$$

where $\chi_0(k,0)$ is the static polarizability of the relativistic degenerate electrons given in Eq. (B.7) and $G(k)$ is the exchange local-field correction (Sato and Ichimaru, 1989).

Table B.2 lists the values of the electric and thermal conductivities calculated through the formulae (B.12) and (B.13). Separately, we have computed the same quantities by setting $G(k) = 0$ in Eq. (B.16), to see the effect of the exchange local-field correction. We have thereby found that the $G(k)$ acts to decrease the

conductivities by a mere 1% at most, which takes place in the fluid cases of $\Gamma = 160$ and 200.

Figure B.3 compares the present results for the thermal conductivity with other theoretical predictions. Analogous comparison can be made for the electric conductivity. We thus find that the conductivities in the present calculation take on values smaller by a factor of three than those in the single-phonon approximation at $\Gamma = 400$, and that the difference widen as Γ further increases.

Reasons for the increased rates of electron scattering in the present theory may be traced as follows. With an accurate knowledge of the structure factor, the formula (B.15) enables one to account for those scattering processes beyond the single-phonon approximation. The MC structure factors (see Fig. B.2) for the quenched OCPs accommodate an additional scattering effect arising from lattice imperfections.

Resistivities and conductive opacities enhanced in the quenched outer crust should significantly affect the magnetic and thermal evolution of a neutron star.

IV. First principles calculation of shear moduli

(a) Elastic-constant tensors

Free-energy increment δF resulting from application of a strain u_{ij} is expressed as (Landau and Lifshitz, 1970)

$$\delta F = \frac{1}{2} S_{ij,kl} u_{ij} u_{kl} \ . \tag{B.17}$$

Here $S_{ij,kl}$ is the elastic modulus tensor, the subscripts, i, j, k, and l, designate the Cartesian components, x, y, and z, and we adopt the summation convention for repeated subscripts. For an isotropic body, Eq. (B.17) reduces to

$$\delta F = \frac{1}{2}\lambda u_{ii}^2 + \mu u_{ik} u_{ik} \ . \tag{B.18}$$

TABLE B.2. Electric and thermal conductivities of Fe OCP at $T = 10^7$ K; [L] means a liquid state, [Q] quenched, and [C] crystalline lattice. The number in parentheses indicates a decimal exponent.

Γ	State	σ (s^{-1})	κ (ergs cm^{-1} s^{-1} K^{-1})
160	L	7.15 (18)	1.94 (13)
200	Q	1.32 (19)	3.59 (13)
300	Q	8.78 (19)	2.39 (14)
300	C	9.49 (19)	2.58 (14)
400	Q	1.84 (20)	4.99 (14)
800	Q	1.12 (21)	3.05 (15)
800	C	2.02 (21)	5.48 (15)

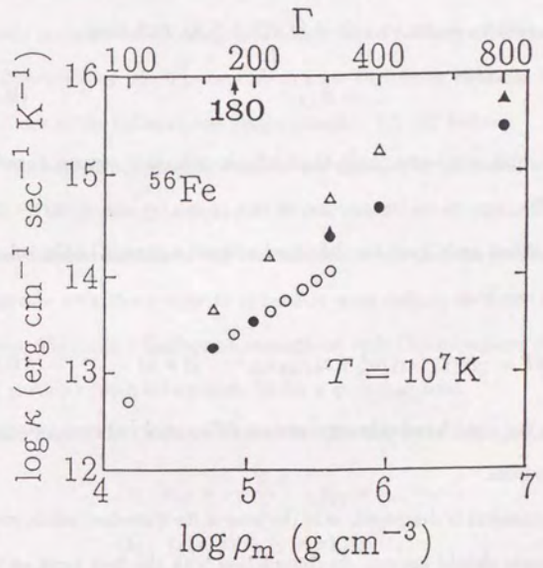

Fig. B.3 Thermal conductivity of Fe material: present (solid circles), crystalline simulations (solid triangles), Ichimaru *et al.* (1983) (open circles), Flowers and Itoh (1976) (open triangles).

The quantities λ and μ are Lamé coefficients.

The usual elastic constants (Mott and Jones, 1936), c_{rs} $(r, s = 1, 2, \ldots 6)$, are derived from the elastic modulus tensor through transformation $(ij, kl) \rightarrow (r, s)$ of the subscripts, $(xx, yy, zz, xy, yz, zx) \rightarrow (1, 2, 3, 4, 5, 6)$, such that

$$c_{rs} = S_{ij,kl} \ . \tag{B.19}$$

For a solid with cubic symmetry, only three elastic constants remain (Laudau and Lifshitz, 1970): $c_{11} = c_{22} = c_{33}$; $c_{12} = c_{21} = c_{23} = c_{32} = c_{31} = c_{13}$; $c_{44} = c_{55} = c_{66}$. When such a solid is deformed without a change in the volume (i.e., $\sum_i u_{ii} = 0$), one finds

$$\delta F = \frac{1}{2}(c_{11} - c_{12})u_{ii}^2 + c_{44}u_{ik}u_{ik} \qquad (i \neq k) \ . \tag{B.20}$$

The first term on the right-hand side represents a differential between two compressional deformations.

If the cubic symmetry is destroyed, as in the case of the quenched solids, more independent elements should appear. In conjunction with the first term on the right-hand side of Eq. (B.20), it is useful to define and introduce

$$\begin{aligned} b_{11} &= (2c_{11} - c_{12} - c_{31})/4 \ , \\ b_{22} &= (2c_{22} - c_{23} - c_{12})/4 \ , \\ b_{33} &= (2c_{33} - c_{31} - c_{23})/4 \ . \end{aligned} \tag{B.21}$$

The shear modulus tensor is then represented by the elements: b_{11}, b_{22}, b_{33}, c_{44}, c_{55}, c_{66}. For an isotropic body, all of these elements take on the same value which coincides with the shear modulus μ in Eq. (B.18).

(b) MC calculations of the shear moduli

The following steps have been taken in the calculations of the shear moduli for the MC simulated Coulomb solids. Since the crustal matter under consideration is virtually incompressible owing to the high Fermi pressure of dense electrons, we choose deformations which induce no changes in volume elements to the desired second order in the infinitesimal displacement ϵ. [cf. (2) below.]

(1) For the crystalline-simulated solids, we choose the Cartesian axes along the MC cell. For those solids produced in the quenched simulations, we perform rotational transformations of the coordinate axes so that the resultant Cartesian axes coincide with those close to symmetry axes defined in terms of the layered structures. Figure B.4 displays an example of such Cartesian axes chosen along a layer of particles (with interstitials B) for a quenched solid.

(2) In each case of the Coulomb solids, the following set of deformations is applied:

$$\begin{aligned} &\mathrm{D}_1 : u_{xx} = \epsilon + \frac{3}{2}\epsilon^2 \ , \quad u_{yy} = u_{zz} = -\frac{\epsilon}{2} \ . \\ &\mathrm{D}_2 : \ (x, y, z) \rightarrow (y, z, x), \ \text{to } \mathrm{D}_1 \ . \\ &\mathrm{D}_3 : \ (x, y, z) \rightarrow (z, x, y), \ \text{to } \mathrm{D}_1 \ . \\ &\mathrm{D}_4 : u_{xy} = u_{yx} = \frac{\epsilon}{2} \ , \quad u_{zz} = \frac{\epsilon^2}{4} \ . \\ &\mathrm{D}_5 : (x, y, z) \rightarrow (y, z, x), \ \text{to } \mathrm{D}_4 \ . \\ &\mathrm{D}_6 : (x, y, z) \rightarrow (z, x, y), \ \text{to } \mathrm{D}_4 \ . \end{aligned}$$

In these deformations, an elementary volume is kept invariant up to order ϵ^2, so that the derivatives, $dv/d\epsilon$ and $d^2v/d\epsilon^2$ [cf. (4) below], may be calculated through Ewald sums without changing the MC cell volume $(= L^3, \ L = (4\pi N/3)^{1/3}a)$. The deformations, D_1 and D_4, are depicted in Figs. B.5a and B.5b.

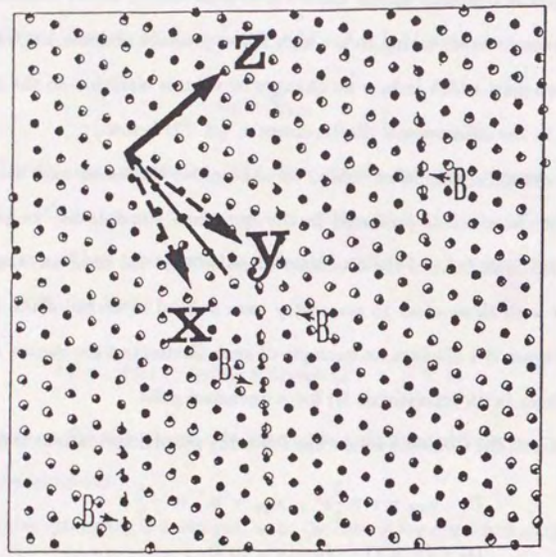

Fig. B.4 Schematic view of the Cartesian axes for the quenched solid (see Fig. A.23), which are chosen so that x and y are out of the layer at angles by a half of $\pi/2$ radians while z axis is on the layer along one of the axes for the resultant quasi-*bcc* structures.

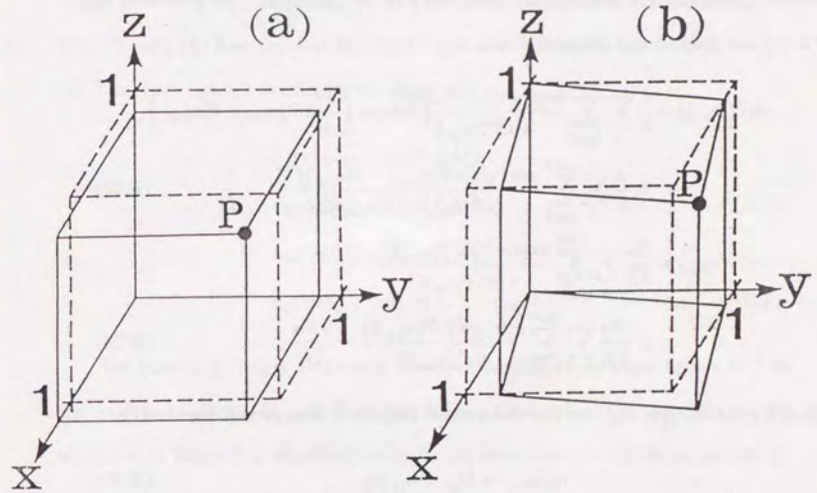

$P(1+\epsilon+\frac{3\epsilon^2}{2}, 1-\frac{\epsilon}{2}, 1-\frac{\epsilon}{2})$ $P(1+\frac{\epsilon}{2}, 1+\frac{\epsilon}{2}, 1+\frac{\epsilon^2}{4})$

Fig. B.5 Schematic views of the deformation: (a) D_1; (b) D_4.

(3) Let v be defined by

$$v(u_{lm}) = \frac{1}{2}\sum_{p\neq q}^{N} \Phi\{\vec{r}_p(u_{lm}) - \vec{r}_q(u_{lm})\} + U_0(u_{lm}) \ , \tag{B.22}$$

where $\vec{r}_p$ denotes the position vector of the p-th MC particle. The potentials in (B.22) are defined and calculated as

$$\begin{aligned}\Phi(\vec{r}(u_{lm})) =& \frac{a}{L}\sum_i \sum_{t\neq 0}^{\pm\infty} \frac{\exp(-\pi|t\vec{\alpha}^i(u_{lm})|^2)}{\pi|t\vec{\alpha}^i(u_{lm})|^2} \cos\left(\frac{2\pi}{L} t\vec{\alpha}^i(u_{lm})\cdot\vec{r}(u_{lm})\right) \\ &+ \frac{a}{L}\sum_i \sum_{t=0}^{\pm\infty} \frac{\mathrm{erfc}(\sqrt{\pi}|t\vec{\alpha}^i(u_{lm}) - \vec{r}(u_{lm})/L|)}{|t\vec{\alpha}^i(u_{lm}) - \vec{r}(u_{lm})/L|} - \frac{a}{L} \ , \end{aligned} \tag{B.23}$$

$$\begin{aligned} U_0(u_{lm}) =& \frac{Na}{2L}\sum_i \sum_{t\neq 0}^{\pm\infty} \frac{\exp(-\pi|t\vec{\alpha}^i(u_{lm})|^2)}{\pi|t\vec{\alpha}^i(u_{lm})|^2} \\ &+ \frac{Na}{2L}\sum_i \sum_{t\neq 0}^{\pm\infty} \frac{\mathrm{erfc}(\sqrt{\pi}|t\vec{\alpha}^i(u_{lm})|)}{|t\vec{\alpha}^i(u_{lm})|} - \frac{3Na}{2L} \ , \end{aligned} \tag{B.24}$$

Here t is an integer; u_{lm} are the elements of the strain tensors specified in (2);

$$r_i(u_{lm}) = (\delta_{ik} + u_{ik})r_k \ , \tag{B.25}$$

with δ_{ik} representing Kronecker's delta; the unit Cartesian vectors, $\vec{a}^i$, are analogously transformed as

$$a^i_j(u_{lm}) = (\delta_{jk} + u_{jk})a^i_k \ ; \tag{B.26}$$

the vectors, $\vec{\alpha}^i(u_{lm})$, orthogonal to $\vec{a}^j(u_{lm})$ are then defined as $(i \neq j \neq k)$

$$\vec{\alpha}^i(u_{lm}) = \vec{a}^j(u_{lm}) \times \vec{a}^k(u_{lm}) \ ; \tag{B.27}$$

and the error function complement is

$$\mathrm{erfc}(x) = 1 - \frac{2}{\sqrt{\pi}}\int_0^x \exp(-t^2)dt \ . \tag{B.28}$$

(4) In each case of the deformations D_m (m = 1, 2,..., 6), we calculate the MC averages:

$$f_m \equiv \left\langle \frac{d^2v}{d\epsilon^2} \right\rangle - \Gamma N \left\{ \left\langle \left(\frac{dv}{d\epsilon}\right)^2 \right\rangle - \left\langle \frac{dv}{d\epsilon} \right\rangle^2 \right\} \ , \tag{B.29}$$

where $d/d\epsilon = (\partial u_{ij}/\partial\epsilon)(\partial/\partial u_{ij})$. In the absence of thermal fluctuations (i.e., $T = 0$), only the first term on the right-hand side remains in Eq. (B.29).

(5) The shear moduli are finally obtained as

$$\begin{aligned} b_{11} =& (5f_1 - f_2 - f_3)/9 \ , \\ b_{22} =& (5f_2 - f_3 - f_1)/9 \ , \\ b_{33} =& (5f_3 - f_1 - f_2)/9 \ , \end{aligned} \tag{B.30}$$

$$c_{44} = f_4 \ , \quad c_{55} = f_5 \ , \quad c_{66} = f_6 \ . \tag{B.31}$$

We have accordingly evaluated the shear moduli at different values of Γ in the various cases (C, Q, and F in Sec. B.I) of Coulombic systems. The results are listed in Table B.3. We observe significant dependence of the shear moduli on temperatures and on the modes of deformations.

At $T = 0$ (i.e., $\Gamma = \infty$), the shear moduli are calculated from the first term of Eq. (B.29). The *bcc* crystalline values so calculated are also in Table B.3; for the *fcc* crystal, we find $b_{11} = b_{22} = b_{33} = 0.02066$ and $c_{44} = c_{55} = c_{66} = 0.1852$ in units of $n(Ze)^2/a$. These are identical to the Fuchs values cited in Mott and Jones (1936).

We remark that the effects of the fluctuations on the elastic constants were formulated by Squire, Holt, and Hoover (1969) for a classical ensemble of particles interacting through a central potential. Fluctuation effects in the screened metallic systems were subsequently studied (Wallace and Schiferl, 1984; Schiferl and

TABLE B.3. Elements of shear modulus tensors in units of $n(Ze)^2/a$. The numbers in the parentheses denote possible errors in the last digits. Only the common values are entered when b's or c's are equal.

Γ		b_{11}	b_{22}	b_{33}	c_{44}	c_{55}	c_{66}	$\mu_{\rm eff}$
∞	C		0.02454			0.1827		0.1194
800	C		0.024 (2)			0.174 (1)		0.114 (2)
800	Q	0.053 (2)	−0.007 (1)	0.057 (1)	0.181 (2)	0.171 (2)	0.133 (1)	0.111 (2)
400	C		0.025 (2)			0.167 (1)		0.110 (2)
400	Q	0.059 (3)	−0.009 (3)	0.062 (3)	0.170 (2)	0.169 (1)	0.121 (4)	0.107 (4)
300	C		0.025 (3)			0.157 (4)		0.104 (4)
300	Q	0.053 (1)	0.025 (2)	0.014 (3)	0.141 (3)	0.167 (2)	0.149 (3)	0.104 (3)
200	C		0.019 (3)			0.12 (1)		0.08 (1)
200	F		−0.004 (16)			0.05 (2)		0.03 (2)

Wallace, 1985). The present theory treats the cases of the long-range Coulomb interaction for the first time, where volume fluctuations should be avoided in the Ewald sums.

(c) Effective shear modulus

Though the elastic properties of crystalline solids are known to be anisotropic, it is sometimes convenient and useful for practical purposes if an effective shear modulus $\mu_{\rm eff}$ may be introduced approximately in the sense of Eq. (B.18).

We have approached this problem through averages of the dispersion relations for the transverse shear modes with respect to the polarizations and the directions of propagation. Let $\vec{u}$ be a displacement vector so that the strains are written as

$$u_{ij} = \frac{1}{2}\left(\frac{\partial u_i}{\partial r_j} + \frac{\partial u_j}{\partial r_i}\right) . \tag{B.32}$$

Its equations of motion are then given by (Landau and Lifshitz, 1970)

$$\rho\frac{\partial^2 u_i}{\partial t^2} = \frac{1}{2}S_{ij,ij}\left(\frac{\partial^2 u_i}{\partial r_j \partial r_j} + \frac{\partial^2 u_j}{\partial r_i \partial r_j}\right) , \tag{B.33}$$

where ρ is the mass density. Assuming plane-wave displacements, $u_i = a_i \exp(ik_l r_l - i\omega t)$, and multiplying (B.33) by a_i (with the summation convention), we find

$$\rho\omega^2 a^2 = \frac{1}{2}S_{ij,ij}(a_i^2 k_j^2 + a_i a_j k_i k_j) . \tag{B.34}$$

Averages of $\rho\omega^2/k^2$ over the directions of $\vec{k}$ and $\vec{a}$ (polarizations) with the constraint, $\vec{a}\cdot\vec{k} = 0$, yield

$$\mu_{\rm eff} = \{2(b_{11} + b_{22} + b_{33}) + 3(c_{44} + c_{55} + c_{66})\}/15 . \tag{B.35}$$

We add that the directional averages of f_4 in Eq. (B.29) over all the rotations of the Cartesian axes lead to the same expression (B.35). The values of $\mu_{\rm eff}$ are likewise entered in Table B.3.

It is instructive to note that the values of $\mu_{\rm eff}$ for the quenched solids remain approximately the same as those with the corresponding *bcc* crystals, although the shear moduli of the former solids deviate considerably from the cubic-symmetry values of the latter. Analogous observation can be made also between the *bcc* and *fcc* crystals at $T = 0$. Reason for these may be attributed to the relative insensitivity of Coulombic Ewald sums such as Eq. (B.23) to details of the microscopic particle configurations after averages over directions are carried out. We recall in these connections that the internal energies of Coulombic systems, involving analogous Ewald sums, are approximately the same for the *bcc*, *fcc*, and even isotropic ion-sphere configurations.

The values in Table B.3 suggest a possibility that the supercooled fluid at $\Gamma = 200$ may sustain a non-vanishing shear modulus of small magnitude. A definite conclusion on this issue, however, should be deferred until the nature of the equilibrium ensemble of the MC configurations generated in the supercooled fluid state is more carefully assessed.

V. Nonradial oscillation of neutron stars

Earlier, McDermott *et al.* (1985, 1988) calculated the nonradial oscillation spectra of neutron stars containing a solid crust using c_{44} for the *bcc* crystal at $T = 0$ as the shear modulus of the crustal matter. To illustrate an effect of the new temperature-dependent shear modulus tensors, we here recompute the nonradial oscillation modes of a particular model neutron star (Strohmayer *et al.*, 1991).

It has been shown (e.g., Schumaker and Thorne, 1983) that non-rotating, non-magnetic neutron stars can sustain a wealth of different oscillation modes. The modes are grouped into two classes, the *spheroidal* and *toroidal* modes, on the basis of the angular separation of variables in the solutions for the pulsation eigenfunctions. The toroidal modes in a completely fluid body are all degenerate at zero frequency, but the presence of a solid crust in a neutron star gives them non-zero frequencies. Such modes have been designated ${}_lt_n$ modes, where the first subscript denotes the order of the spherical harmonic $Y_{lm}(\theta, \phi)$ corresponding to that mode, and the second subscript is the overtone number, corresponding to the number of radial nodes in the eigenfunction. Toroidal modes in non-rotating, non-magnetic neutron stars are purely transverse oscillations, with no radial component to the displacement eigenfunction. The periods of the oscillations are a few milliseconds, with the higher overtones having successively shorter periods.

The spheroidal oscillation modes form a much richer class. These include the p-, g-, and f-modes familiar from conventional non-radial pulsation theory (e.g., Unno *et al.*, 1989) for purely fluid stars. We designate individual modes from these sub-classes as ${}_lp_n$, ${}_lg_n$, and ${}_lf$ modes, respectively. For each value of $l \geq 1$, there is only one f-mode, with a period of the order of 0.5 ms, while the p- and g-modes can have arbitrarily many overtones. The p-mode oscillations have periods less than about 0.1 ms, with higher overtones having progressively shorter periods.

A complication in the oscillation spectra that occurs in neutron stars is that the g-mode oscillations are split into two subclasses by the presence of the solid crust. One subclass, the ${}_lg_n^s$ modes, is confined almost exclusively to the thin surface fluid "ocean" overlying the crust. These modes have periods of the order of

hundreds of milliseconds, with higher overtones having longer periods. A second subclass, the ${}_lg_n^c$ modes, is similarly confined to the superfluid core. Existing calculations for the core g-modes are not very satisfactory, as they neglect superfluid effects. It is expected that the properties of these modes will be substantially modified by superfluidity. To the extent that the existing calculations can be trusted for these modes, they appear to have periods of several tens of *seconds*, with the higher overtones again having longer periods.

Another complication of the oscillation spectra that is caused by the presence of the solid crust is the creation of several new modes. One of these, the ${}_ls_n$ modes, corresponds to that polarization of the shear waves in the crust which is orthogonal to the toroidal ${}_lt_n$ modes. Like them, the s-modes have periods of the order of a millisecond, with higher overtones having shorter periods. The remaining modes associated with the solid crust are two interfacial modes, which have been designated ${}_li_1$ and ${}_li_2$. They are confined approximately to the crust-ocean interface and to the crust-superfluid core interface, respectively. The mode periods reflect the properties of the upper and lower parts of the crust, respectively, and are a few hundred milliseconds and a few milliseconds.

Since the purpose of the present study is to illustrate the effects of the new shear modulus calculations on the different oscillation modes, rather than to conduct an exhaustive recalculation of the modes of different neutron star models, we have chosen to compute the modes of a single model. We have selected the NS05T7 model studied by McDermott *et al.* (1988) because details of the properties and the oscillation spectrum of this model are already in the literature. This neutron star model consists of a fluid core, a solid crust, and a thin surface. As

the structure of the model is based upon the relatively "soft" equation of state developed by Baym, Pethick, and Sutherland (1971), it is somewhat smaller in radius than most currently favored neutron star models. This model has a mass of 0.503 $M_\odot$, a radius $R_* = 9.839$ km, and a central temperature of 1.03×10^7 K.

Since the difference in $\mu_{\rm eff}$ between the crystalline and quenched states are no larger than the residual errors in the MC calculations (see Table B.3), we have fitted the crystalline values to the following formula:

$$\frac{\mu_{\rm eff}}{n(Ze)^2/a} = \frac{0.1194}{1 + 1.781 \times (100/\Gamma)^2} \,. \tag{B.36}$$

This expression fits the MC results within the estimated numerical errors and goes asymptoically to the correct limiting value as $\Gamma \to \infty$. We apply Eq. (B.36) to all the region of the solid crust.

With these results, we next computed the new shear moduli for the NS05T7 neutron star model. We did this by multiplying the value of c_{44} used in the previous calculations (McDermott *et al.*, 1988) by the ratio of our new Γ-dependent result to the c_{44} (Γ-*in*dependent) value. The smaller values of the new shear moduli produce correspondingly smaller values of the shear speed in the crust, and these in turn result in correspondingly longer oscillation periods for those modes that are especially sensitive to this quantity.

This can be seen directly in Table B.4, where we show the oscillation periods calculated for the global, non-radial $l = 2$ oscillation modes computed for the NS05T7 neutron star model using both the new and the old results for the shear moduli. Here, $\mu_{\rm eff}$ is the new shear modulus computed as discussed in this paper, and c_{44} is the old shear modulus.

These results can be summarized as follows.

(1) The periods of the two interfacial (i_1 and i_2) modes are increased by about 10 % compared to the previous results.

(2) The s-mode periods are increased by about 30 %.

(3) The periods of the f- and p-modes are hardly affected at all. This is as expected, because these modes are not greatly influenced by the properties of the crust.

(4) The periods of the surface g-modes also are not greatly affected. This probably is also to be expected, because the surface g-modes are primarily confined to the surface fluid "ocean" layer and so are not much influenced by crustal properties.

(5) The toroidal t-mode periods are increased by some 20 to 25 %. This also is expected, as are the results for the spheroidal s- and interfacial i-modes, as these three classes of modes are the most sensitive to the crustal properties.

TABLE B.4. Periods (millisecond) of neutron star oscillations: μ_{eff} is the present shear modulus, c_{44} is the former value used in McDermott *et al.* (1988).

${}_l[Mode]_n$	Period with μ_{eff}	Period with c_{44}
${}_2i_1$	96.48	90.62
${}_2i_2$	7.91	7.297
${}_2s_1$	3.114	2.427
${}_2s_2$	1.68	1.35
${}_2f$	0.3980	0.3980
${}_2p_1$	0.1861	0.1859
${}_2p_2$	0.1592	0.158
${}_2g_1^s$	236.75	232.4
${}_2g_2^s$	368.9	368.4
${}_2t_0$	22.99	18.59
${}_2t_1$	2.32	1.88
${}_2t_2$	1.355	1.096

Part C: EQUATION OF STATE AND PHASE DIAGRAM OF DENSE CARBON-OXYGEN MIXTURES

I. Introduction

Binary-ionic mixtures (BIMs) of carbon (C) and oxygen (O) are thought to constitute the internal composition of the white dwarf produced by helium burning; such a white dwarf in a close binary system may make a likely progenitor of a Type-I supernova (SNI) (Starrfield *et al.*, 1972; Whelen and Iben, 1973; Canal and Schatzman, 1976). It has been noted (Kirzhnitz, 1960; Abrikosov, 1960; Salpeter, 1961) that a dense matter in the interior of a white dwarf may undergo a freezing transition as its density and/or inverse temperature increase through the evolutionary processes.

An outstanding problem associated with such a solidification is the phase diagram or a possibility of chemical separation in the BIM material. Stevenson (1980) showed how sensitive the phase diagram of C-O mixtures was to the assumptions of thermodynamic models, and in particular pointed out a possibility of a *eutectic* phase diagram when the random-alloy mixing (RAM) model was assumed for the internal energies in the solid phase. This prediction of a eutectic was then followed by proposal of new models for white-dwarf cooling, luminosity, and SNI mechanisms involving chemical separation (Canal, Isern, and Labay, 1982; Mochkovitch, 1983).

The purpose of Part C of the Thesis is to present the detailed study on the C-O BIM phase diagrams by MC simulations and analytic calculations (Ichimaru,

Iyetomi, and Ogata, 1988; Iyetomi, Ogata, and Ichimaru, 1989). In Sec. C.II, we show in particular through the MC analyses that the internal energies of BIM solids and liquids both obey accurately the linear mixing (LM) formulas, rather than the RAM formula, invalidating thus the basic assumption introduced by Stevenson (1980) for his eutectic diagram. We then carry out nonlinear density-functional calculations of the BIM solids, to derive an analytic expression for mixing entropy; for liquids, we take the ideal entropy of mixing. Those evaluations of internal energies and entropies lead to a novel prediction of an *azeotropic* phase diagram for the C-O BIM material in Sec. C.III; consequently, a chemical separation is unlikely to take place in the solidification processes. Mindful of an application to evolution calculations, we evaluate numerically the mass-density differences on the phase boundaries in Sec. C.IV.

II. Thermodynamic functions

We consider a C-O BIM with $x = n_O/n$ (the molar fraction of oxygen), where $n = n_C + n_O$ is the total number density of ions. The mass densities are assumed in the range $10^6 \leq \rho_m \leq 10^{10}$ g/cm^3, so that for the electronic pressure, $10^{10} \leq P_e \leq 10^{16}$ Mbar. The dimensionless density parameter of the electrons in Eq. (B.1),

$$r_s = 1.75\rho_m^{-1/3} , \tag{C.1}$$

ranges in $10^{-3} \leq r_s \leq 10^{-2}$; hence, the electrons form a relativistically degenerate, incompressible background of negative charges (see Sec. B.II), except across the phase boundaries, where $\Delta\rho_m/\rho_m < 10^{-3}$ (cf. Sec. C.IV). The freezing temperature of carbon plasmas (Ogata and Ichimaru, 1987),

$$T_C = 3.48 \times 10^4 r_s^{-1}(\mathrm{K}) , \tag{C.2}$$

are found in $2 \times 10^6 \leq T_C \leq 5 \times 10^7$ K.

The effective Coulomb coupling constant of the BIM is formulated as (Ichimaru, Iyetomi, and Tanaka, 1987)

$$\Gamma_{\rm eff} = \langle Z^{5/3} \rangle \Gamma_e \ , \tag{C.3}$$

where $\langle Z^p \rangle = Z_1^p(1-x) + Z_2^p x$, and

$$\Gamma_e = 5.0476 \times 10^{-2} \Gamma_{\rm m} T_C / T \ . \tag{C.4}$$

We take $Z_1 = 6$ and $Z_2 = 8$ for the C-O BIM and $\Gamma_{\rm m} = 180$ for a transition to a *bcc* crystal in the classical OCP (Ogata and Ichimaru, 1987).

(a) MC simulation study

We have performed a series of MC simulations with $N = 1024$, the number of MC particles, for the fluid and crystalline BIMs at various combinations of T and x, following the standard Metropolis algorithm (Brush *et al.*, 1966). In the simulations, we have implemented a possibility of interchanging two neighboring MC particles, in addition to the usual random displacements of particle positions. We started from a randomly distributed configuration of particles in the fluid simulations. For the crystalline simulations, we adopted the *bcc*-lattice positions as the initial configuration of all the particles. In each run, we have generated $\sim 10^7$ MC configurations after the system reached equilibrium.

In the *bcc* lattice simulations, irrespective of the initial distribution of O ions on the lattice sites, we have found the equilibrated final states to take random *bcc*-solid configurations. Figures C.1(a)–(d) show the resulting partial distribution functions, $g_{\mu\nu}(r)$ with μ, ν =C, O, for lattice simulations at $(T/T_C, x) = (0.5, 0.5)$,

(0.9, 0.5), (1.1, 0.61), and for fluid simulation at $(T/T_C, x) = (1.1, 0.48)$. Both in the fluid and *bcc* crystalline simulations, the ratio of the first-peak position in $g_{\rm OO}(r)$ to that in $g_{\rm CC}(r)$ is approximately $(Z_{\rm O}/Z_{\rm C})^{1/3} \simeq 1.1$. Such a behavior may be related to the fact that the ion-sphere (i.e., Wigner-Seitz) radius for an ion with charge Ze is proportional to $Z^{1/3}$. In the *bcc* crystalline cases, peak positions of $g_{\mu\nu}(r)$ other than the first peaks coincide with each other between C-C, C-O, and O-O pairs; it is a result of existence of the long-ranged *bcc* lattice order. Especially for the crystalline simulations at $(T/T_C, x) = (0.5, 0.5)$ and (0.9, 0.5) shown in Figs. C.1(a) and C.1(b), we find that the first peak of $g_{\mu\nu}(r)$ is higher for C-O pair than for C-C and O-O pairs. This finding indicates that the system do not favor chemically separated state in the *bcc*-solid phase.

With the knowledge of $g_{\mu\nu}(r)$ the (normalized) excess internal-energy, $u = U_{\rm ex}/Nk_{\rm B}T$, is calculated as (Ichimaru, Iyetomi, and Tanaka, 1987)

$$u = \sum_{\mu\nu} \frac{\sqrt{n_\mu n_\nu}}{2k_{\rm B}T} \int d\vec{r} \frac{Z_\mu Z_\nu e^2}{r} [g_{\mu\nu}(r) - 1] \ . \tag{C.5}$$

The MC values of u are listed in Table C.1 for the fluid and in Table C.2 for the random *bcc*-solid simulations.

In terms of the OCP excess internal-energy formula, $u_{\rm OCP}(\Gamma)$, the ion-sphere model considerations (Salpeter, 1954; Ichimaru, 1982) predict the LM formula:

$$u_{\rm LM} = (1-x) u_{\rm OCP}(Z_1^{5/3}\Gamma_e) + x u_{\rm OCP}(Z_2^{5/3}\Gamma_e) \ . \tag{C.6}$$

The RAM model assumes that the internal energy of a BIM may be given by that of an equivalent OCP with $Z = \langle Z \rangle$, so that

$$u_{\rm RAM} = u_{\rm OCP}(\langle Z \rangle^{5/3}\Gamma_e) \ . \tag{C.7}$$

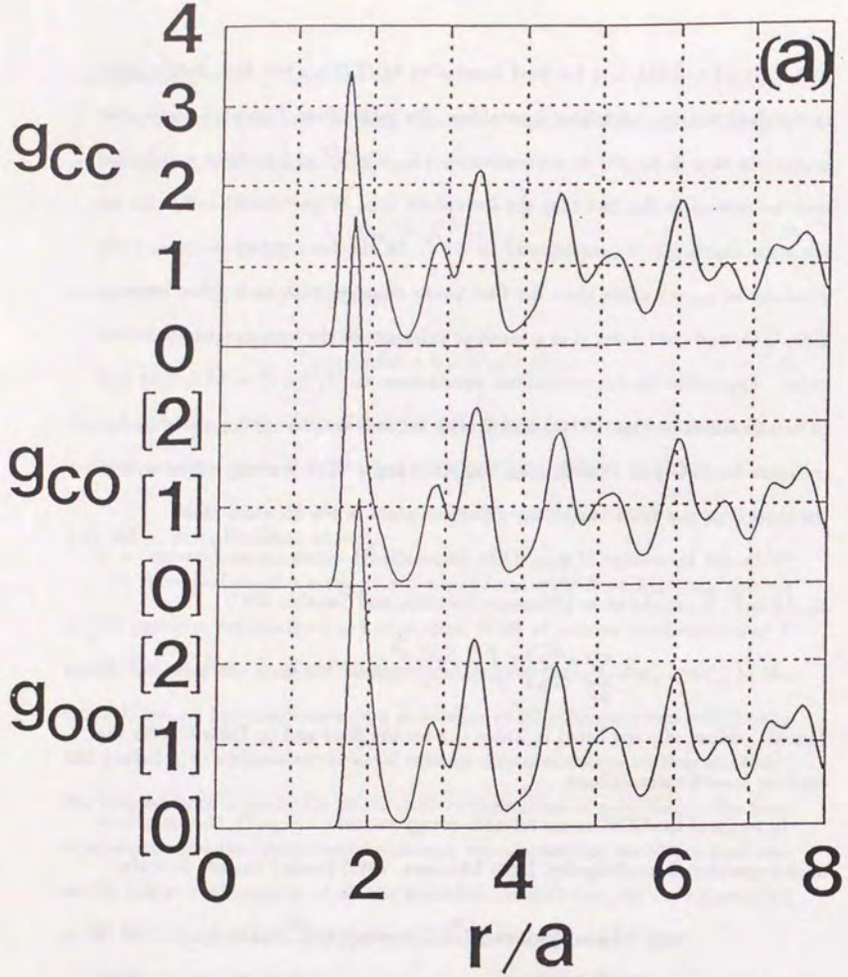

Fig. C.1(a) Partial radial-distribution functions vs. distance in units of $a = (3/4\pi n)^{1/3}$, the average interionic separation, for the lattice simulation at $T/T_C = 0.5$ and $x = 0.5$.

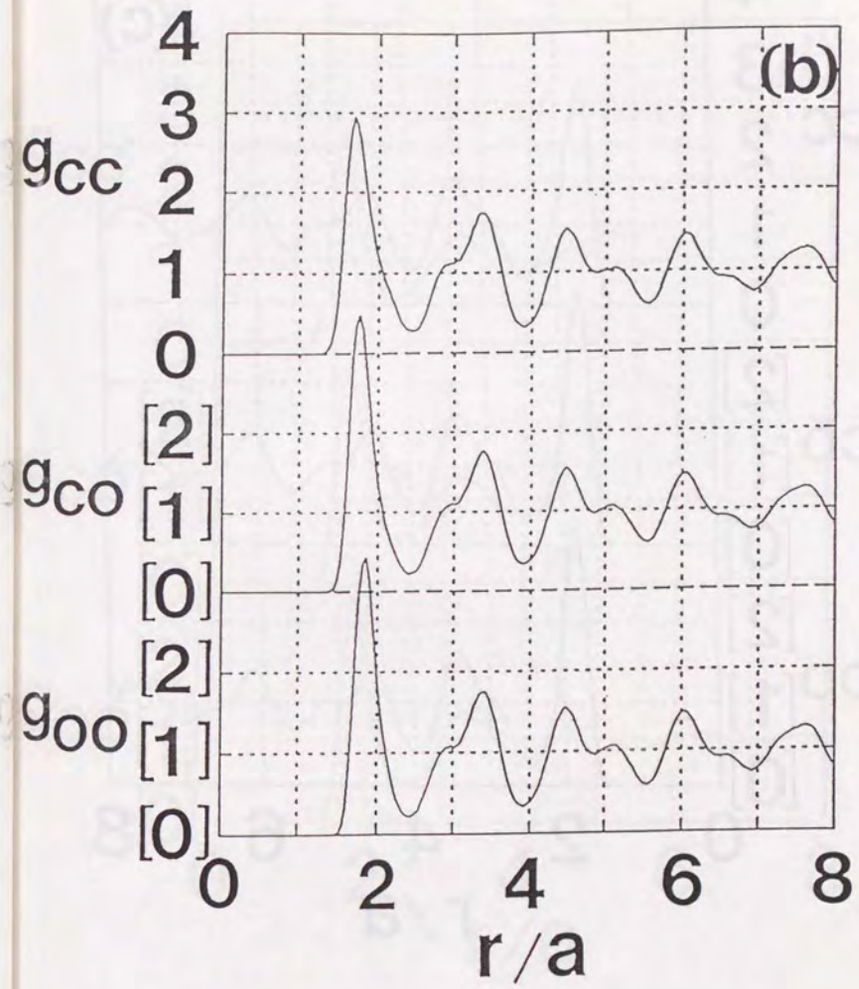

Fig. C.1(b) Partial radial-distribution functions vs. distance in units of $a = (3/4\pi n)^{1/3}$, the average interionic separation, for the lattice simulation at $T/T_C = 0.9$ and $x = 0.5$.

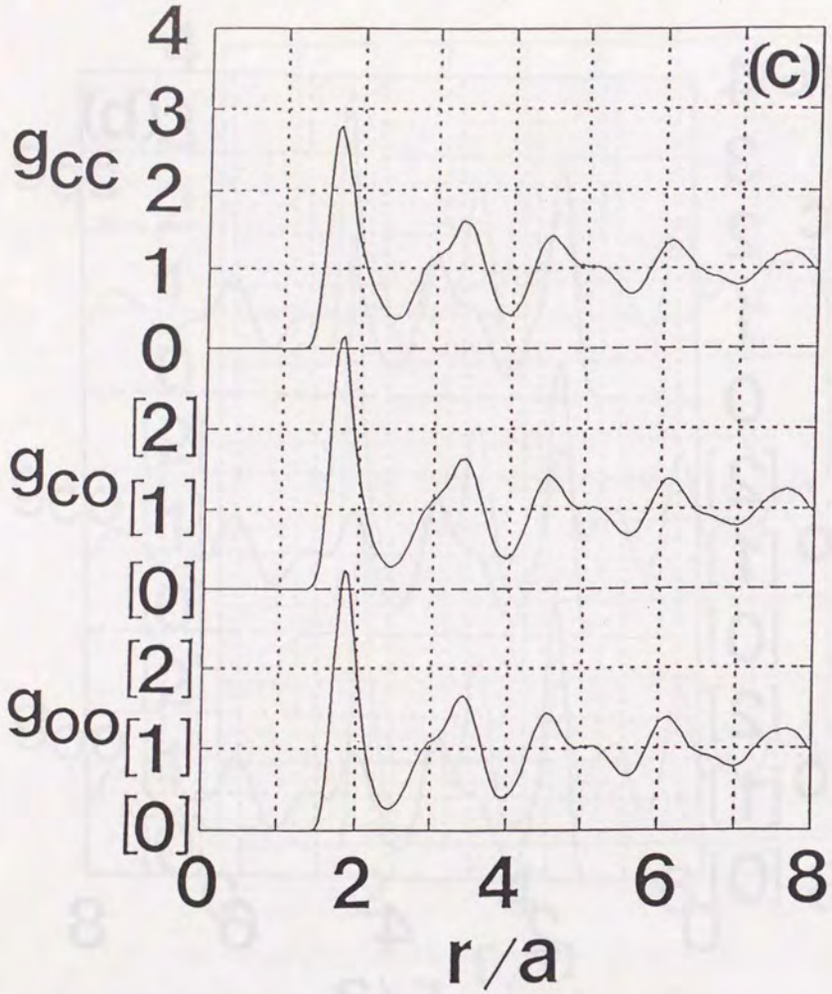

Fig. C.1(c) Partial radial-distribution functions vs. distance in units of $a = (3/4\pi n)^{1/3}$, the average interionic separation, for the lattice simulation at $T/T_C = 1.1$ and $x = 0.61$.

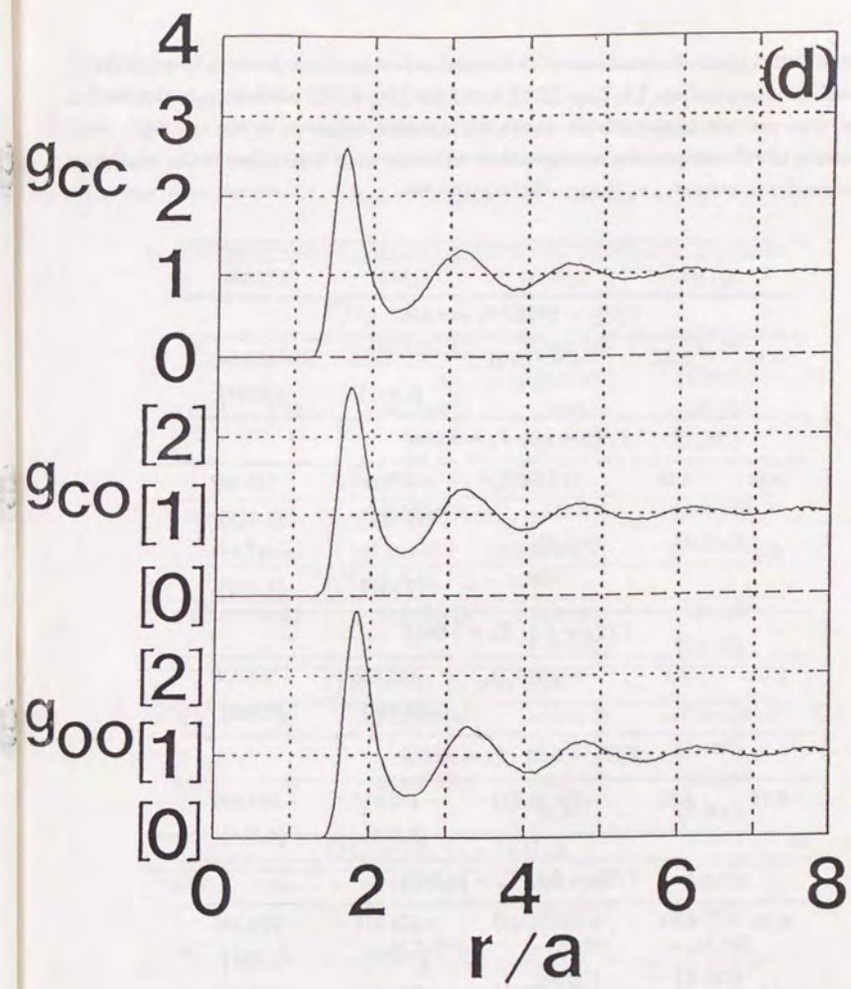

Fig. C.1(d) Partial radial-distribution functions vs. distance in units of $a = (3/4\pi n)^{1/3}$, the average interionic separation, for the fluid simulation at $T/T_C = 1.1$ and $x = 0.48$.

TABLE C.1. Numerical comparison of the normalized excess internal-energy between the MC values, u_{MC}, and the LM [Eq. (C.6)] and RAM [Eq. (C.7)] predictions in the *fluid* state. The numbers in parentheses denote the standard deviations in the last digits of the means in 10^5 configuration averages; the numbers in curly braces denote the relative discrepancies in percent, i.e., $[(u_{\mathrm{MC}} - u)/u_{\mathrm{MC}}] \times 100$.

x	$\langle Z \rangle$	u_{MC}	u_{LM}	u_{RAM}
		$T/T_{\mathrm{C}} = 1.128,\ \Gamma_e = 8.0547$		
0.16	6.32	−154.712(3)	−154.695	−153.548
			{0.011}	{0.751}
		$T/T_{\mathrm{C}} = 1.1,\ \Gamma_e = 8.2596$		
0.48	6.96	−187.863(5)	−187.469	−185.307
			{0.210}	{1.361}
0.5	7	−189.551(6)	−189.269	−187.104
			{0.149}	{1.291}
		$T/T_{\mathrm{C}} = 1.0,\ \Gamma_e = 9.0857$		
0.05	6.1	−163.938(3)	−163.848	−163.389
			{0.055}	{0.328}
		$T/T_{\mathrm{C}} = 0.94,\ \Gamma_e = 9.6656$		
0.16	6.32	−186.042(3)	−186.015	−184.639
			{0.015}	{0.754}
		$T/T_{\mathrm{C}} = 0.9,\ \Gamma_e = 10.0951$		
0.42	6.84	−223.313(5)	−222.979	−220.396
			{0.150}	{1.306}
0.5	7	−232.171(6)	−232.782	−229.138
			{0.168}	{1.306}

TABLE C.2. Numerical comparison of the normalized excess internal-energy between the MC values, u_{MC}, and the LM [Eq. (C.6)] and RAM [Eq. (C.7)] predictions in the *solid* state. The numbers in parentheses denote the standard deviations in the last degits of the means in 10^5 configuration averages; the numbers in curly braces denote the relative discrepancies in percent, i.e., $[(u_{\mathrm{MC}} - u)/u_{\mathrm{MC}}] \times 100$.

x	$\langle Z \rangle$	u_{MC}	u_{LM}	u_{RAM}
		$T/T_{\mathrm{C}} = 1.1,\ \Gamma_e = 8.2596$		
0.5	7	−190.241(5)	−190.120	−187.981
			{0.064}	{1.188}
0.61	7.22	−200.436(4)	−200.050	−198.021
			{0.193}	{1.205}
		$T/T_{\mathrm{C}} = 1.0,\ \Gamma_e = 9.0857$		
0.05	6.1	−164.675(3)	−164.633	−164.179
			{0.026}	{0.298}
		$T/T_{\mathrm{C}} = 0.94,\ \Gamma_e = 9.6656$		
0.16	6.32	−186.768(3)	−186.871	−185.508
			{−0.055}	{0.668}
		$T/T_{\mathrm{C}} = 0.9,\ \Gamma_e = 10.0951$		
0.5	7	−232.899(4)	−232.749	−230.128
			{0.064}	{1.190}
0.77	7.54	−263.495(4)	−262.527	−260.685
			{0.367}	{1.066}
		$T/T_{\mathrm{C}} = 0.5,\ \Gamma_e = 18.1712$		
0.05	6.1	−330.994(3)	−330.935	−330.023
			{0.003}	{0.282}
0.5	7	−420.581(4)	−420.231	−415.502
			{0.083}	{1.208}
		$T/T_{\mathrm{C}} = 0.47,\ \Gamma_e = 19.3312$		
0.16	6.32	−375.213(3)	−375.380	−372.645
			{−0.045}	{0.684}

The OCP excess internal-energy formulas are

$$u_{\rm OCP}(\Gamma) = -0.895929\Gamma + 1.5 + 3225/\Gamma^2 \qquad \text{(C.8)}$$

for the *bcc* crystalline state (Slattery, Doolen, and DeWitt, 1982) and

$$u_{\rm OCP}(\Gamma) = -0.898004\Gamma + 0.96786\Gamma^{1/4} + 0.220703\Gamma^{-1/4} - 0.86097 \qquad \text{(C.9)}$$

for the fluid state (Ogata and Ichimaru, 1987).

In Tables C.1 anc C.2, we have compared the excess internal-energy values predicted by the mixing formulas (C.6) and (C.7) with the MC values. We have thus observed that the LM formula (C.6) can reproduce the MC values very accurately both in the fluid and solid states, while the RAM formula (C.7) is not accurate enough to be used in the phase-diagram calculations.

Separately, Iyetomi, Ogata, and Ichimaru (1988) examined the validity of the LM formula (C.6) analytically for the C-O BIM fluids, through numerical solution to the hypernetted chain (HNC) and the improved HNC (IHNC) schemes (Iyetomi and Ichimaru, 1982, 1983b). The results have likewise shown the superiority of formula (C.6) in the HNC and IHNC schemes. We conclude that the internal energies of the C-O BIM fluids and solids can be evaluated through formula (C.6)

(b) Entropy of mixing

Iyetomi and Ichimaru (1988) formulated a variational approach to the free energy for the OCP solids in the nonlinear density-functional method. Iyetomi, Ogata, and Ichimaru (1989) subsequently treated the free energy $F(x)$ of the BIM solids, using an increased number of the variational parameters. The mixing

entropy, $\Delta S_{\rm c}$ of the crystalline state is then calculated as the variational minimum of

$$-T\Delta S_{\rm c} \equiv F(x) - [(1-x)F(x=0) + xF(x=1)] \; . \qquad \text{(C.10)}$$

In Fig. C.2, we plot the values of $\Delta S_{\rm c}$ so computed at $\Gamma_e = 7$ and $\Gamma_e = 13$. We thus find that the calculated values can be parametrized accurately by the formula:

$$\Delta S_{\rm c}(\Gamma_e, x) = R(\Gamma_e)\Delta S_{\rm id}(x) \; . \qquad \text{(C.11)}$$

where $R(\Gamma_e) = 0.7204 - 0.0354(\Gamma_e - 10) + 0.0016(\Gamma_e - 10)^2$ near the solidification temperatures, and

$$\Delta S_{\rm id}(x) = -Nk_{\rm B}[(1-x)\ln(1-x) + x\ln x] \; . \qquad \text{(C.12)}$$

The calculated values of (C.11) and (C.12) are plotted in Fig. C.2, to show the accuracy of fitting formula (C.11).

The entropy of mixing in the fluid phase is calculated as

$$\Delta S_{\rm F}(x) = \Delta S_{\rm id}(x) - Nk_{\rm B}[(1-x)\ln(Z_1/\langle Z\rangle) + x\ln(Z_2/\langle Z\rangle)] \; . \qquad \text{(C.13)}$$

The second term of formula (C.13) stems from the charge neutrality condition in the uniform background of the electrons (Iyetomi and Ichimaru, 1986); at $x = 0.5$, it amounts to a 1.5% correction to the first term.

III. Phase diagram

The evaluation of the thermodynamic quantities described in the preceding section can be combined into a construction of the phase diagram for the C-O BIMs. The result is shown in Fig. C.3 and implies an azeotropic phase diagram with the azeotropic point at $T_{\rm A} = 0.94T_{\rm C}$ and $x_{\rm A} = 0.16$.

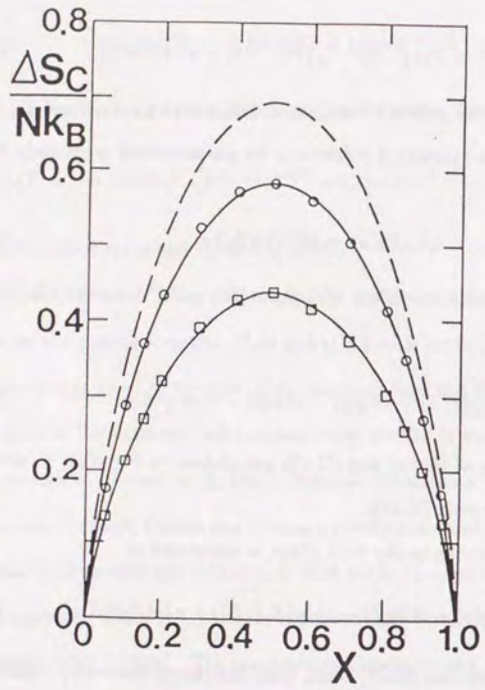

Fig. C.2 The mixing entropies computed as minima of (C.10) are plotted vs. x: open circles, $\Gamma_e = 7$; open squares, $\Gamma_e = 13$. The solid curves depict (C.11) at the same Γ_e.

The appearance of an azeotrope stems physically from the LM rule (C.6) and the mixing entropy (C.11) in solid. Since $\Delta S_{\rm C} < \Delta S_{\rm F}$ and formula (C.6) is applicable for both fluids and solids, the fluid phase is favored in the mixtures, resulting in lowering of the solidification temperatures. The solid state, still retaining a considerable amount of the mixing entropy (C.11), can sustain a mixed alloy phase, rather than chemically separated phases.

Stevenson's eutectic is a result of assuming the RAM rule (C.7) for solids (while assuming the LM rule (C.6) for liquids) and adopting the ideal entropy of mixing (C.12) for both fluids and solids. Near the solidification temperatures, the internal energy is overwhelmingly the major constituent of the free energy than the entropy term. Since formula (C.7) substantially underestimates the magnitude of the BIM internal energy as Table C.2 illustrates, the solidification temperatures decrease, and chemically separated phases are favored over mixed alloys in solids. As we have presently shown, however, the assumption of formula (C.7) cannot be justified for the C-O BIM.

IV. Variations of mass density across the phase boundary

Variation of the mass density across the phase-boundary curves can be evaluated through a perturbative method (Mochkovitch, 1983). In the ranges of physical parameters under present investigation, the partial pressure P_e of the electrons constitute the bulk of the total pressure P of the system. The ionic contribution $P_{\rm i}$ then creates a difference in mass density between the coexisting solid-solution and fluid-mixture phases across the boundary.

In the first-order perturbation theory, the discontinuity,

$$\Delta\rho_{\rm m} \equiv \rho_{\rm m}({\rm solid}) - \rho_{\rm m}({\rm fluid})\ , \qquad \text{(C.14)}$$

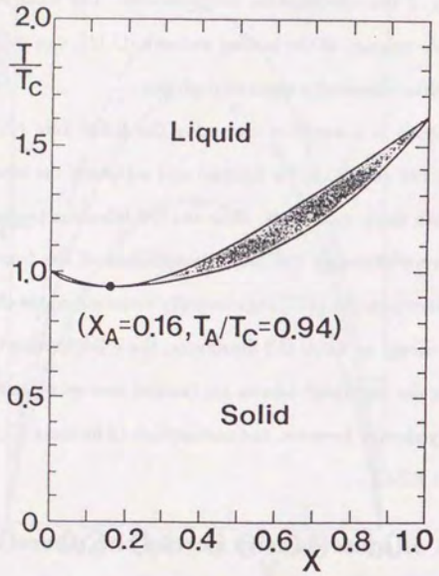

Fig. C.3 Azeotropic phase diagram of C-O mixtures.

across the phase boundary is calculated as

$$\Delta\rho_{\rm m}/\rho_{\rm m} = \Delta n_e/n_e - \Delta Y/Y$$
$$= -\Delta P_{\rm i}/\gamma P_e - \Delta Y/Y \ . \qquad \text{(C.15)}$$

Here $Y = \langle Z\rangle/\langle A\rangle$ refers to the number of electrons per unit of atomic mass, and $\gamma \equiv (d\ln P_e/d\ln\rho_{\rm m})_Y$ is an adiabatic index.

The results for the azeotropic phase diagram of Fig. C.3 are listed in Table C.3. In the case of Stevenson's eutectic diagram, the discontinuities have been calculated (Mochkovitch, 1983) to fall in the range of $(1\text{–}2)\times10^{-3}$ at the eutectic point. Hence, the present results at the azeotropic point are smaller by about an order of magnitude than those at Stevenson's eutectic point, predicting significantly reduced influences of the phase separation on the evolution of a C-O white dwarf.

TABLE C.3. Discontinuities, $\Delta\rho_{\rm m} \equiv \rho_{\rm m}(\text{solid}) - \rho_{\rm m}(\text{fluid})$, between the coexisting solid solution and fluid mixture phases as a function of pressure P at $x = 0.5$ (initial fluid composition) and at the azeotrope, $x = x_{\rm A}$.

P (Mbar)	$\Delta\rho_{\rm m}/\rho_{\rm m}$ (10^{-3})	
	$x = 0.5$	$x = x_{\rm A}$
2×10^{10}	0.57	0.11
2×10^{11}	0.43	0.084
2×10^{12}	0.37	0.072
2×10^{13}	0.34	0.068
2×10^{14}	0.33	0.066
2×10^{15}	0.33	0.066
2×10^{16}	0.33	0.066

Part D: NUCLEAR REACTION RATES IN DENSE BINARY-IONIC MIXTURES

I. Introduction

Nuclear reaction rates in dense C-O BIMs are essential quantities governing the evolution and ignition in white-dwarf progenitors of Type-I supernovae (Barkat, Wheeler, and Buchler, 1972; Graboske, 1973; Couch and Arnett, 1975). Phase diagrams associated with freezing transitions in such BIMs have been elucidated in Part C. The short-range correlations responsible for nuclear reactions in dense matter are influenced strongly by such phase properties as well as by the quantum and classical many-body effects.

Enhancement of thermonuclear reaction rates arising from Coulomb correlations in dense OCPs was reviewed by Ichimaru (1982). Jancovici (1977) developed a quantum-statistical framework for a treatment of short-range correlations between the reacting pairs; Alastuey and Jancovici (1978) applied this theory for a calculation of the enhancement factor with the aid of a screening potential obtained in the classical statistics. Their calculations therefore superseded in the principles those of Itoh, Totsuji, and Ichimaru (1978), who relied on an approximate evaluation of the WKB penetration probability with the classical potential of mean force. Analogous criticism is applicable likewise to an extension of the latter work in the BIM cases by Itoh *et al.* (1979).

In all the theories cited above, the quantities that essentially control the enhancement rates are the short-range screening potentials defined as the balances between the bare Coulomb potentials and the potentials of mean force. Accuracy

of the short-range screening potentials derived from computer simulations and otherwise at that time, however, did not exactly match with the necessary level for the problem; this was especially the case with BIMs. Since then, owing to advancement of computer capabilities, one can now treat the short-range correlations with substantially improved accuracy both for OCPs (e.g., Ichimaru and Ogata, 1990) and for BIMs (Ichimaru, Iyetomi, and Ogata, 1988).

In Part D, we thus present the first-principles calculations of nuclear reaction rates in dense C-O BIMs in the fluid phase (*thermonuclear reaction*) as well as in the *bcc* crystalline phase (*pycnonuclear reaction*) (Ogata, Iyetomi, and Ichimaru, 1991). In so doing, we extend the quantum-statistical treatment, developed originally by Jancovici (1977) for OCP, to the BIM situations. First, we evaluate accurately the short- and intermediate-range correlations in the BIMs for both fluid and *bcc* crystalline phases by the MC simulation method in Sec. D.II. In Secs. D.III and D.IV, we then treat correctly the contact probabilities by an exact solution to the resultant Schrödinger equations for both phases. As a result, we discover "blocking" effect of "larger" O nuclei against pycnonuclear reactions of "smaller" C nuclei.

In those calculations for both fluid and crystalline phases, we have neglected screening effects of degenerate electrons on the ground that the dielectric screening function of the electrons would take on values close to unity for those dense materials. At high densities of interest, i.e., $r_s \leq 0.01$, however, the relativistic effects may act to enhance the screening by "softening" the electrons against compression (cf. Sec. B.II). In Sec. D.V, we evaluate quantitatively the possible enhancement due to screening effects of electrons in the fluid phase (Ogata and

Ichimaru, 1991). Finally in Sec. D.VI, carbon ignition curves are obtained through balance between C-C reactions and neutrino losses to illustrate the effects of the calculated enhancement factors to the evolution of white dwarfs. Concluding remarks are given in Sec. D.VII.

II. MC screening potentials

The Coulomb coupling parameters (e.g., Ichimaru, 1982) for C-O BIMs with mass density ρ_m at temperature T are

$$\Gamma_{ij} = \frac{Z_i Z_j e^2}{a_{ij} k_B T} , \tag{D.1}$$

where $a_{ij} = \frac{1}{2}(a_i + a_j)$ $(i, j = \mathrm{C}, \mathrm{O})$, $a_i = Z_i^{1/3} a_e$, $\langle Z \rangle = (1-x)Z_C + xZ_O$, $a_e = (3/4\pi\langle Z \rangle n)^{1/3}$ is the Wigner-Seitz radius of the electrons, x is the molar fraction of oxygen, and n is the total number density of ions. Though we formulate the theory mostly in terms of the BIM, the OCP limit may be approached in the obvious way and will be hereafter described with omission of the subscripts.

The screening potentials, $H_{ij}(r)$, are defined in conjunction with the joint probability densities, $g_{ij}(r)$, as

$$\beta H_{ij}(r) = \Gamma_{ij} \frac{a_{ij}}{r} + \ln[g_{ij}(r)] . \tag{D.2}$$

In the intermediate range of r, the screening potentials can be sampled by the MC method (e.g., Ichimaru, 1982). For the C-O BIM, we have performed sixteen cases of fluid and crystalline simulations with $N = 1024$ as explained in Part C; in each simulation, 10^7 MC configurations have been generated.

To probe further into the short-range character of the screening potentials, we have carried out "extra-long" OCP-fluid simulations with $N = 432$. The numbers

of MC configurations generated were 2.5×10^8 at $\Gamma = 10$, 0.7×10^8 at $\Gamma = 40$, and 1.0×10^8 at $\Gamma = 160$; these numbers are to be compared with several times 10^6 configurations in some of the existing simulations (Slattery *et al.*, 1982; Ogata and Ichimaru, 1987). As Figs. D.1(a) and 1(b) illustrate, we have thus been able to sample the screening potentials accurately over an extended domain of r/a. The MC results in Fig. D.1(a) exhibit significant departures from the linear behavior (DeWitt, Graboske, and Cooper, 1973; Itoh, Totsuji, and Ichimaru, 1978) towards both ends. Comparison between Fig. D.1(a) at $\Gamma = 10$ and Fig. D.1(b) at $\Gamma = 160$ indicates a slight dependence of the slope on Γ.

In the vicinity of $r = 0$, the screening potentials are expanded (Widom, 1963) in powers of $(r/a_{ij})^2$, such that

$$\beta H_{ij}(r) = h_0 - h_1 \left(\frac{r}{a_{ij}}\right)^2 + h_2 \left(\frac{r}{a_{ij}}\right)^4 + \cdots . \tag{D.3}$$

Extending the OCP calculation of Jancovici (1977) to the BIM, we find that

$$h_1 = \frac{\Gamma_{ij}(Z_i^{1/3} + Z_j^{1/3})^3}{16(Z_i + Z_j)} . \tag{D.4}$$

The coefficient h_2 is related to a mean square value of the microscopic forces acting on a given particle (Widom, 1963) and can be evaluated by the MC sampling method. As described in the Appendix II, we have carried out these samplings at various Γ values, to confirm that h_2 is virtually zero, far smaller in magnitude than h_1: This finding enables us to truncate the expansion (D.3) at the second term with h_1, and thereby to establish a smooth and accurate extrapolation scheme of the MC screening potential into the short-range domain.

The screening potentials in the *bcc* crystalline phases can be analyzed analogously through the MC sampling method. Here we deal with the joint probability

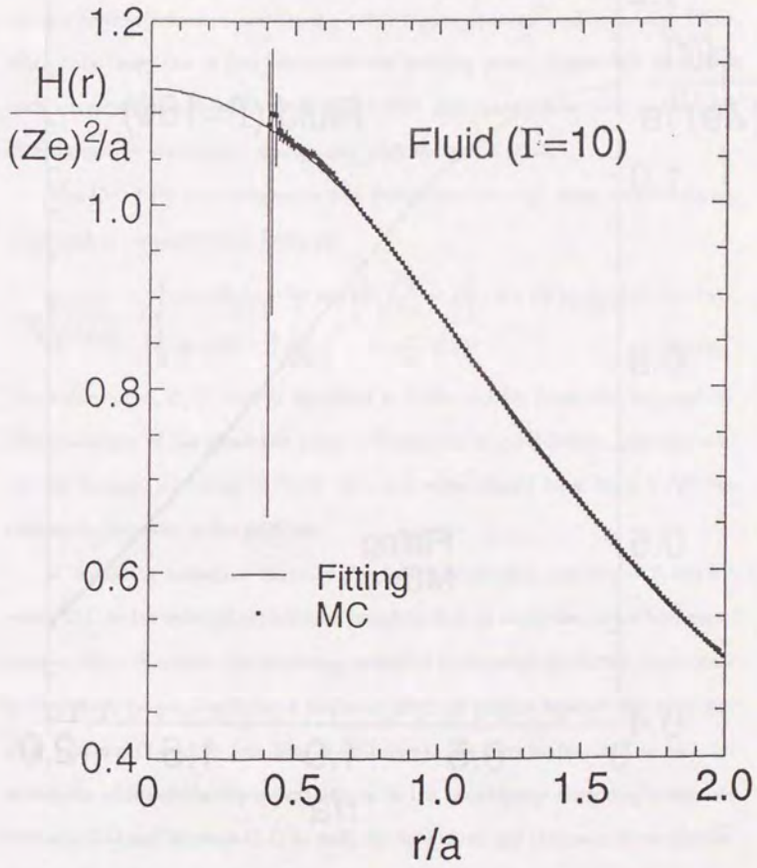

Fig. D.1(a) Screening potential for OCP fluid at $\Gamma = 10$. The maximum extent of uncertainties in the MC sampling points is 10^{-4}, unless explicitly shown by vertical bars.

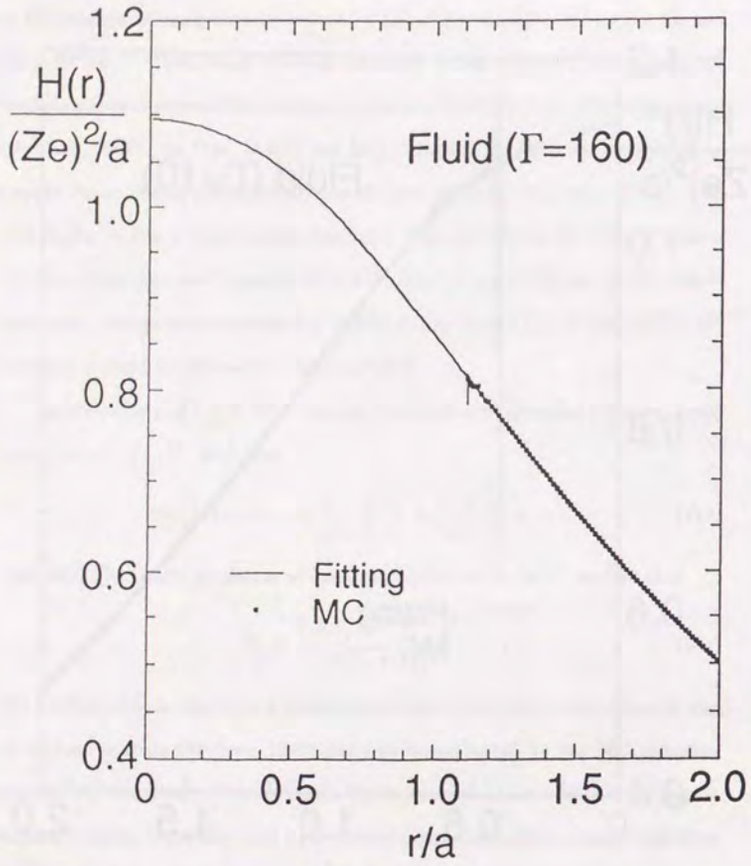

Fig. D.1(b) Screening potential for OCP fluid at $\Gamma = 160$. The maximum extent of uncertainties in the MC sampling points is 10^{-5}, unless explicitly shown by vertical bars.

densities between those pairs of particles located in the nearest neighbor sites of the *bcc* lattice (Ichimaru and Ogata, 1990; Ogata, Iyetomi, and Ichimaru, 1990), since only those can in fact constitute the reacting pairs. Figure D.2 illustrates such a screening potential for OCP at $\Gamma = 200$. Extrapolation into the short-range domain can be carried out analogously with the aid of (D.3).

The C-O BIM screening potentials determined through those procedures are expressed in parameterized forms as

$$\frac{H_{ij}(r)}{Z_i Z_j e^2/a_{ij}} = \begin{cases} A - B\frac{r}{a_{ij}} + \frac{a_{ij}}{r}\exp\left[C\sqrt{\frac{r}{a_{ij}}} - D\right], & \text{for } 2B \le \frac{r}{a_{ij}} < 2, \quad \text{(D.5a)} \\ A - B^2 - \frac{1}{4}\left(\frac{r}{a_{ij}}\right)^2, & \text{for } \frac{r}{a_{ij}} < 2B\,. \quad \text{(D.5b)} \end{cases}$$

The values of A, B, C, and D are listed in Table D.1 for fluids and *bcc* crystals. The coefficient of the quadratic term in (D.5b) for $H_{\mathrm{CO}}(r)$ is here approximated as 1/4, though according to (D.4) its exact value should have been 0.248; the difference, however, is insignificant.

It should be remarked that the short-range screening potentials (D.5b) between C-C in the solid phase are here found to depend on x, the molar fraction of oxygen. As x increases, the screening potential is therefore predicted to decrease in the short ranges, implying a blocking effect of oxygen against the pycnonuclear reaction of carbon (see Sec. D.III below). We have endeavored to look for analogous composition-dependent effects in the short-range screening potentials between C-O and between O-O as well. To the extent and accuracy of our simulation study, such a composition-dependent effect has not been seen in the screening potentials between C-O and between O-O, however. The difference between the charge numbers, $Z_{\mathrm{C}} = 6$ and $Z_{\mathrm{O}} = 8$, though small in magnitude, appears to be the source of such an asymmetry.

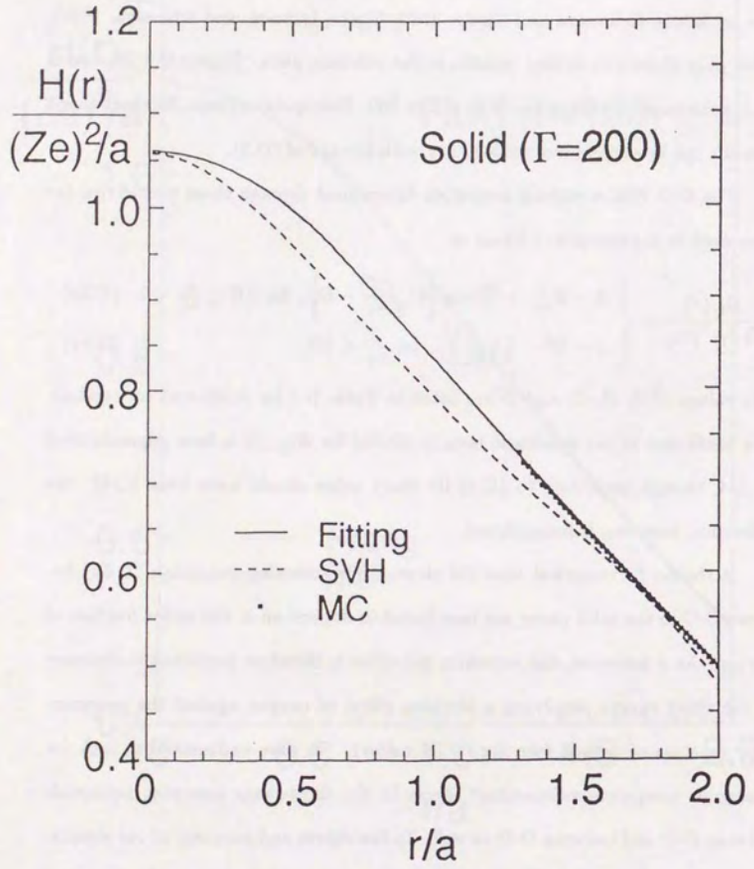

Fig. D.2 Screening potential between pairs of the first nearest-neighbor particles for OCP solid at $\Gamma = 200$. The maximum extent of uncertainties in the MC sampling points is 10^{-4}, unless explicitly shown by vertical bars.

TABLE D.1. Screening potential parameters in Eqs. (D.5a) and (D.5b).

	A	B	C	D
FLUID	1.356	0.456	9.29	14.83
	$-0.0213 \ln \Gamma_{ij}$	$-0.0130 \ln \Gamma_{ij}$	$+0.79 \ln \Gamma_{ij}$	$+1.31 \ln \Gamma_{ij}$
SOLID (C–C)	1.183	0.350	13.2	22.1
	$-0.035\sqrt{x}$	$-0.015\sqrt{x}$	$-10.2\sqrt{x}$	$-14.4\sqrt{x}$
(C–O)	1.166	0.340	13.2	22.5
(O–O)	1.183	0.350	34.0	51.3
			$-20.8\sqrt{x}$	$-29.2\sqrt{x}$

It should be likewise noted that A, B, C, and D for fluids contain dependence on $\ln \Gamma_{ij}$. These and departures from linearity in the intermediate regime ($2B \leq r/a_{ij} < 2$) are the features unknown in the earlier analyses (DeWitt, Graboske, and Cooper, 1973; Itoh, Totsuji, and Ichimaru, 1978; Itoh *et al.*, 1979) and constitute new findings in these elaborate MC analyses.

In Figs. D.1(a), D.1(b), and D.2, we compare the OCP limit of the fitting formula (D.5) to the MC results and find an excellent agreement between the two. Combining this with our proof of $h_2 \simeq 0$, we may ensure good accuracy of the short-range extrapolation of the MC screening potentials performed in (D.5b); we estimate errors in the values of $H_{ij}(0)$ so extrapolated to stay on the order of 0.1 percent.

It has been shown (Hoover and Poirer, 1962; Widom, 1963; Jancovici, 1977) that the value of $H(r)$ at $r = 0$ is equal to the increment of the chemical potential for the reacting pair before and after the nuclear reaction in the OCP. An approximate estimate of this increment in the ion-sphere model was made originally by Salpeter (1954). Later, Jancovici (1977) approached this problem under the assumption that the mixing formula for the hypernetted-chain excess free energy $F(N_1, N_2)$ of N_1 charges Ze and N_2 charges $2Ze$ for fluids, proposed by Hansen, Torrie, and Vieillefosse (1977), was applicable accurately to such an extreme case of mixture with N_1 = total number of Ze particles minus 2, and $N_2 = 1$. A critical examination of various mixing formulas has appeared only recently (Ichimaru, Iyetomi, and Ogata, 1988) for the excess internal-energy in light of accurately executed BIM simulations for fluids and solids, and in this light we find that the free-energy mixing formula used by Jancovici (1977) lacks necessary

accuracy; furthermore its applicability to the extreme situation mentioned above remains questionable. Their resultant OCP fluid values,

$$\frac{H(0)}{(Ze)^2/a} = \begin{cases} 1.057\ , & \text{(Salpeter)} \\ 1.0531 + 2.2931\Gamma^{-3/4} - (2.35 + 0.5551 \ln \Gamma)/\Gamma\ , & \text{(Jancovici)} \end{cases}$$

differ significantly from the corresponding value in this work ($5 < \Gamma \lesssim 180$),

$$\frac{H(0)}{(Ze)^2/a} = 1.148 - 0.0094 \ln \Gamma - 0.00017(\ln \Gamma)^2\ . \tag{D.6}$$

For reasons enumerated in the preceding paragraph, we are confident in the accuracy of (D.6). We might add that BIM values of $H_{ij}(0)$ in Table D.1 are totally new.

Finally in Fig. D.2, we compare the OCP lattice screening potential in (D.5) with the relaxed-lattice model potential of Salpeter and Van Horn (1969). A reasonable similarity is observed.

III. Pycnonuclear reaction rates

Nuclear reaction rates between nuclei of species, i and j, per $\sqrt{n_i n_j}$ are given generally as (e.g., Salpeter and Van Horn, 1969)

$$R_{ij} = \frac{8 S_{ij} r_{ij}^*}{(1 + \delta_{ij})\hbar} \frac{n_i n_j}{n} |\Psi_{ij}(r_{\rm N})|^2\ . \tag{D.7}$$

Here $\Psi_{ij}(r_{\rm N})$ refers to the wave function at the nuclear reaction radius $r_{\rm N}$, which being extremely small in the atomic scales shall be henceforth denoted as 0, the wave function is normalized so that

$$\int_\Omega dr 4\pi r^2 |\Psi_{ij}(r)|^2 = \Omega \frac{n}{\sqrt{n_i n_j}} \tag{D.8}$$

over a spherical volume Ω with the radius $2a_{ij}$, δ_{ij} represents Kronecker's delta, and

$$r_{ij}^{*} = \frac{\hbar^2}{2\mu_{ij} Z_i Z_j e^2} \tag{D.9}$$

are the nuclear Bohr radii with μ_{ij} denoting the reduced mass between i and j. The cross sections σ_{ij} of nuclear reactions between particles with relative kinetic energy, $E = \mu_{ij} v^2/2$, is expressed as

$$\sigma_{ij} = \frac{S_{ij}}{E} \exp(-2\pi\eta) \ , \tag{D.10}$$

where $\eta = Z_i Z_j e^2/\hbar v$. The cross-section parameters for C-O BIM are (Fowler, Caughlan, and Zimmerman, 1975): $S_{\rm CC} = 8.83 \times 10^{16}$, $S_{\rm CO} = 1.15 \times 10^{21}$, and $S_{\rm OO} = 2.31 \times 10^{27}$, in units of MeV·barn. The phase diagrams associated with freezing transitions in such a C-O BIM have been investigated (see Part C). The quantum and classical many-body effects in those various phases affect the contact probabilities $|\Psi_{ij}(0)|^2$ and thereby the reaction rates. In this Section, we consider the reaction rates in BIM solids.

When the OCP is in a fluid state ($\Gamma < 180$), $\Lambda = \hbar/a\sqrt{M k_{\rm B} T}$ in Eq. (B.3) measures the degree to which a quantum-mechanical description is necessitated in the behavior of the ion with mass M. For a crystalline OCP ($\Gamma > 180$), the ratio $Y = \hbar\omega_0/k_{\rm B}T$ in Eq. (B.5), where $\hbar\omega_0$ is the Einstein frequency in the Wigner-Seitz sphere model, measures involvement of the quantum effects (see Sec. B.II). Figures D.3 and D.4 depict the freezing condition ($\Gamma = 180$) as well as the relations, $\Lambda = 1$ and $Y = 1$, on the $\rho_{\rm m}$–T planes for the carbon and oxygen

OCPs. In both figures, we observe $\Lambda < 1$ in the fluid state and $Y > 1$ in the crystalline state.

In the consideration of nuclear reaction rates in the solid BIMs, we shall henceforth assume that the condition for pycnonuclear reactions, $Y \gg 1$, is satisfied for C and O, so that the nuclei forming quantum solids are in the ground state at their equilibrium *bcc* lattice sites. The principal problem then is the evaluation of contact probabilities, $|\Psi_{ij}(0)|^2$, for the reaction rates (D.7) in such a quantum solid.

We approach this problem by observing that the major contributions to $|\Psi_{ij}(0)|^2$ arise from the S-wave scattering acts between the reacting nuclei. The factor that crucially controls such a scattering event and the resulting contact probability is then the effective potential between the nuclei in the short-range domain, where the screening potential may be regarded as isotropic, given accurately by Eq. (D.5b), though the bulk of nuclei experience anisotropic lattice fields most of the time. Further justification for the use of such a directionally averaged potential is provided by the fact that the S-wave functions sample only the spherically symmetric part of the potential.

Introducing $U_{ij}(r)$ via

$$\Psi_{ij}(r) = \exp[U_{ij}(r)] \tag{D.11}$$

with the normalization (D.8), we find that it obeys the Schrödinger equation for the S waves,

$$\left\{ -\frac{\hbar^2}{2\mu_{ij}} \frac{d^2}{dr^2} + W_{ij}(r) - E \right\} r \exp[U_{ij}(r)] = 0 \ . \tag{D.12}$$

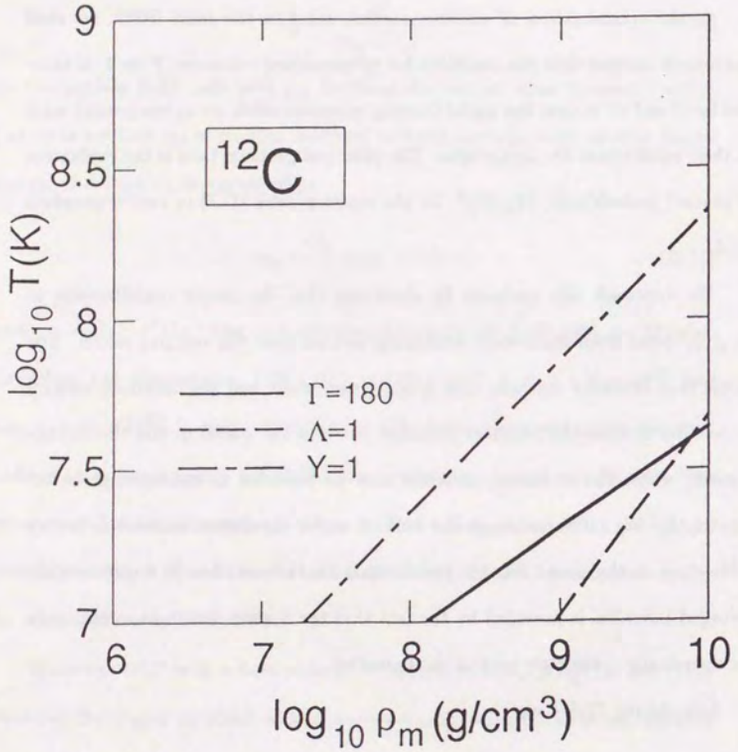

Fig. D.3 Freezing condition ($\Gamma = 180$) and comparison of the parameters Λ and Y (cf. Eqs. (B.3) and (B.5)) on ρ_m–T plane for carbon material.

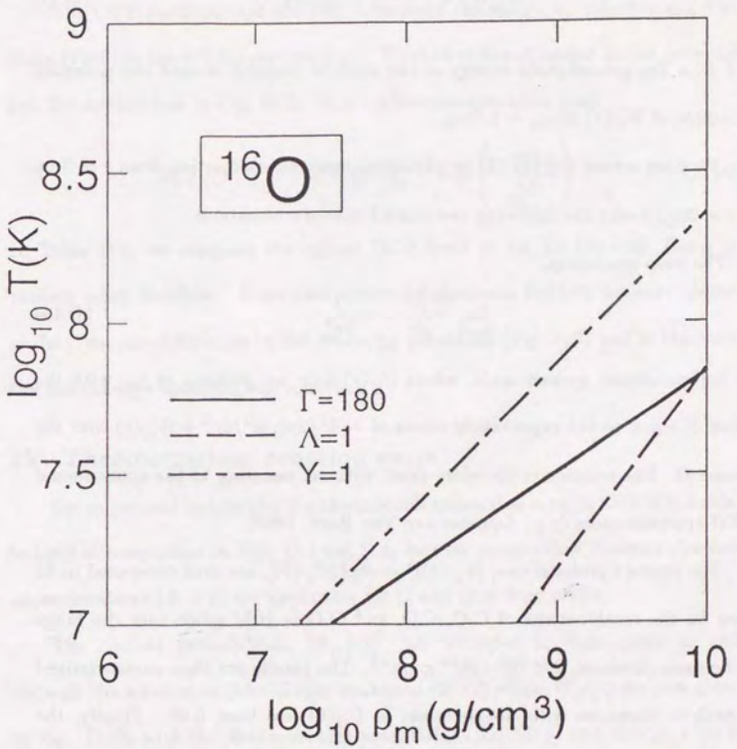

Fig. D.4 Freezing condition ($\Gamma = 180$) and comparison of the parameters Λ and Y (cf. Eqs. (B.3) and (B.5)) on ρ_m–T plane for oxygen material.

Here the effective potential of scattering is given by

$$W_{ij}(r) = \frac{Z_i Z_j e^2}{r} - H_{ij}(r) \ , \tag{D.13}$$

and E is the ground-state energy of the particle trapped around the potential minimum of $W_{ij}(r)$ at $r_{\rm m} = 1.74 a_{ij}$.

We have solved Eq. (D.12) by numerical integrations starting from $r \simeq 0$ up to $r = 2a_{ij}$, under the following two exact boundary conditions:

(1) The cusp conditions,

$$\lim_{r \to 0} \frac{dU_{ij}(r)}{dr} = \frac{1}{2r_{ij}^*} \ . \tag{D.14}$$

(2) Self-consistent ground state, where $U_{ij}(r)$ take on maxima at $r_{\rm m}$ with the values E equal to the expectation values of $-(\hbar^2/2\mu_{ij})d^2/dr^2 + W_{ij}(r)$ over the volume Ω. The solution is therefore exact without resorting to the conventional WKB approximation (e.g., Salpeter and Van Horn, 1969).

The contact probabilities, $|\Psi_{ij}(0)|^2 = \exp[2U_{ij}(0)]$, are thus computed in 45 cases for the combinations of C-C, C-O, and O-O in BIM solids over the range of the mass densities, $2 \times 10^6 - 10^{11}$ g cm^{-3}. The results are then parameterized in analytic formulae with fitting errors in $U_{ij}(0)$ less than 0.06. Finally, the pycnonuclear reaction rates in the C-O BIM solids are obtained from (D.7) as

$$R_{ij}({\rm s}^{-1}) = \frac{K \rho_8^\alpha}{1+\delta_{ij}} \exp\left(-\frac{K_1 + K_2\sqrt{x}}{\rho_8^{1/6}} - K_3 - K_4\sqrt{x} \right) \ . \tag{D.15}$$

Here ρ_8 is mass density in units of 10^8 g cm^{-3}, and the parameters, α, K, K_1, K_2, K_3, and K_4, are listed in Table D.2. The blocking effects of oxygen on the

pycnonuclear reactions, described here by the x dependence, enter through the coefficients, K_2 and K_4; these do not vanish with C-C reactions only.

The OCP pycnonuclear reaction rates were calculated by Salpeter and Van Horn (1969) in the WKB approximation. With the relaxed-lattice model potential (cf. the dashed line in Fig. D.2), their carbon-reaction rates read

$$R_{\rm SVH}({\rm s}^{-1}) = 1.11 \times 10^{38} \rho_8^{7/12} \exp\left(\frac{-263.3}{\rho_8^{1/6}} \right) \ . \tag{D.16}$$

In Table D.3, we compare the carbon OCP limit of Eq. (D.15) with $R_{\rm SVH}$ at various mass densities. Numerical agreement between the two appears almost perfect, despite differences in the screening potentials (Fig. D.2) and in the ways the Schrödinger equation was solved.

IV. Thermonuclear reaction rates

Let us proceed to consider the thermonuclear reaction rates in C-O BIM fluids. In light of comparison in Figs. D.3 and D.4, we may assume that the semi-classical approximations ($\Lambda < 1$) are applicable for C and O in fluid states.

The contact probabilities, $|\Psi_{ij}(0)|^2$, are obtained in these cases as well through the solution to Schrödinger equations (D.12) where $W_{ij}(r)$ are now given by Eq. (D.13) with the *fluid* screening potentials in Eq. (D.5) and $E = \mu_{ij} v^2/2$ is the relative kinetic energy between the reacting nuclei. The evaluations of thermonuclear reaction rates $R_{ij}(T)$ at temperature T are then carried out by the thermal averages of $R_{ij}(E)$ in Eq. (D.7) over the Boltzmann factor, that is,

$$R_{ij}(T) = \frac{2\beta^{3/2}}{\sqrt{\pi}} \int_0^\infty dE \sqrt{E} \exp(-\beta E) R_{ij}(E) \tag{D.17}$$

TABLE D.2. Parameters in Eq. (D.15) for the pycnonuclear reaction rates.

	C − C	C − O	O − O
K	$1.30 \times 10^{31} \frac{1-x}{3+x}$	$1.11 \times 10^{35} \frac{\sqrt{x(1-x)}}{3+x}$	$1.42 \times 10^{41} \frac{x}{3+x}$
α	0.397	0.421	0.455
K_1	257.486	327.132	414.706
K_2	2.636	—	—
K_3	−15.114	−15.940	−16.192
K_4	−0.560	—	—

TABLE D.3. Comparison between $R_{\rm CC}$ of Eq. (D.15) and $R_{\rm SVH}$ of Eq. (D.16).

$\log_{10} \rho_{\rm m}$ (g·cm^{-3})	$\log_{10} R_{\rm CC}$ (s^{-1})	$\log_{10} R_{\rm SVH}$ (s^{-1})
7	−127.6	−130.4
8	−74.9	−76.3
9	−38.9	−39.3
10	−14.2	−13.9

The enhancement factors, $\exp(Q_{ij})$, of the reaction rates are defined as the ratios between $R_{ij}(T)$ and $R^0_{ij}(T)$, the latter being calculated with the bare Coulomb potentials,

$$W^0_{ij}(r) = \frac{Z_i Z_j e^2}{r} , \tag{D.18}$$

substituted in place of $W_{ij}(r)$ in Eq. (D.12). Hence,

$$\exp(Q_{ij}) = R_{ij}(T)/R^0_{ij}(T) . \tag{D.19}$$

In the limit of classical approximations, one finds (e.g., Salpeter and Van Horn, 1969; DeWitt, Graboske, and Cooper, 1973)

$$Q_{ij}|_{\rm CL} = \beta H_{ij}(0) . \tag{D.20}$$

Jancovici (1977) obtained a rigorous lowest-order quantum correction to (D.20) for OCP with the short-range screening potential, $H(r) = H(0) - \pi n (Ze)^2 r^2/3$ [cf. Eq. (D.5b)]. Further quantum corrections were evaluated for OCP by Alastuey and Jancovici (1978) by the semi-classical WKB method with an approximate screening potential.

In this section we present rigorous calculations of the enhancement factors (D.19) for the BIM fluids through numerical solutions to Eq. (D.12). In doing so, we first note that with the bare potentials (D.18) the solution to Eq. (D.12) exactly gives

$$U^0_{ij}(0) = -\frac{1}{2}\ln\left\{\exp\left(\frac{\pi t}{\sqrt{\epsilon}}\right) - 1\right\} + \frac{1}{2}\ln\left(\frac{\pi t}{\sqrt{\epsilon}}\right) , \tag{D.21}$$

where

$$t = \sqrt{\frac{a_{ij}}{r^*_{ij}}} , \tag{D.22}$$

$$\epsilon = \frac{E}{Z_i Z_j e^2/a_{ij}} . \tag{D.23}$$

It then follows that with the shifted potentials,

$$W^1_{ij}(r) = \frac{Z_i Z_j e^2}{r} - H_{ij}(0) , \tag{D.24}$$

the quantities corresponding to (D.21) are

$$U^1_{ij}(0) = -\frac{1}{2}\ln\left\{\exp\left(\frac{\pi t}{\sqrt{\epsilon + h}}\right) - 1\right\} + \frac{1}{2}\ln\left(\frac{\pi t}{\sqrt{\epsilon + h}}\right) , \tag{D.25}$$

with

$$h = \frac{H_{ij}(0)}{Z_i Z_j e^2/a_{ij}} . \tag{D.26}$$

Consequently, the enhancement factors (D.19) can be re-expressed as

$$\exp(Q_{ij}) = P_{ij}(T)/P^0_{ij}(T) , \tag{D.27}$$

where

$$P_{ij}(T) = \int_0^\infty dE\sqrt{E}\exp\{-\beta E + 2U^1_{ij}(0)\}\exp(2\Delta U_{ij}) , \tag{D.28}$$

$$P^0_{ij}(T) = \int_0^\infty dE\sqrt{E}\exp\{-\beta E + 2U^0_{ij}(0)\} , \tag{D.29}$$

and

$$\Delta U_{ij} \equiv U_{ij}(0) - U^1_{ij}(0) . \tag{D.30}$$

We calculate the increments (D.30) through numerical solutions to Eq. (D.12) as follows: First, with the boundary conditions (D.14) and assuming for the moment that $U_{ij}(0) = 0$, we integrate Eq. (D.12) starting from $r = 0$; the integrated result of $U_{ij}(r)$ takes on a maximum value X near the radius r_c corresponding to the "classical turning-point." Next, we substitute $W^1_{ij}(r)$ of Eq. (D.24) in place of $W_{ij}(r)$ in Eq. (D.12), and calculate the corresponding maximum value X_1 with the resulting equation. Recalling, however, that both solutions should approach similar wave functions representing a free-particle behavior asymptotically for $r > r_c$,

we observe that the differences between X and X_1 should in fact correspond to those between $U_{ij}(0)$ and $U^1_{ij}(0)$. Hence,

$$\Delta U_{ij} = \ln(X/X_1) \ . \tag{D.31}$$

We have followed these procedures for 120 cases of the parametric combinations in the ranges: $t = 20$–200 and $\epsilon = 10^{-4}$–10^2. The results can be fitted in an analytic formula,

$$\Delta U_{ij} = -\,t\exp(-\sqrt{\epsilon+0.001})\left\{u_1 + u_2\ln\Gamma_{ij} + \frac{u_3+u_4\ln\Gamma_{ij}}{\epsilon+0.8073-0.1335\ln\Gamma_{ij}} + \frac{u_5+u_6\ln\Gamma_{ij}}{(\epsilon+0.8073-0.1335\ln\Gamma_{ij})^2}\right\} , \tag{D.32}$$

with $u_1 = 0.0011685$, $u_2 = -0.0023531$, $u_3 = 0.0020104$, $u_4 = 0.0087516$, $u_5 = 0.066453$, and $u_6 = -0.013581$. Fitting errors of Eq. (D.32) are confined within 0.3.

Finally, the results for the enhancement factors (D.27) are:

$$Q_{ij} = C_0\Gamma_{ij} - \frac{5}{32}\Gamma_{ij}\left(\frac{3\Gamma_{ij}}{\tau_{ij}}\right)^2 \times\left\{1+(C_1+C_2\ln\Gamma_{ij})\left(\frac{3\Gamma_{ij}}{\tau_{ij}}\right)+C_3\left(\frac{3\Gamma_{ij}}{\tau_{ij}}\right)^2\right\} , \tag{D.33}$$

with

$$\begin{aligned} C_0 &= 1.148 - 0.00944\ln\Gamma_{ij} - 0.000168(\ln\Gamma_{ij})^2 \ , \\ C_1 &= 1.1858 \ , \\ C_2 &= -0.2472 \ , \\ C_3 &= -0.07009 \ , \end{aligned} \tag{D.34}$$

and

$$\tau_{ij} = \left(\frac{27\pi^2}{4}\frac{Z_iZ_je^2\beta}{r^*_{ij}}\right)^{1/3} . \tag{D.35}$$

This fit is applicable for $3\Gamma_{ij}/\tau_{ij} \le 2$ with accuracy of fitting, $\delta Q_{ij} \le 1$.

The first term $C_0\Gamma_{ij}$ of Eq. (D.33) corresponds to the purely classical contribution, Eq. (D.20). Retaining the lowest-order quantum corrections in Eq. (D.33), we may derive

$$Q_{ij}|_{\rm LQ} = \beta H_{ij}(0) - \frac{5}{32}\Gamma_{ij}\left(\frac{3\Gamma_{ij}}{\tau_{ij}}\right)^2 . \tag{D.36}$$

The OCP limit of this expression coincides with that obtained by Jancovici (1977). Approximate calculations of Alastuey and Jancovici (1978) would further be recovered if substitutions: $C_1 + C_2\ln\Gamma_{ij} \to -0.0896$ and $C_3 \to -0.08192$, are made in the OCP limit of Eq. (D.33); roughly, both would agree at $\Gamma \simeq 110$ for the OCP.

V. Screening effects of relativistic degenerate electrons on the thermonuclear reaction rates

The short-range screening effects of relativistic degenerate electrons on Coulomb repulsion between the reacting nuclei were studied by Ichimaru and Utsumi (1983) with the aid of the relativistic free-electron polarizability (Jancovici, 1962) and the local-field correction of the degenerate electrons (Ichimaru and Utsumi, 1981). It has thereby been shown that the kinematic effects of relativistic degenerate electrons (e.g., Landau and Lifshitz, 1969) with inclusion of the Dirac positron states soften the electrons against compression and thus act to enhance the screening. These authors subsequently (Ichimaru and Utsumi, 1984) studied the screening effect of the electrons on the "long-range" correlation between ions over various combinations of the plasma parameters, and found that

the long-range screening potential at zero separation almost cancelled that due to the short-range correlation between ions.

In this section we revisit the calculations of the nuclear-reaction enhancement factor due to the electron screening of the short- and long-range correlations. We first present a renewed derivation of the long-range correlation effect, more transparent than that given earlier (Ichimaru and Utsumi, 1984). We then show that the short- and long-range correlations modify the nuclear reaction rates in different ways, and that the electron screening, as a consequence, brings about a considerable enhancement of nuclear reactions in high-Z materials even in the limit of high densities.

(a) Screening potentials due to dense relativistic electrons

The inter-ionic potentials, $V_{ij}^{e}(r)$, screened by the dense relativistic electrons are calculated as

$$V_{ij}^{e}(r) = \frac{Z_i Z_j e^2}{2\pi^2} \int d\vec{k} \frac{1}{k^2 \epsilon(k,0)} \exp(i\vec{k}\cdot\vec{r}) \ . \tag{D.37}$$

Here $\epsilon(k,0)$ is the static dielectric function of the relativistic degenerate electrons defined in Eq. (B.16) (we set $G(\vec{k}) = 0$ here). In the short-range domain, Eq. (D.37) may be expanded as

$$V_{ij}^{e}(r) = \frac{Z_i Z_j e^2}{r} \left(1 - \frac{r}{D_S} + \cdots\right) \ , \tag{D.38}$$

where $D_S = a_e/\alpha_0$ with

$$\alpha_0 = \left(\frac{18}{\pi^2}\right)^{1/3} \int_0^\infty dx \left[1 - \frac{1}{\epsilon(x k_{\rm F}, 0)}\right] \tag{D.39}$$

and $k_{\rm F} = (9\pi/4)^{1/3}/a_e$ is the Fermi wave number. The short-range screening parameter (D.39) has been evaluated and expressed in a parametrized form as (Ichimaru and Utsumi, 1983)

$$\alpha_0 = 0.1718 + 0.09283 R_{\rm s} + 1.591 R_{\rm s}^2 - 3.800 R_{\rm s}^3 + 3.706 R_{\rm s}^4 - 1.311 R_{\rm s}^5 \tag{D.40}$$

where $R_{\rm s} = 10 r_{\rm s}$. The formula (D.40) reproduces the computed values of (D.39) over the domain, $0 \le r_{\rm s} \le 0.1$, with digressions of less than 0.7%. A comparison between the relativistic results (D.40) and the nonrelativistic evaluations with the Lindhard (1954) polarizability was given in Ichimaru and Utsumi (1983).

It is noteworthy that the short-range screening distance (in units of a_e), $D_S/a_e = \alpha_0^{-1}$, takes on a finite value 5.8 in the limit of high densities, $r_{\rm s} \to 0$. This finiteness is a consequence of the relativistic effects. For a comparison, we note that the relativistic Thomas-Fermi distance, $(k_{\rm TF} a_e)^{-1} = (4/9\pi)^{1/3}\sqrt{\pi\hbar c/4e^2}$, takes on 5.4, a similar magnitude. The effects of the electron screening thus remain considerable in dense stellar materials (see also Sec. B.II).

In addition to the short-range, direct-screening effect between ions represented by α_0, the electron screening influences the potential of mean force (e.g., Ichimaru, 1982) through indirect, many-body effect between ions, called the long-range correlation effect (Ichimaru and Utsumi, 1984). In the Andersen-Chandler (1972) approximation, the long-range screening potential (in OCP) was calculated as

$$H^{lr}(r) = \frac{(Ze)^2}{2\pi^2} \int d\vec{k} \frac{1}{k^2} [1 - S(k)] \left[1 - \frac{1}{\epsilon(k,0)}\right] \exp(i\vec{k}\cdot\vec{r}) \ . \tag{D.41}$$

Setting the screening potential at zero separation as

$$H^{lr}(0) \equiv \beta_0 (Ze)^2/a_e \ , \tag{D.42}$$

Ichimaru and Utsumi (1984) computed and parametrized the values of $\alpha_0 - \beta_0$ over the ranges: $0 \leq r_s \leq 0.1$, $1 \leq Z \leq 26$, and $1 \leq \Gamma \leq 200$. Thus Ichimaru-Utsumi (1984) enhancement factor due to the electron screening was given by

$$A_e^{\rm IU} = \exp[(\alpha_0 - \beta_0) Z^{1/3} \Gamma] \,. \tag{D.43}$$

In Table D.4, values of those parameters are listed for $Z = 8$, 6, and 2 at various combinations of density and temperature.

In the balance of this section, we present an alternative and transparent derivation for the long-range screening parameter, β_0. In the next section, we shall perform MC sampling of the long-range screening potential for an electron-screened ion system, and thereby show that the newly derived expression for β_0 coincides closely with the MC result. Subsequently, we shall use the MC screening potential so obtained to show that short- and long-range correlations act differently in the enhancement of nuclear reactions and thereby derive a new and improved expression for A_e.

Let us thus begin with approximating Eq. (D.37) in the form of a screened Coulomb potential as

$$V_{ij}^e(r) = \frac{Z_i Z_j e^2}{r} \exp\left(-\frac{r}{D_S}\right) \,. \tag{D.44}$$

Figure D.5 depicts for a carbon material at $r_s = 10^{-3}$ the bare Coulomb potential, the equation (D.37) with the relativistic and nonrelativistic dielectric functions, and the equation (D.44). Comparison in the figure shows that Eq. (D.44) offers a good approximation to the relativistic evaluation of the exact formula (D.37).

In a separate contribution, Ichimaru *et al.* (1990) approached those long-range screening parameters for general cases of repulsive interparticle potentials,

TABLE D.4. Electron screening parameters, α_0 and β_0; and enhancement factor, A_e. IU84 refers to the results of Ichimaru and Utsumi (1984); IO90, the present work. ($Y_e = \langle Z \rangle / \langle A \rangle = 0.5$ is assumed.)

$\rho_{\rm m}$ (g/cm^3)	T (K)	Z	Γ	$\frac{3\Gamma}{\tau}$	$\frac{D_S}{a}$	α_0	β_0		A_e	
r_s							IU84	IO90	IU84	IO90
	10^8	8	72.6	0.74	2.9	0.173	0.167	0.155	2.4	15.1
2×10^9	5×10^7	8	145.2	1.18	2.9	0.173	0.168	0.155	5.1	4.24×10^4
	10^8	6	44.9	0.74	3.2	0.173	0.168	0.157	1.6	4.91
	5×10^7	6	89.9	1.18	3.2	0.173	0.169	0.157	2.2	7.51×10^2
1.4×10^{-3}	10^8	2	7.2	0.74	4.6	0.173	0.168	0.165	1.0	1.24
	5×10^7	2	14.4	1.18	4.6	0.173	0.170	0.165	1.1	2.95
	10^8	8	12.4	0.13	2.7	0.188	0.177	0.166	1.3	1.60
10^7	5×10^7	8	24.8	0.20	2.7	0.188	0.178	0.166	1.6	2.39
	10^8	6	7.7	0.13	2.9	0.188	0.176	0.168	1.2	1.26
	5×10^7	6	15.4	0.20	2.9	0.188	0.179	0.168	1.3	1.53
8.1×10^{-3}	10^8	2	1.2	0.13	4.2	0.188	0.172	0.177	1.0	1.01
	5×10^7	2	2.5	0.20	4.2	0.188	0.177	0.177	1.0	1.03

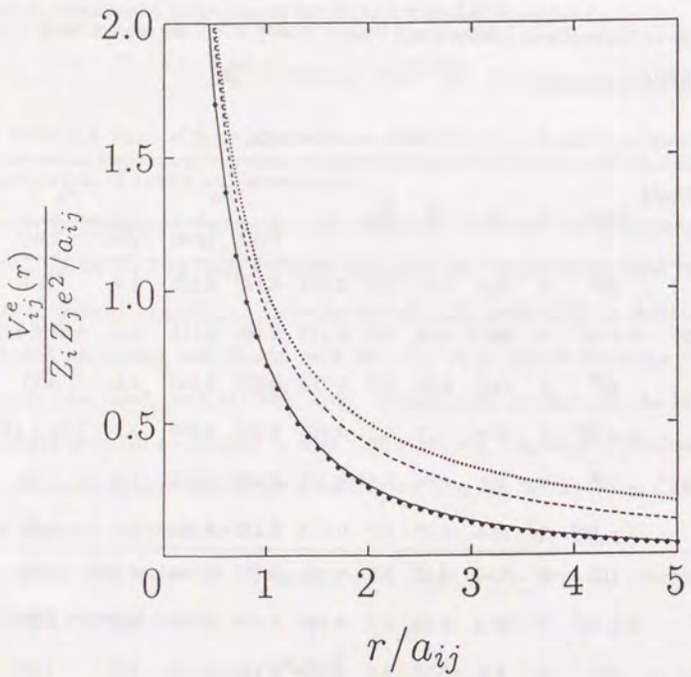

Fig. D.5 Inter-ionic potentials for a carbon matter at $r_s = 10^{-3}$. The dotted line depicts the bare Coulomb potential; the dashed line and bold dots, the non-relativistic and relativistic evaluations of Eq. (D.37); and the solid line, Eq. (D.44).

through a solution to the hypernetted-chain equations (e.g., Ichimaru, 1982) with appropriate strong-coupling corrections. For the potential (D.44), it has thus been found [cf. Eq. (18) in Ichimaru *et al.*, 1990] that

$$\beta_0 = 1.057 \frac{a_e}{a_{ij}} \left[1 - \exp\left(-\frac{a_{ij}}{D_S} \right) \right] . \tag{D.45}$$

The values (D.45) of β_0 listed in Table D.4 agree well with the Ichimaru-Utsumi (1984) values calculated from Eq. (D.42). Though both calculations involve different approximations, we find that the derivation of (D.45) is much more transparent than the earlier parametrization (Ichimaru and Utsumi, 1984). It is straightforward to reconfirm in the expressions (D.38) and (D.45) the near cancellation between the short- and long-range screening parameters, $\alpha_0 - \beta_0 \simeq 0$, for $a_{ij}/D_S < 1$.

(b) MC sampling of screening potential

To supplement the analytic calculation in the preceding section, we have performed a MC simulation study of the screening potential in a carbon matter at $\rho_m = 2 \times 10^9$ g/cm^3 and $T = 10^8$ K, assuming that the interparticle potential is given by Eq. (D.44). (See Table D.4 for other parameters.) The screening potential, $H^e(r)$, defined in conjunction with the joint probability, $g(r)$, as

$$H^e(r) = V^e(r) + k_B T \ln[g(r)] , \tag{D.46}$$

has been sampled over 5×10^6 MC configurations generated with 500 particles in the periodic boundary conditions; the result is plotted in Fig. D.6.

We have then derived the following analytic formula to fit the MC data:

$$\frac{H^e(r)}{(Ze)^2/a} = \begin{cases} 0.8252 - 0.2312 \left(\frac{r}{a}\right)^2 , & \frac{r}{a} < 0.8427 , \quad \text{(D.47a)} \\ -1.048 + 2.071 \exp\left(-0.228 \frac{r}{a}\right) , & 0.8427 \le \frac{r}{a} < 2 . \quad \text{(D.47b)} \end{cases}$$

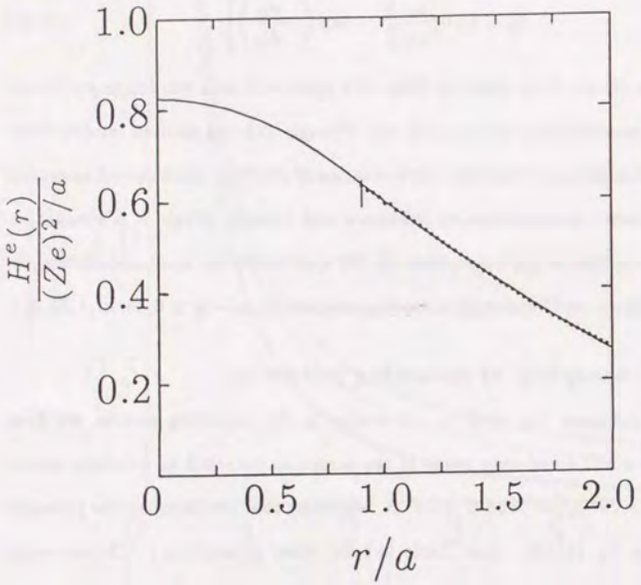

Fig. D.6 Screening potential in a carbon matter with the screened potential (D.44) and $D_S/a = 3.2$. The maximum extent of uncertainties in the MC sampling points is 10^{-5}, unless explicitly shown by vertical bars.

The intermediate-range expression, Eq. (D.47b), stems from an actual fit of the MC data as shown in Fig. D.6. Equation (D.47a) derives from the short-range expansion:

$$H^e(r) = H^e(0) - \frac{(Ze)^2}{12a}\left(\frac{a}{D_S}\right)^2 \left\langle \sum_{l\neq 1} \frac{a_{1l}}{r_{1l}} \exp\left(-\frac{r_{1l}}{D_S}\right)\right\rangle \left(\frac{r}{a}\right)^2 . \qquad \text{(D.48)}$$

The statistical average in the second term can be evaluated by the MC sampling in a test-particle system in which the test-particle "1" interacts with other 498 "l" particles via a potential $2V^e(r)$, while the 498 "l" particles interact with each other by the potential $V^e(r)$. The coefficient, 0.2312, in the second term of Eq. (D.47a) has been obtained through evaluation of the statistical average over 3×10^6 MC configurations generated in such a system. With this coefficient determined, the first term, 0.8252, stems from a smooth extrapolation of (D.47b) towards the short-range domain.

In the absence of electron screening, the carbon OCP under consideration has $H(0)/[(Ze)^2/a] = 1.110$ from Eq. (D.6). Hence, the MC simulation data yield

$$\beta_0 = (1.110 - 0.8252)/6^{1/3} = 0.1567 ,$$

a value in agreement with (D.45) listed in Table D.4.

(c) Enhancement of thermonuclear reactions due to electron screening

In this section, we are concerned with the assessment of the extent to which electron screening affects the contact probabilities and the reaction rates.

We approach this problem by observing that the electron screening effect, though finite and thus non-negligible, may be treated as a weak perturbation, and

that the WKB approximation (e.g., Salpeter and Van Horn, 1969) is applicable in the evaluation of the enhancement factor due to the electron screening. The contact probabilities $|\Psi_{ij}(0)|^2$ are proportional to the WKB penetration probabilities $P_{ij}(E)$ between reacting nuclei:

$$P_{ij}(E) = \exp\left[-\frac{2\sqrt{2\mu_{ij}}}{\hbar}\int_0^{r^c} dr\sqrt{W_{ij}(r)-E}\right] . \tag{D.49}$$

Here r^c is the classical turning radius satisfying

$$W_{ij}(r^c) = E , \tag{D.50}$$

$W_{ij}(r)$ is the effective potential of scattering between the reacting nuclei,

$$W_{ij}(r) = V_{ij}^e(r) - H_{ij}^e(r) , \tag{D.51}$$

and in light of (D.47) we set the electron-screened BIM screening potentials in the semiclassical approximation ($\Lambda_i < 1$) as

$$\frac{H_{ij}^e(r)}{Z_iZ_je^2/a_{ij}} = \begin{cases} 0.8252 - 0.2312\left(\frac{r}{a_{ij}}\right)^2 , \ \frac{r}{a_{ij}} < 0.8427 , & \text{(D.52a)} \\ -1.048 + 2.071\exp\left(-0.228\frac{r}{a_{ij}}\right) , \ 0.8427 \le \frac{r}{a_{ij}} < 2 . & \text{(D.52b)} \end{cases}$$

The penetration probabilities $P_{ij}^e(T)$ at temperatures T with inclusion of the electron screening are then evaluated through thermal averages of (D.49) over the Boltzmann factor, that is,

$$P_{ij}^e(T) = \frac{2}{\sqrt{\pi}(k_BT)^{3/2}}\int_0^\infty dE\sqrt{E}\exp\left(-\frac{E}{k_BT}\right)P_{ij}(E) . \tag{D.53}$$

The integration (D.53) usually involves a passage across the Gamow peak.

Let $P_{ij}^{e0}(T)$ be defined as $P_{ij}^e(T)$ evaluated in the absence of $H_{ij}^e(r)$, that is, when $W_{ij}(r)$ is given by $V_{ij}^e(r)$ alone. We may likewise define $P_{ij}(T)$ and $P_{ij}^0(T)$,

respectively, as the BIM penetration probabilities with the bare Coulomb repulsion (i.e., without electron screening) with and without the screening potentials $H_{ij}(r)$.

Since the classical turning radii at the Gamow peak, $r_{ij}^c \simeq 3\Gamma_{ij}a_{ij}/\tau_{ij}$, are smaller substantially than the short-range screening distance D_S (cf. Table D.4), where

$$\tau_{ij} = \left(\frac{27\pi^2}{4}\frac{Z_iZ_je^2}{r_{ij}^*k_BT}\right)^{1/3} , \tag{D.54}$$

we obtain

$$\frac{P_{ij}^{e0}(T)}{P_{ij}^0(T)} = \exp[\alpha_0\langle Z\rangle^{1/3}\Gamma_{ij} - D_{ij}^{\rm QM}] , \tag{D.55}$$

$$D_{ij}^{\rm QM} = \frac{3}{8}\Gamma_{ij}(\alpha_0\langle Z\rangle^{1/3})^2\left(\frac{3\Gamma_{ij}}{\tau_{ij}}\right) - 0.091\Gamma_{ij}(\alpha_0\langle Z\rangle^{1/3})^{2.923}\left(\frac{3\Gamma_{ij}}{\tau_{ij}}\right)^{1.897} . \tag{D.56}$$

For the derivation of the parametrized formula (D.56), we have carried out relevant WKB integrations (D.49) for 12 cases of the combination: $\alpha_0\langle Z\rangle^{1/3} = 0.2$, 0.4, and 0.6; and $3\Gamma_{ij}/\tau_{ij} = 0.5$, 1.0, 1.5, and 2.0. The first term of (D.56) can also be obtained analytically through expansion of (D.49) with respect to $\alpha_0\langle Z\rangle^{1/3}(3\Gamma_{ij}/\tau_{ij})$. The reaction rate resulting from the direct process between i and j is enhanced by the factor (D.55) due to the screening action of the relativistic electrons.

The enhancement factors of the thermonuclear reaction rates stemming from the screening potentials are defined as

$$\exp(Q_{ij}^e) = \frac{P_{ij}^e(T)}{P_{ij}^{e0}(T)} , \tag{D.57}$$

and

$$\exp(Q_{ij}) = \frac{P_{ij}(T)}{P_{ij}^0(T)} . \tag{D.58}$$

The latter quantity has been extensively investigated for the C-O BIM fluids (see Sec. D.IV). In the present WKB calculations where the screening potentials are regarded as weak perturbations, we find

$$Q_{ij}^{e} = 0.8252\Gamma_{ij} - Q_{ij}^{e\mathrm{QM}} \tag{D.59}$$

with

$$Q_{ij}^{e\mathrm{QM}} = 0.354 \exp\left[-0.228\left(\frac{3\Gamma_{ij}}{\tau_{ij}}\right)\right]\Gamma_{ij}\left(\frac{3\Gamma_{ij}}{\tau_{ij}}\right) , \tag{D.60}$$

and

$$Q_{ij} = 1.057\Gamma_{ij} - Q_{ij}^{\mathrm{QM}} \tag{D.61}$$

with

$$Q_{ij}^{\mathrm{QM}} = 0.342\Gamma_{ij}\frac{3\Gamma_{ij}}{\tau_{ij}} . \tag{D.62}$$

The first terms on the right-hand sides of (D.59) and (D.61) correspond to the classical contributions. The second terms represent the quantum corrections, resulting from the spatial variations of the screening potentials.

Finally, summing up Eqs. (D.55), (D.56), (D.59), and (D.61), we obtain the total enhancement factor of the nuclear reaction rate due to the electron screening as

$$A_e = \exp\left[(\alpha_0 - \beta_0)\langle Z\rangle^{1/3}\Gamma_{ij} - D_{ij}^{\mathrm{QM}} - Q_{ij}^{e\mathrm{QM}} + Q_{ij}^{\mathrm{QM}}\right] . \tag{D.63}$$

For the OCP, we may write this as

$$A_e = A_e^{\mathrm{IU}} \exp\left(-D^{\mathrm{QM}} - Q^{e\mathrm{QM}} + Q^{\mathrm{QM}}\right) \tag{D.64}$$

in light of (D.43), where β_0 is to be evaluated in accord with (D.45). The main difference between the present evaluation of the enhancement factor and that of

Ichimaru-Utsumi (1984) stems from the balance between the quantum corrections with and without the electron screening. Since the quantum corrections are nonlinear in plasma coupling parameters, the differences widen when the latter parameters are large. As Table D.4 illustrates, the enhancement of nuclear reaction due to the electron screening is significant in high-Z materials such as carbon and oxygen at high densities near ignition.

VI. Carbon ignition curves

As an example of applications for the theory of nuclear reaction rates in dense C-O BIMs described in Sec. D.II and D.III, and the extra enhancement due to the electron screening evaluated in Sec. D.IV, we calculate in this section the carbon ignition curves, that is, the loci of points in the density-temperature plane for which the $^{12}\mathrm{C} + {}^{12}\mathrm{C}$ energy release equals the neutrino energy loss. Following the conventional treatments (Arnett and Truran, 1969; Nomoto, 1982), we assume an approximate rate of such an energy release to be 3×10^{17} erg g^{-1}. For the neutrino loss rate, we use the results reviewed by Itoh *et al.* (1989), both in fluids and in solids.

In Figs. D.7 and D.8, the carbon ignition curves in C-O BIMs (i.e., without screening) are depicted. For the reaction rates in fluids, we have considered, not only the cases with the enhancement factors (D.33) (the solid curves), but also those with Eq. (D.20) (the dashed curves) and with Eq. (D.36) (the dot-dashed curves). In Fig. D.8, where a BIM with $x = 0.9$ is treated, we have taken the solidification line at $T = 1.43T_{\mathrm{C}}$ (see Fig. C.3), where T_{C} is the freezing temperature of a pure carbon material. In Fig. D.9, the carbon ignition curves obtained with (the solid curves) and without (the dotted curves) the electron

screening are compared for a pure carbon material and a C-O material with $x = 0.9$ in the fluid phase.

We stress that those curves have been obtained under the specific assumptions about the loss processes; if other processes unaccounted for in the present calculations are more effective, the curves would naturally have to be shifted.

We note in Figs. D.7 and D.8 a small but finite discrepancy in the ignition lines between the thermonuclear (i.e., fluid) and pycnonuclear (i.e., crystalline) regimes across the freezing transitions. The microscopic features of the correlations and hence the magnitude of the contact probabilities exhibit drastic changes across such a phase boundary; one generally anticipates such a gap to take place. We emphasize, however, that in each regime the reaction rate has been evaluated in a way physically consistent with the microscopic states of the reacting particles in the fluid or crystalline substance.

VII. Concluding remarks

We have presented first-principles calculations of nuclear reaction rates in dense C-O BIMs appropriate to Type-I supernova progenitors for fluid (thermonuclear) and *bcc* crystalline (pycnonuclear) phases. The calculations are based on an elaborate Monte Carlo simulation study of the screening potentials and a correct treatment of the quantum-statistical effects through an accurate solution to the S-wave Schrödinger equations. In the limiting cases of the OCP, the numerical results do not differ significantly from the pycnonuclear reaction rates of Salpeter and Van Horn (1969) and the thermonuclear reaction rates of Alastuey and Jancovici (1978), but the accurate evaluations of the reaction rates in C-O BIMs are

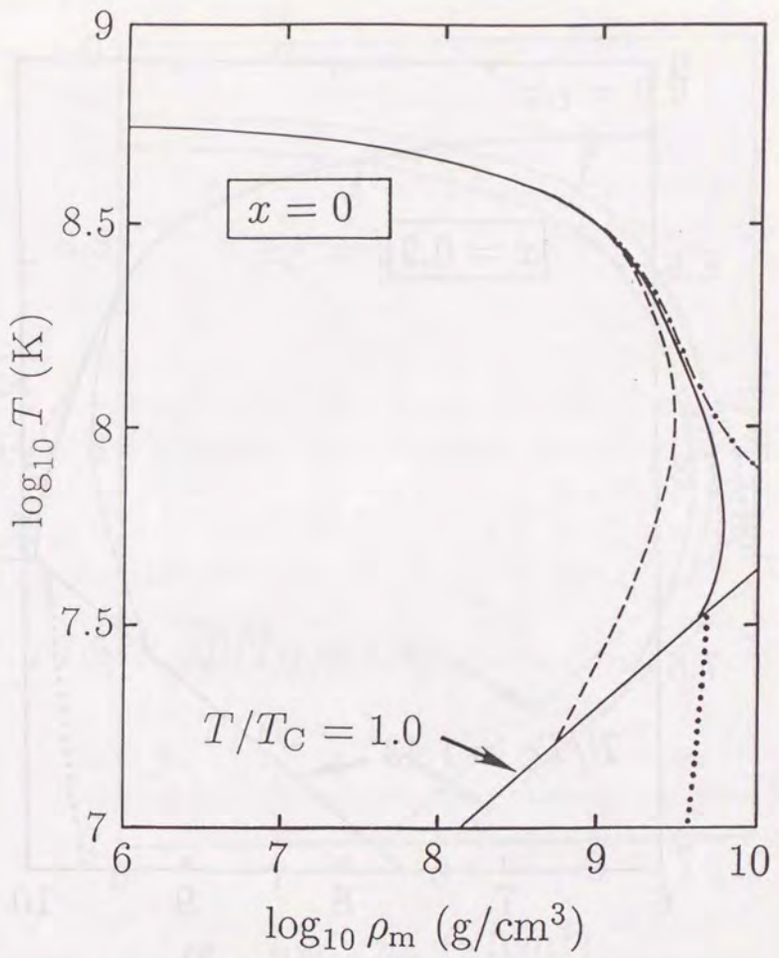

Fig. D.7 Carbon ignition curves in pure carbon material ($x = 0$). The solid curve is derived from the enhancement factor with Eq. (D.33); the dashed curve, Eq. (D.20); the dot-dashed curve, Eq. (D.36). The dotted curve is for the solid state.

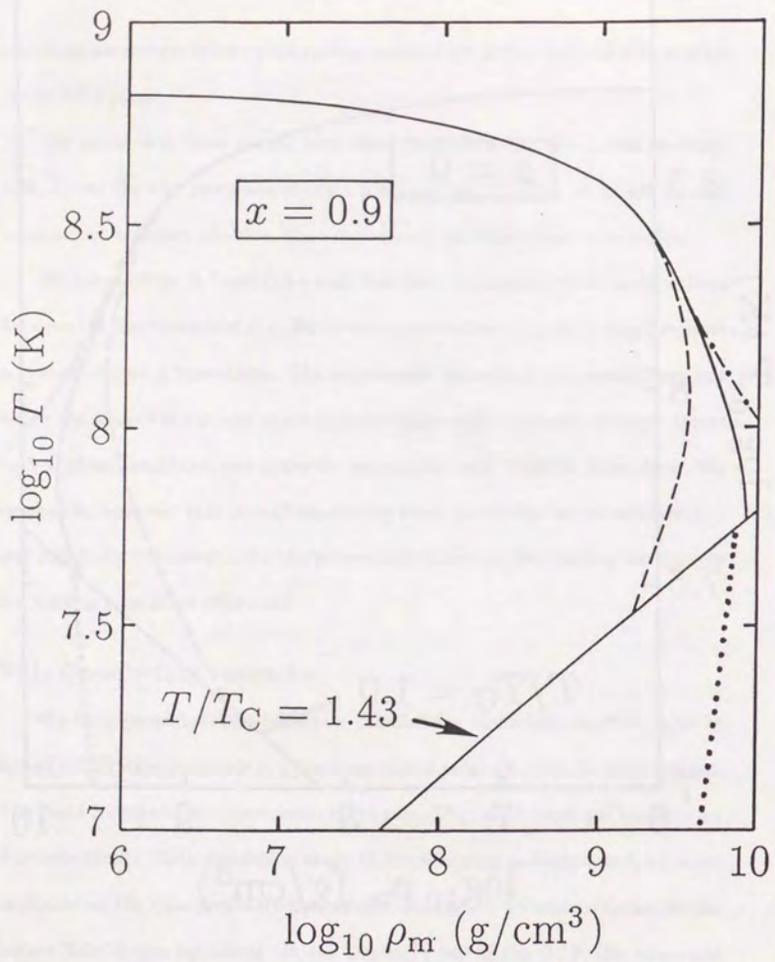

Fig. D.8 Carbon ignition curves in C-O BIM with $x = 0.9$. The solid curve is derived from the enhancement factor with Eq. (D.33); the dashed curve, Eq. (D.20); the dot-dashed curve, Eq. (D.36). The dotted curve is for the solid state.

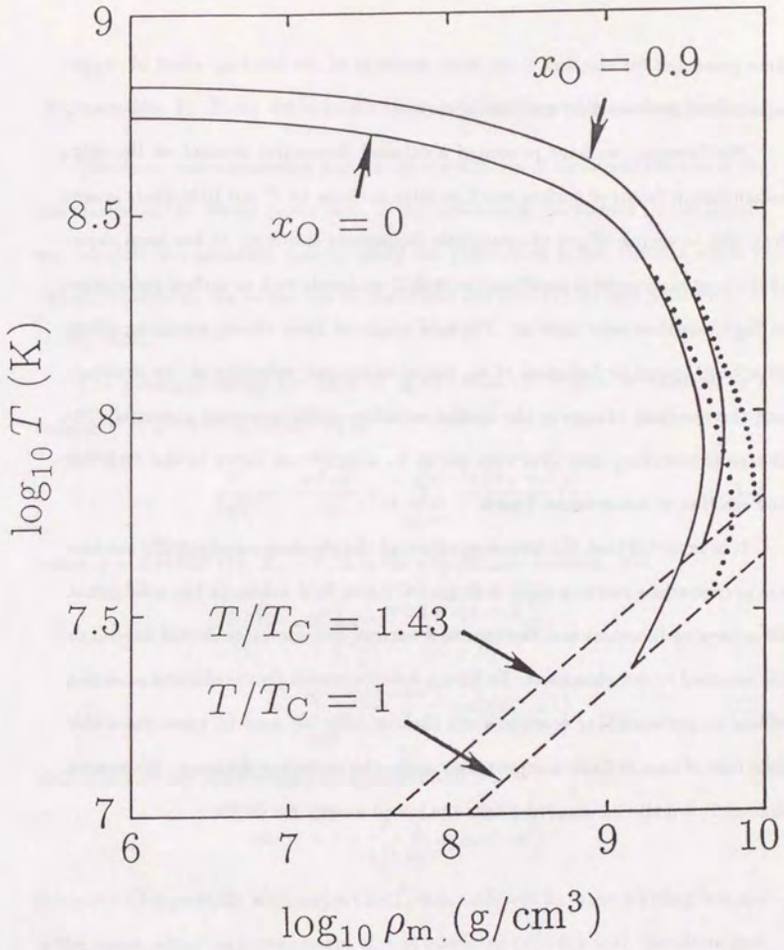

Fig. D.9 Carbon ignition curves in C-O BIM fluids with (solid curves) and without (dotted curves) electron screening. x_O is the molar fraction of oxygen.

here presented for the first time, with inclusion of the blocking effect of oxygen against the pycnonuclear reaction of carbon.

Furthermore, we have presented a detailed theoretical account on the extra enhancement factor of nuclear reaction rates in dense OCP and BIM fluids arising from the screening effects of relativistic degenerate electrons. It has been shown that the enhancement is significant in high-Z materials such as carbon and oxygen at high densities near ignition. Physical origin of these strong screening effects have been traced to finiteness of α_0 due to relativistic softening of the electrons, and the resultant change in the spatial variation of the screening potential. The electronic screening may thus turn out to be a significant factor in the evolution and ignition of dense white dwarfs.

It is expected that the screening effects of the electrons substantially enhance the pycnonuclear reaction rates in dense OCP and BIM solids. In the solid phase, the screening functions and the resultant nuclear reaction rates should depend on the assumed lattice structures. To have a definite answer for the electron screening effects on pycnonuclear reaction rates theoretically, we need to know the stable structure of ions at finite temperatures under the screening electrons. We remark that at $T = 0$ the *bcc* structure take the lowest energy for OCPs.

Appendix I: Fast computation of the Ewald potential

The most time-consuming part in the simulations of Coulomb systems is the calculation of the Ewald potentials. In the simulations performed in the Thesis, we calculate the potential rapidly using the polynomial fitted formula which is obtained following the recipe due to Slater and DeCicco (1963) and Slattery *et al.* (1980, 1982).

The potential energy (in units of $k_{\rm B}T$) of the OCP with N particles in a volume $V = L^3$, $L = (4\pi N/3)^{1/3}a$ is

$$\frac{U}{k_{\rm B}T} = -\frac{aN\alpha\Gamma}{2L} + \frac{1}{2}\sum_{i\neq j=1}^{N}\frac{U_1(\vec{X}_i - \vec{X}_j)}{k_{\rm B}T}\,, \tag{I.1}$$

where $\alpha = 2.837297479$, $\vec{X}_i = \vec{r}_i/L$ is the i-th particle position, and

$$\frac{U_1(\vec{X})}{k_{\rm B}T} = \frac{a\Gamma}{L}\left\{\sum_{\vec{n}}\frac{\mathrm{erfc}\left(\sqrt{\pi}|\vec{n}-\vec{X}|\right)}{|\vec{n}-\vec{X}|} - 1 \right. \\ \left. \sum_{\vec{n}\neq\vec{0}}\frac{\exp(-\pi n^2)}{\pi n^2}\cos[2\pi\vec{n}\cdot\vec{X}]\right\}. \tag{I.2}$$

Here $\vec{n}$ is a vector with integer components and

$$\mathrm{erfc}(t) = 1 - \frac{2}{\sqrt{\pi}}\int_0^t ds\exp(-s^2)\,.$$

Since $U_1(\vec{X})$ is periodic with respect to $\vec{X}$, it is sufficient to make a fitting formula in the region where each component of $\vec{X}$ is restricted to $[-0.5, 0.5]$. Recalling that $U_1(\vec{X})$ has the cubic symmetry, we introduce the fitting formula in the following form:

$$\frac{U_1^{\rm f}(\vec{X})}{k_{\rm B}T} = \frac{a\Gamma}{L}\left\{\frac{1}{X} - \alpha + \frac{2\pi}{3}X^2\right.$$

$$
\begin{aligned}
&+ a_4[P_4(\hat{x}) + P_4(\hat{y}) + P_4(\hat{z})]X^4 \\
&+ a_6[P_6(\hat{x}) + P_6(\hat{y}) + P_6(\hat{z})]X^6 \\
&\quad\vdots \\
&+ a_{22}[P_{22}(\hat{x}) + P_{22}(\hat{y}) + P_{22}(\hat{z})]X^{22} \\
&+ b_{12}\mathrm{Re}[(\hat{x}+i\hat{y})^{12} + (\hat{y}+i\hat{z})^{12} + (\hat{z}+i\hat{x})^{12}]X^{12}\Big\}\,, \qquad \text{(I.3)}
\end{aligned}
$$

where $(\hat{x}, \hat{y}, \hat{z}) = \vec{X}/|X|$ and $P_l(\hat{x})$ is l-th order Legendre polynomial. The first three terms in Eq. (I.3) result from the expansion of $U_1(\vec{X})$. Parameters $a_4, a_6, \cdots, a_{22}$, and b_{12} are optimized via the least square method using 8000 random points of $\vec{X}$.

To know the extent of relative errors of the fitting formula, we compare the potential energy which is calculated using Eq. (I.3) with the exact value for 5000 cases of random configurations and for the *bcc* and *fcc* configurations with $N = 1024$. Relative errors are 3 parts in 10^8 for the random configurations; 1 part in 10^7 for the *bcc* and *fcc* configurations. The fitting formula (I.3) has a sufficient accuracy for MC simulations. We remark in addition that the fitting formula Eq. (I.3) also applies directly to the multi-component systems with appropriate substitutions of Γ and L.

Appendix II: MC sampling of the coefficient h_2 in equation (D.3)

Let $\Phi(r)$ be the Coulomb potential (in units of $k_B T$) acting on a given test particle with charge $2Ze$ at r from all other N particles forming the OCP with charge Ze. The coefficient h_2 in Eq. (D.3) is then calculated in the ensemble of MC generated configurations as

$$
h_2 = \frac{a^4}{384}\left\langle\left[\left(\frac{d\Phi}{dx}\right)^2 - 2\frac{d^2\Phi}{dx^2}\right]^2\right\rangle - \frac{\Gamma^2}{32}\,, \qquad \text{(II.1)}
$$

where x represents one of the Cartesian components of r. The statistical average $\langle\ \rangle$ is carried out over 2.5×10^5 configurations in the MC sequences. To examine the accuracy of the MC averaging procedure, we have also computed

$$
h_1 = \frac{1}{8}\left\langle\left(\frac{d\Phi}{dx}\right)^2\right\rangle\,. \qquad \text{(II.2)}
$$

This quantity should exactly take on $\frac{\Gamma}{4}$ for OCP from Eq. (D.4).

The computed values are listed in Table II.1. With the accuracy confirmed in the MC evaluations of u, we may conclude that h_2 virtually vanishes; the computed values, smaller in magnitude than the extent of errors, are far smaller than h_1 in Eq. (D.4).

TABLE II.1. MC values of h_2 in Eq. (II.1). Also listed are h_1/Γ values in Eq. (II.2) which should take on $\frac{1}{4}$ from Eq. (D.4).

Γ	h_2	h_1/Γ
10	0.006 ± 0.088	0.2473 ± 0.0003
40	-1.2 ± 1.4	0.2480 ± 0.0001
80	-5.3 ± 5.4	0.2478 ± 0.0002
160	10.1 ± 21.3	0.2519 ± 0.0002

References

Abrikosov, A. A., 1960, Zh. Eksp. Teor. Fiz. **39**, 1798 [Sov. Phys. JETP. **12**, 1254].

Alastuey, A., and B. Jancovici, 1978, Astrophys. J. **226**, 1034.

Alder, B. J., and T. E. Wainwright, 1957, J. Chem. Phys. **27**, 1208.

Alder, B. J., and T. E. Wainwright, 1959, J. Chem. Phys. **31**, 459.

Andersen, H. C., and D. Chandler, 1972, J. Chem. Phys. **57**, 1918.

Arnett, W. D., and J. W. Truran, 1969, Astrophys. J. **157**, 339.

Ashcroft, N. W., and D. Stroud, 1978, Solid State Phys. **33**, 1.

Barkat, Z., C. Wheeler, and J.-R. Buchler, 1972, Astrophys. J. **171**, 651.

Barrett, J. L., J.-P. Hansen, and R. Mochkovich, 1988, Astron. Astrophys. **199**, L15.

Baus, M., and J.-P. Hansen, 1980, Phys. Rep. **59**, 1.

Baym, G., C. J. Pethick, and P. G. Sutherland, 1971, Astrophys. J. **170**, 299.

Binder, K., 1979, in *Monte Carlo methods in statistical physics*, edited by K. Binder (Springer-Verlag, Berlin), p. 1.

Brush, S. G., H. L. Sahlin, and E. Teller, 1966, J. Chem. Phys. **45**, 2102.

Canal, R., J. Isern, and J. Labay, 1982, Nature **296**, 225.

Canal, R., and E. Schatzman, 1976, Astron. Astrophys. **46**, 229.

Ciccotti, G., D. Frenkel, and I. R. McDonald, 1987, *Simulation of Liquids and Solids* (North-Holland, Amsterdam).

Couch, R. G., and W. D. Arnett, 1975, Astrophys. J. **196**, 791.

DeWitt, H. E., H. C. Graboske, and M. S. Cooper, 1973, Astrophys. J. **181**, 439.

Dubin, D. H. E., and T. M. O'Neil, Phys. Rev. Lett. **60**, 511 (1988).

Flowers, E., and N. Itoh, 1976, Astrophys. J. **206**, 218.

Fowler, W. A., G. R. Caughlan, and B. A. Zimmerman, 1975, Ann. Rev. Astron. Astrophys. **13**, 69.

Galam, S., and J.-P. Hansen, 1976, Phys. Rev. A **14**, 816.

Gilbert, S. L., J. J. Bollinger, and D. J. Wineland, Phys. Rev. Lett. **60**, 2022 (1988).

Graboske, H. C., 1973, Astrophys. J. **183**, 177.

Gudmundsson, E. H., C. J. Pethick, and R. I. Epstein, 1982, Astrophys. J. Lett. **259**, L19.

Hansen, J.-P., 1973, Phys. Rev. A **8**, 3096.

Hansen, J.-P., and I. R. McDonald, 1986, *Theory of Simple Liquids*, 2nd. ed. (Academic Press, London).

Hansen, J.-P., G. M. Torrie, and P. Vieillefosse, 1977, Phys. Rev. A **16**, 2153.

Helfer, H. L., R. L. McCrory, and H. M. Van Horn, 1981, J. Stat. Phys. **48**, 397.

Hoover, W. G., J. C. Poirer, 1962, J. Chem. Phys. **37**, 1041.

Ichimaru, S., 1982, Rev. Mod. Phys. **54**, 1017.

Ichimaru, S., H. Iyetomi, S. Mitake, and N. Itoh, 1983, Astrophys. J. Lett. **265**, L83.

Ichimaru, S., H. Iyetomi, and S. Ogata, 1988, Astrophys. J. Lett. **334**, L17.

Ichimaru, S., H. Iyetomi, and S. Tanaka, 1987, Phys. Rep. **149**, 91.

Ichimaru, S., A. Nakano, S. Ogata, S. Tanaka, H. Iyetomi, and T. Tajima, 1990, J. Phys. Soc. Jpn. **59**, 1333.

Ichimaru, S., and S. Ogata, 1990, in *Strongly Coupled Plasma Physics*, edited by S. Ichimaru (North-Holland, Amsterdam), p. 101.

Ichimaru, S., and S. Ogata, 1991, Astrophys. J. (in press, June 20 issue).

Ichimaru, S., and S. Tanaka, 1986, Phys. Rev. Lett. **56**, 2815.

Ichimaru, S., and K. Utsumi, 1981, Phys. Rev. B **24**, 7365.

Ichimaru, S., and K. Utsumi, 1983, Astrophys. J. Lett. **269**, L51.

Ichimaru, S., and K. Utsumi, 1984, Astrophys. J. **286**, 363.

Itoh, N., T. Adachi, M. Nakagawa, Y. Kohyama, and H. Munakata, 1989, Astrophys. J. **339**, 354.

Itoh, N., S. Mitake, H. Iyetomi, and S. Ichimaru, 1983, Astrophys. J. **273**, 744.

Itoh, N., H. Totsuji, and S. Ichimaru, 1978, Astrophys. J. **218**, 477.

Itoh, N., H. Totsuji, S. Ichimaru, and H. E. DeWitt, 1979, Astrophys. J. **234**, 1079.

Iyetomi, H., S. Ichimaru, 1982, Phys. Rev. A **25**, 2434.

Iyetomi, H., S. Ichimaru, 1983a, Phys. Rev. A **27**, 1734.

Iyetomi, H., S. Ichimaru, 1983b, Phys. Rev. A **27**, 3241.

Iyetomi, H., S. Ichimaru, 1986, Phys. Rev. A **34**, 3203.

Iyetomi, H., S. Ichimaru, 1988, Phys. Rev. B **38**, 6761.

Iyetomi, H., S. Ogata, and S. Ichimaru, 1989, Phys. Rev. B **40**, 309.

Jancovici, B., 1962, Nuovo Cimento **25**, 428.

Jancovici, B., 1977, J. Stat. Phys. **17**, 357.

Kirzhnitz, D. A., 1960, Zh. Eksp. Teor. Fiz. **38**, 503 [Sov. Phys. JETP. **11**, 365].

Landau, L. D., and E. M. Lifshitz, 1969, *Statistical Physics* (Pergamon Press, Oxford), Sec. 58.

Landau, L. D., and E. M. Lifshitz, 1970, *Theory of Elasticity*, 2nd ed. (Pergamon Press, Oxford), Chap. I.

Landau, L. D., and E. M. Lifshitz, 1976, *Quantum Mechanics*, 3rd. ed. (Pergamon press, Oxford), p. 433.

Lindhard, J., 1954, K. Dan. Vidensk. Selsk. Matt.-Fys. Medd. **28**, No. 8.

McDermott, P. N., C. J. Hansen, H. M. Van Horn, and R. Buland, 1985, Astrophys. J. Lett. **297**, L37.

McDermott, P. N., H. M. Van Horn, and C. J. Hansen, 1988, Astrophys. J. **325**, 725.

Metropolis, N., A. W. Rosenbluth, M. N. Rosenbluth, A. H. Teller, and E. Teller, 1953, J. Chem. Phys. **21**, 1087.

Mochkovitch, R., 1983, Astron. Astrophys. **122**, 212.

Mott N. F., and H. Jones, 1936, *The Theory of the Properties of Metals and Alloys* (Clarendon Press, Oxford) Chap. IV, Sec. 4.

Nielsen, O. H., and R. M. Martin, 1983, Phys. Rev. Lett., **50**, 697.

Nomoto, K., 1982, Astrophys. J., **253**, 798.

Ogata. S., 1991, Phys. Rev. A (submitted).

Ogata, S., and S. Ichimaru, 1987, Phys. Rev. A **36**, 5451.

Ogata, S., and S. Ichimaru, 1988, Phys. Rev. A **38**, 1457.

Ogata, S., and S. Ichimaru, 1989a, Phys. Rev. A **39**, 1333 [referred to as Paper I].

Ogata, S., and S. Ichimaru, 1989b, Phys. Rev. Lett. **62**, 2293.

Ogata, S., and S. Ichimaru, 1989c, J. Phys. Soc. Jpn. **58**, 356.

Ogata, S., and S. Ichimaru, 1989d, J. Phys. Soc. Jpn. **58**, 3049.

Ogata, S., and S. Ichimaru, 1990a, Astrophys. J. **361**, 511.

Ogata, S., and S. Ichimaru, 1990b, Phy. Rev. A **42**, 4867.

Ogata, S., H. Iyetomi, and S. Ichimaru, 1990, in *Strongly Coupled Plasma Physics*,, edited by S. Ichimaru (North-Holland, Ameterdam), p. 59.

Ogata, S., H. Iyetomi, and S. Ichimaru, 1991, Astrophys. J. (in press, May 1 issue).

Pandharipande, V. R., D. Pines, and R. A. Smith, 1976, Astrophys. J. **208**, 550.

Pines, D., 1964, *Elementary Excitations in Solids* (Benjamin, New York).

Rahman, A., and J. P. Schiffer, 1986, Phys. Rev. Lett. **57**, 1133.

Ruderman, M. A., 1968, Nature **218**, 1126.

Salpeter, E. E., 1954, Aust. J. Phys. **7**, 373.

Salpeter, E. E., 1961, Astrophys. J. **134**, 669.

Salpeter, E. E., and H. M. Van Horn, 1969, Astrophys. J. **155**, 183.

Sato, K., and S. Ichimaru, 1989, J. Phys. Soc. Jpn. **58**, 787.

Schiferl, S. K., and D. C. Wallace, 1985, Phys. Rev. B **31**, 7662.

Schiffer, J. P., 1988, Phys. Rev. Lett. **61**, 1843.

Schumaker, B. L., and K. S. Thorne, 1983, M. N. R. A. S. **203**, 457.

Shapiro, S. L., and S. A. Teukolsky, 1983, *Black Holes, White Dwarfs, and Neutron Stars* (John Wiley & Sons, New York).

Slater, J. C., and P. DeCicco, 1963, MIT Solid State and Molecular Theory Group Quarterly Progress Report **50**, 46.

Slattery, W. L., G. D. Doolen, and H. E. DeWitt, 1980, Phys. Rev. A **21**, 2087.

Slattery, W. L., G. D. Doolen, and H. E. DeWitt, 1982, Phys. Rev. A **26**, 2255.

Squire, D. R., A. C. Holt, and W. G. Hoover, 1969, Physica **42**, 388.

Starrfield, S., J. W. Truran, W. N. Sparks, and G. S. Kutter, 1972, Astrophys. J. **176**, 169.

Steinhardt, P. J., D. R. Nelson, and M. Ronchetti, 1983, Phys. Rev. B **28**, 784.

Stevenson, D. J., 1980, J. Phys. (Paris) Suppl. **41**, C2-61.

Strohmayer, T. E., S. Ogata, H. Iyetomi, S. Ichimaru, and H. M. Van Horn, 1991, Astrophys. J. (in press, June 10 issue).

Unno, W., Y. Osaki, H. Ando, and H. Shibahashi, 1989, *Nonradial oscillation of stars* (Univ. of Tokyo Press, Tokyo).

Van Horn, H. M., 1990, in *Strongly Coupled Plasma Physics*, edited by S. Ichimaru (North-Holland, Amsterdam), p. 3.

Wallace, D. C., S. K. Schiferl, and G. K. Straub, 1984, Phys. Rev A **30**, 616.

Whelen, J., and I. Iben, 1973, Astrophys. J. **186**, 1007.

Widom, B. 1963, J. Chem. Phys. **39**, 2803.

Wigner, E. P., 1934, Phys. Rev. **46**, 1002.

281